GUIDED WAVE EVALUATION OF PIPES USING THE FIRST AND SECOND ORDER TORSIONAL WAVE MODES

Matthew Deere

Brunel University London

College of Engineering, Design and Physical Sciences

A thesis submitted in partial fulfilment for the degree of Doctor of Philosophy

February 2017

Dedicated to my

Mum and Dad

ABSTRACT

Guided wave inspection is a form of ultrasonic testing used for non-destructive testing (NDT). Guided waves are capable of propagating long distances bounded by the geometries of the specimen, such as pipes and plates. The technique is commercially used to detect defects in pipelines and is capable of a full volumetric screening many metres (often up to around 100m) from one location. Fundamental axisymmetric wave modes are used to inspect pipelines and are used to quantify defects and features. However, as the technology has progressed, a demand for improving defect sensitivity, spatial resolution and developing the technology into new fields has been recognised.

Operating at medium range frequencies is one possibility that could provide the increase in defect sensitivity and spatial resolution required that may not be achieved at low range frequencies. The use of higher order wave modes could also provide additional information useful for defect sizing.

Guided wave inspection is a complex ultrasonic technique due to the many wave modes that exist and testing at medium range frequencies requires some challenges to be overcome. The research presented here investigates the potential of using the second order torsional wave mode at medium range frequencies and provides a new sizing technique that for some applications is likely to offer advancement in guided wave inspection and monitoring.

The approach firstly included the design and implementation of a setup for analysing the complex signal responses in order to access the higher order torsional wave mode T(0,2) for defect sizing. An efficient method of using FEA has been presented using segmented models to provide the capability of analysing defects with small increment changes that could not be achieved using a full 3D model of the pipe. Using a pipe segment to virtually represent the full pipe also allowed small changes in defect size to be investigated, which would otherwise be extremely difficult to accurately machine experimentally. The FEA modelling technique is also based on broadband signals in comparison to the conventional approach of using narrowband signals and is capable of obtaining a wide frequency spectrum from one model, which significantly reduces the number of models needed to conduct a frequency analysis. Following on from this work, a high density transducer array was developed and compared against a conventional transducer array used in guided wave inspection for the purpose of medium range

frequency inspection, which can also be applied to conventional low range frequency inspection. Finally, a new defect sizing method using T(0,2) is presented, which is capable of predicting the depth using peak amplitude responses from spectral analysis and by comparing this to the cut-off frequency of the remaining wall thickness of the defect. The technique has the potential to improve defect sizing, defect sensitivity, increase spatial resolution, and increase the performance of medium range inspection.

ACKNOWLEDGEMENTS

I would like to thank my academic supervisor Prof. Luiz Wrobel firstly for presenting me with the opportunity to conduct the research for my Master's dissertation at TWI and secondly for his continued advice and support during my Ph.D study, for which I am most grateful.

I would like thank my industrial supervisor Peter Mudge for his advice and technical discussions during my study at TWI.

A special appreciation goes to Dr. Alex Haig for his technical support, knowledge and encouragement throughout my Ph.D study. I sincerely appreciate all the time and effort he has contributed.

I would like to thank my colleagues at TWI for being extremely pleasant people to work with. Our scientific discussions have been extremely beneficial and it has been a pleasure to work alongside you.

I would like to thank the Engineering and Physical Sciences Research Board (EPSRC), Brunel University London and TWI Ltd for providing the funding for this research.

Last, but by no means least my Mum and Dad for their love and support throughout my life. Without them this would not have been possible and for that I thank you.

CONTENTS

LIST OF TABLES

LIST OF FIGURES

LIST OF ABBREVIATIONS AND ACRONYMS

CSA **C**ross **S**ection **A**rea

EMAT Electro Magnetic Acoustic Transducer

FEA **F**inite **E**lement **A**nalysis

FT **F**ourier **T**ransform

GWT **G**uided **W**ave **T**esting

NDT **N**on **D**estructive **T**esting

UT **U**ltrasonic **T**esting

1 INTRODUCTION

This chapter provides an overview of the thesis and discusses the motivation for carrying out this research. This includes the current state of the art used for guided wave inspection and the potential areas for improvement. The main aims and objectives are described along with the thesis structure section to provide an overview of each chapter and the subsequent impact they have on each other. The final section describes the contributions to knowledge.

1.1 Motivation

This section provides an overview on the current methods used for guided wave inspection and highlights areas that could be investigated to improve the performance of the current state of the art.

1.1.1 Current Approach to Guided Wave Testing

Guided Wave Testing (GWT) is a branch of Non-Destructive Testing (NDT), commonly used to inspect pipelines. The ultrasonic technique is used to screen a length

of pipeline using ultrasonic wave modes (described in chapter 2) from one location in comparison to localised inspection using conventional Ultrasonic Testing (UT), as shown in Figure 1.1. The wave motion of a guided wave mode is bounded by the surfaces of the pipe wall and the main propagation direction is along the pipe rather than through the thickness of the pipe.

Pipelines can be thousands of metres in length and can exhibit corrosion, erosion, and external damage which are all ultimately defects. Therefore, the technique is highly suitable for inspecting long lengths of pipe for defects in comparison to conventional UT. Conventional UT tends to operate in the MHz frequency range using the longitudinal and shear bulk waves, whereas guided wave inspection is normally carried out at much low frequency range (typically less than 100kHz).

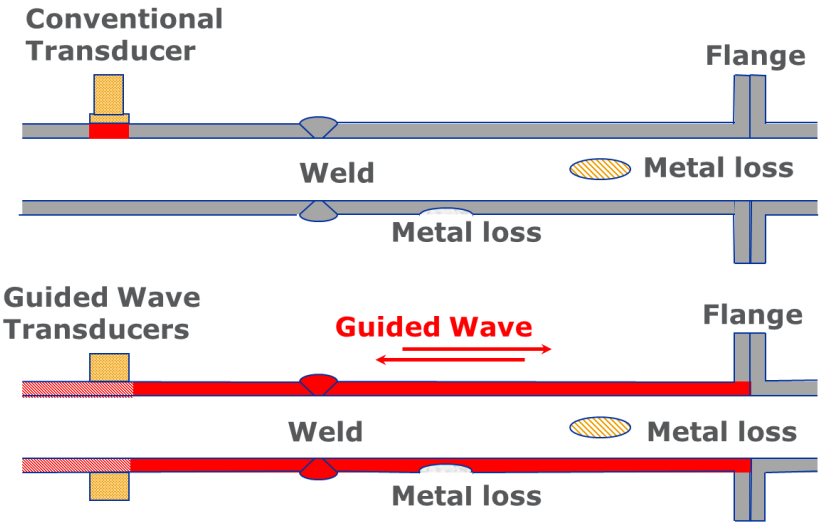

Figure 1.1. Conventional ultrasonic testing versus guided wave testing.

The technique uses arrays of circumferentially distributed transducers to transmit and receive guided waves. For conventional guided wave inspection the transducers in a particular array or "ring" are sequentially excited to provide a single transmitted wave mode. The number of rings used in transmission depends on the wave mode selected in transmission and these are used to provide unidirectional wave propagation and to

supress unwanted wave modes. Guided wave inspection receives signals that are reflected from a cross-sectional change in the pipe, which can be a defect or a feature, such as a weld, pipe support or pipe branch. The detection of the defects and features is generally presented on amplitude against distance graphs known as A-scans, used to quantify defects and to determine their location, based on the amplitude and velocity of the propagating wave. Figure 1.2 shows a typical guided wave system configuration.

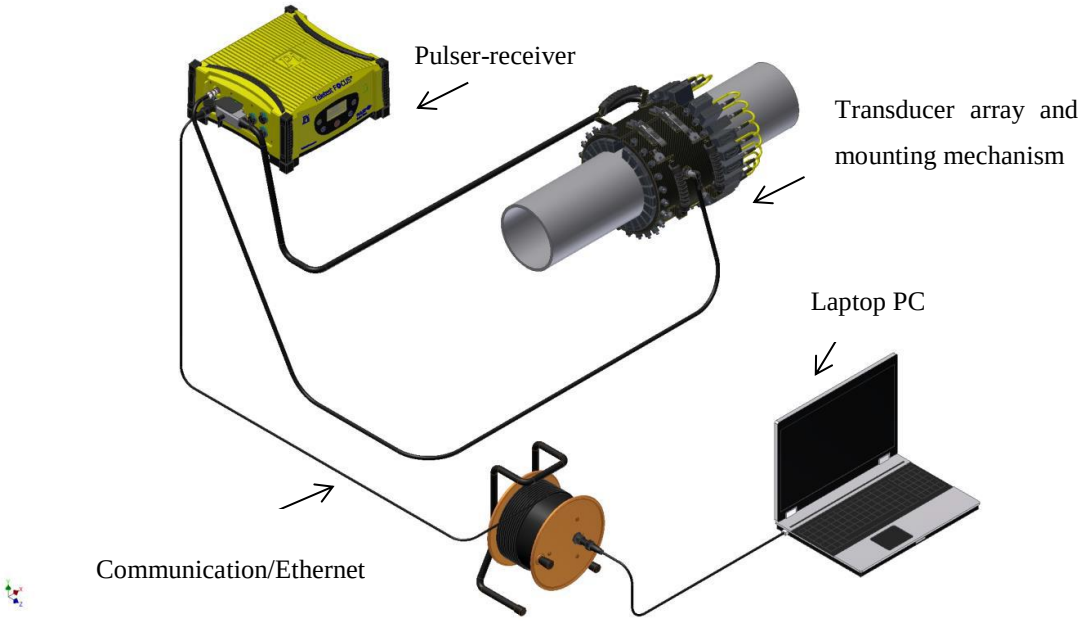

Figure 1.2. Teletest®Focus$^+$ guided wave system. The system consists of the pulser-receiver, piezoelectric transducer array and laptop PC with inspection software.

1.1.2 Potential Enhancements to Guided Wave Inspection

The majority of the guided wave systems including the Teletest Focus$^+$ developed by TWI, as shown in Figure 1.2 operate below 100kHz and propagate waves long distances in pipelines with single wave mode transmission. Due to the successful implementation of GWT on pipelines for long range inspection and demand for greater capability, the technique has provided ongoing research in the field. These areas include developing defect sizing techniques, improving signal to noise, improving defect sensitivity and applying the technology to other fields and applications. The technique is used for

detection of defects, but there is a demand from pipeline operators for better performance, hence the need for further developments.

A limitation of the current guided wave technique is the inability to inspect the near field of the pipe due to the inability to receive signals during the transmission period known as the ‘dead zone’. Another limitation is the defect sensitivity and the spatial resolution based on the frequency limit of the system.

To overcome the issue of the ‘dead zone’ using the current pulse-echo technique used in most commonly available guided wave systems would require operating above the typical range of less than 100kHz. Between 100 kHz and 1 MHz is generally referred to as medium range frequencies. However, the term medium range frequency is loosely used and is highly dependent on pipe dimensions. For the purpose of this thesis, medium range frequency is deemed to be the frequency range where higher order axisymmetric wave modes exist (wave modes are described in chapter 2). Increasing the frequency range also has the potential for increasing defect sensitivity and spatial resolution of defects. Medium range frequency signals have complex responses due to the multimode signal content; however, if a technique were to utilise medium range frequencies, an improvement in near field inspection, defect sensitivity and spatial resolution may be achieved.

1.2 Aims and Objectives

The aim of the research is to develop a technique for guided wave inspection using medium range frequencies (where higher order axisymmetric wave modes exist) in order to utilise higher order waves for defect sizing. To achieve a medium frequency inspection technique the following approach was taken:

- Investigate the literature for current guided wave technques and any potential gaps in the knowledge applicable to medium range frequency inspection.
- To develop a technique for locating and quantifying the size of defects using medium range frequencies by experimental and modelling procedures.
- To develop a technique for improving the efficiency of guided wave inspection through signal generation and interpretation for medium range frequencies.

1.3 Thesis Structure

The subsequent chapters begin by introducing guided waves and the ultrasonic wave types that are used for NDT are described. The purpose is to provide a comparison to other wave types showing the different characteristics of guided waves. The nomenclature for distinguishing different wave modes is presented and the concepts used throughout the thesis are described. Other concepts that are used throughout the thesis including dispersion and mode conversion are described in chapter 2.

Chapter 3 presents the literature review. This begins with the key developments in guided wave inspection from a historical prospective. Details are presented on the current guided wave systems available including the Teletest Focus+ system used for the experimental research conducted in this thesis. The succeeding sections are more focused towards guided wave inspection and relate to the areas that have been investigated, which include modelling, defect sizing and the use of medium and high range frequency guided waves.

Chapter 4 describes the key parameters and features needed to perform guided waves using medium range frequencies. A setup is described to provide the capability of separating wave modes and obtaining reflection coefficients for defect analysis. Other developments include a modified pipe model that increases the range of defects that can

be analysed, incorporated with an effective use of broadband signals providing a multiple frequency response from one data set.

Chapter 5 investigates the performance of the current transducer array design for both low and medium range frequencies. The areas investigated are the number of transducers in the array, the spacing between the transducers and the signal to noise performance. Using the results from this analysis, a high density array was developed for improving guided wave inspection.

Chapter 6 investigates a range of defects at medium range frequencies and a technique for defect sizing based on the reflection coefficient of T(0,2) was developed. The defect sizing technique was based on a relationship between defect depth, peak amplitude and frequency.

Finally, chapter 7 provides the overall conclusions from the thesis and provides recommendations for further work, based on the defect sizing technique developed.

1.4 Contributions to Knowledge

A novel technique has been developed for defect sizing using T(0,2) for medium range frequencies (chapter 6). The signal response from a particular defect size has a peak value at a particular transmission frequency and this frequency closely matches the cut-off frequency for the remaining wall thickness. Therefore, in a monitoring scenario, a spectral analysis can provide the frequency at which the peak amplitude occurs and this can be referenced to the T(0,2) dispersion curves for a range of remaining wall thicknesses to predict the defect size.

A modified pipe segment model was developed to increase the number of defects that can be feasibly analysed using FEA with the use of broadband signals (chapter 4). The modified pipe segment reduced the number of elements significantly for the same mesh size, providing the possibility of decreasing element size in order to analyse more defects without reaching the computational limits. Using broadband signals and a filtering technique for extracting narrowband signals from the results provided an efficient method to perform a spectral analysis on each defect size from one set of data. Using a narrowband transmission signal would have required an individual model for each frequency over all defect sizes, which is infeasible when using FEA. To the best of the author's knowledge the successful use of broadband signal for guided wave testing has not been implemented in FEA before.

Identified the advancement required of guided wave technology to achieve efficacy at medium range frequencies, which was done through the assessment of existing array design methods and the development of a high density array (chapter 5). The signal to noise of the high density array was increased in comparison to the existing transducer array at low frequencies. This was achieved by addressing the number of transducers and the transducer spacing with the objective of operating at both low and medium range frequencies. The conclusions from the results for medium range frequencies can provide recommendations on how to improve the design further, which are based on the transducer length. At medium range frequencies the transducer length has a significant impact on the transmission amplitude. In order to achieve the maximum signal output, the length of the transducer should be reduced as close to a point source as feasibly possible. A recommendation is to operate ideally to a maximum length of ¼ wavelength of the maximum frequency in the range. This shows that any medium range techniques, such as the new sizing technique discussed above, have potential for industrial application once transducer miniaturisation is achieved.

2 FUNDAMENTALS OF ULTRASONIC GUIDED WAVES

2.1 Introduction

This chapter provides an overview of guided waves focusing on the inspection of pipes. This includes a description of ultrasonic wave mode types and their characteristics. Other fundamentals of guided waves such as phase and group velocity, as well as dispersion are also included. All of these aspects provide crucial knowledge needed for guided wave testing and new technique developments.

2.2 Types of Ultrasonic Waves

There are typically two types of waves used in conventional ultrasonic testing, known as the longitudinal and shear bulk waves. These waves propagate in an infinite media and are therefore not bounded by geometry. There are also surface waves that are bounded by one surface of a thick structure considered to be semi-infinite media or as a half space, known as Rayleigh and Love waves. Finally, there are guided waves which

are bounded by two surfaces and propagate along the thickness of a medium which can be defined as a plate or cylindrical structure.

2.2.1 Longitudinal Waves

Longitudinal waves occur when the direction of wave propagation is in the same plane as the particle oscillations, as shown in Figure 2.1. Longitudinal waves are also known as compression or pressures waves.

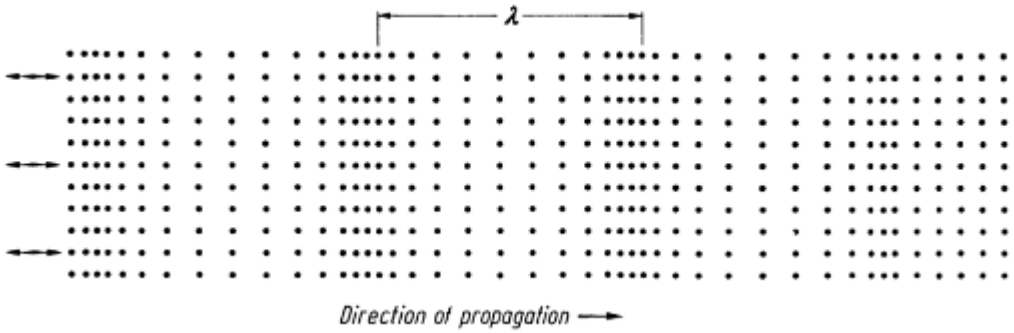

Figure 2.1. Longitudinal wave. The direction of propagation (left to right) is in line with the particle vibration (double headed arrows).

Longitudinal waves can propagate through solids, liquids and gases as long as there is a medium, which all show resistance to compressing or stretching caused by the elasticity of the material or medium. In solids this resistance is known as Young's Modulus (E). Eq. 2.1 defines the longitudinal wave velocity (C_l), where μ is the Poisson's ratio and ρ is the density (Krautkrämer et al. [2013]).

$$c_l = \sqrt{\frac{E}{\rho}\left(\frac{1-\mu}{(1+\mu)(1-2\mu)}\right)} \tag{2.1}$$

2.2.2 Shear Waves

Shear waves occur when the direction of wave propagation is perpendicular to the particle oscillations, as shown in Figure 2.2. Shear waves are also known as transverse waves.

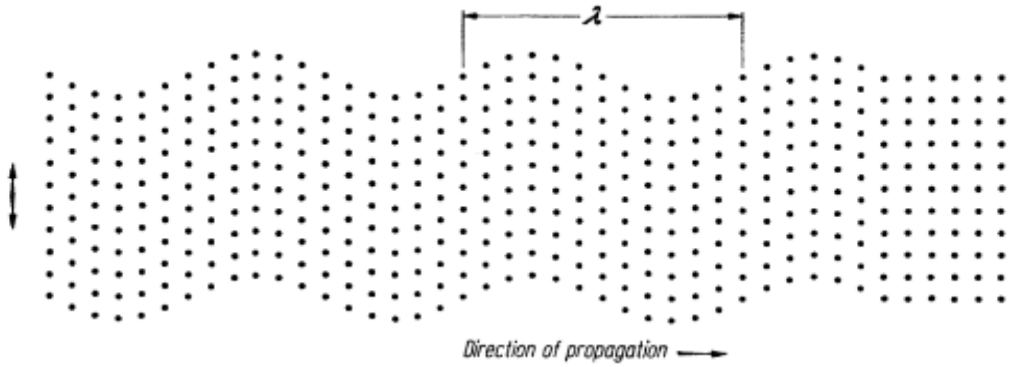

Figure 2.2. Shear wave. The direction of propagation (left to right) is perpendicular to the particle vibration (double headed arrow).

Shear waves can only propagate in solids or fluids with high viscosity. Low viscosity fluids such as water and air cannot support shear stresses. Eq. 2.2 defines the shear wave velocity (C_t).

$$c_t = \sqrt{\frac{E}{\rho}\left(\frac{1}{2(1+\mu)}\right)} \qquad \textbf{(2.2)}$$

2.2.3 Rayleigh Waves

Rayleigh waves are a type of surface wave first predicted in the 19th century and named after the discoverer John W Strutt also known as Lord Rayleigh (published under Rayleigh or Strutt [1885]). The particles oscillate in an elliptical motion providing wave propagation along this axis, as shown in Figure 2.3.

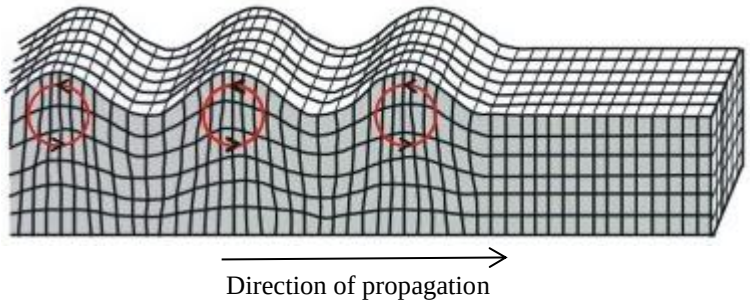

Figure 2.3. Rayleigh wave. Particles oscillate in an anti-clockwise elliptical motion and the wave propagation is from left to right. The particle displacement decreases exponentially through the depth.

The particle displacement decreases through the depth, which is measured to approximately one wavelength. The velocity of a Rayleigh wave is defined by Eq.2.3.

$$c_t = \frac{0.87 + 1.12}{1 + \mu} \cdot \sqrt{\frac{E}{\rho}\left(\frac{1}{2(1+\mu)}\right)} \qquad \textbf{(2.3)}$$

2.2.4 Love Waves

Love waves are named after the mathematician Augustus E H Love (Love [1911]). The particles oscillate in a shear motion perpendicular to wave propagation, as shown in Figure 2.4. Similar to Rayleigh waves, Love waves have a maximum particle

displacement on the outer surface gradually decreasing as the depth reaches one wavelength.

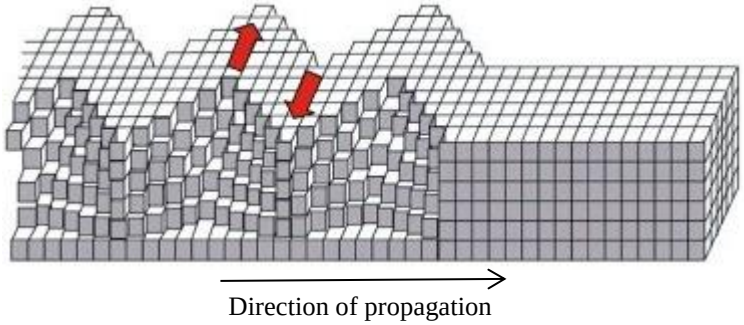

Figure 2.4. Love wave. Particles oscillate in a shear motion perpendicular to the wave propagation (left to right). The particle displacement decreases exponentially through the depth.

2.2.5 Lamb Waves

During the early 1900s, Horace Lamb investigated sound propagation through plates and discovered that there are a number of wave modes that can exist in a thin plate (Lamb [1917]). Thin plates are defined when the surface dimensions of a material are far greater than the thickness and when the thickness is in the order of one wavelength. Lamb waves require upper and lower boundaries in thin plates for guided wave propagation. Lamb waves consist of two fundamental wave modes mainly used for NDT, known as the Symmetric (S_0) and Asymmetric (A_0) Lamb waves, as shown in Figure 2.5. The S_0 wave mode is symmetrical through the top and bottom of the plate where the crests of the wave coincide with each other. The A_0 wave mode is where the waves on both surfaces are identical where the crest on one surface coincides with a trough. The propagation characteristics of a Lamb wave mode are dependent on the material properties, the frequency and the thickness of the plate (P_t).

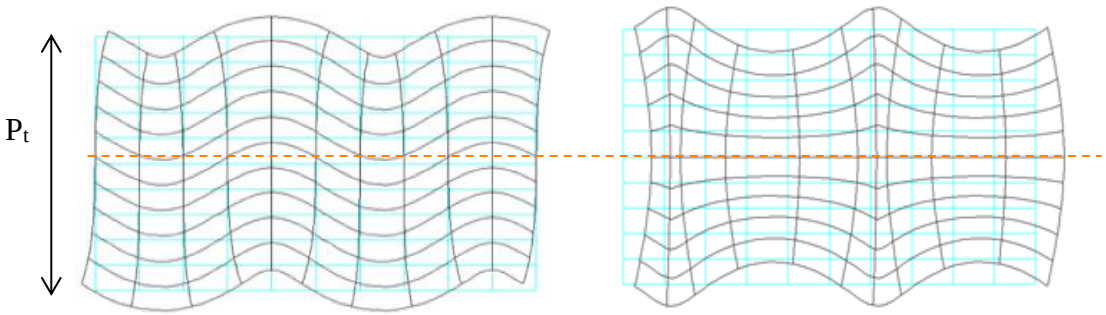

Figure 2.5. The fundamental Lamb wave modes. Asymmetric A_0 wave mode (left) and symmetric wave mode S_0 (right) showing the displacement pattern with respect to plate thickness (P_t). Created from Disperse software.

Another fundamental guided wave mode that can exist in plates is known as the shear horizontal wave. The shear horizontal wave (SH_0) is when the particle oscillation is in line with the plate surface and perpendicular to the direction of wave propagation. The particle displacement pattern is equally distributed through the thickness.

2.2.6 Cylindrical Guided Waves

The propagation of guided waves in pipes has been researched by many scientists and is discussed in chapter 3. However, one of the first was Gazis [1959a,b] who developed a characteristic equation showing wave mode characteristics. These include velocity and wavelength relationships and cut-off frequencies (the minimum frequency that a wave mode can exist). Considering Lamb waves in plates are determined by the plate thickness and a pipe is effectively a rolled plate, pipes have similar axisymmetric wave mode displacement patterns through the thickness. However, the sides are now constrained in a pipe providing the existence of additional non-axisymmetric wave modes. The wave modes in a pipe can be categorised into longitudinal, torsional and flexural wave modes, some of which are shown in Figure 2.6.

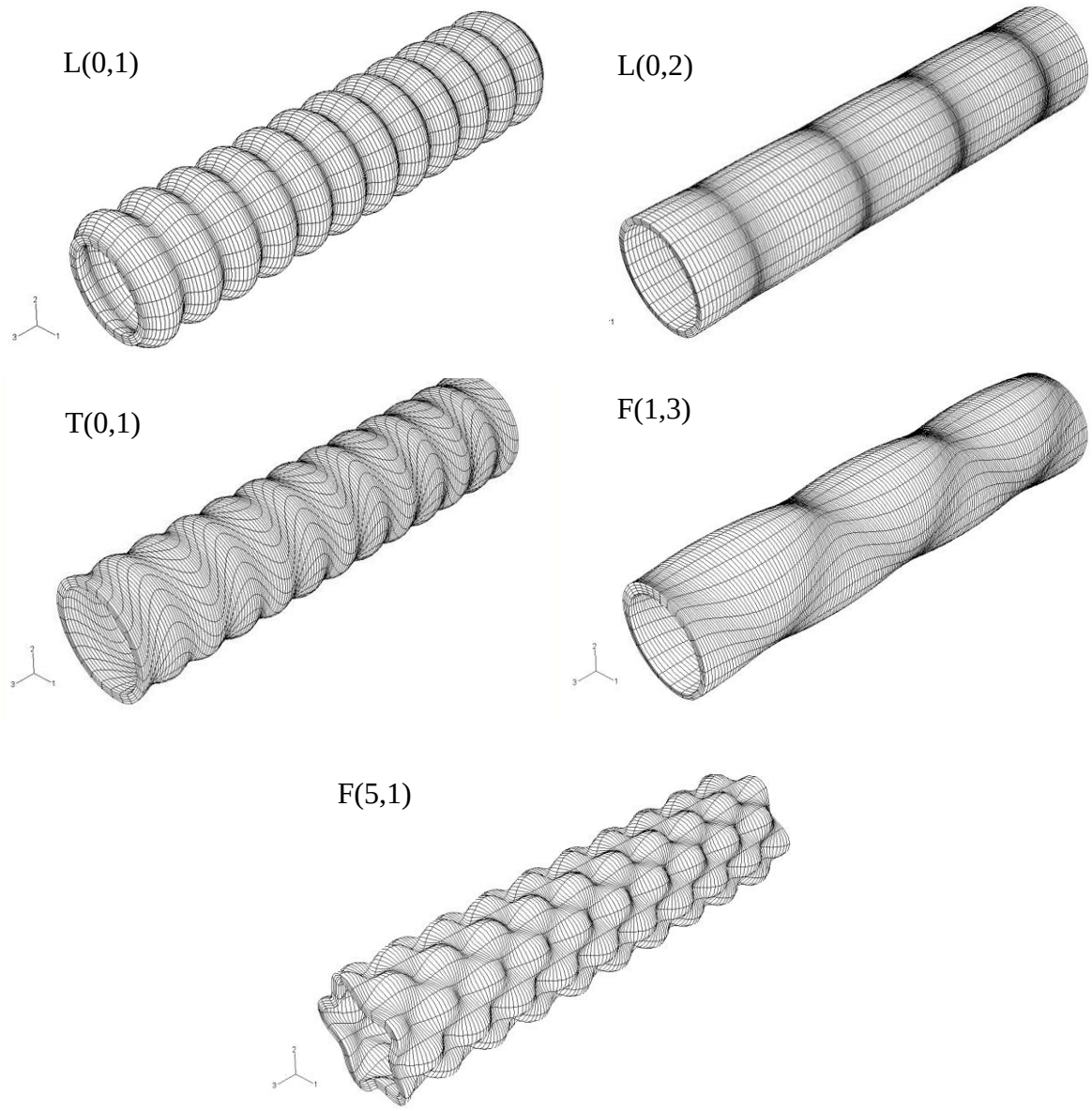

Figure 2.6. FEA representation of wave mode displacement patterns for L(0,1), L(0,2), T(0,1), F(1,3) and F(5,1). L(0,1) and F(5,1) have mainly radial displacement, T(0,1) has circumferential displacement, L(0,2) and F(1,3) have mainly axial displacement.

All wave modes can have circumferential, radial or axial displacement patterns and many consist of a combination of all three displacements. The three axisymmetric wave modes commonly used in guided wave inspection, L(0,1), T(0,1) and L(0,2), have mainly radial displacements, pure circumferential and mainly axial displacement respectively. L(0,1) and L(0,2) also have a relatively small amount of axial and radial

displacement respectively compared to their main displacement, whereas T(0,1) is purely circumferential. Flexural wave modes have a varying displacement pattern around the circumference, which are similar to the corresponding axisymmetric wave mode for a particular family (described in section 2.3). This nomenclature was formalised by Silk and Bainton [1979] and is discussed further in chapter 3 section 3.2.

2.3 Cylindrical Guided Wave Nomenclature

Guided wave modes in pipes are fundamentally axisymmetric or non-axisymmetric (flexural) around the circumference. The axisymmetric wave modes can either propagate in the form of torsional or longitudinal waves. There are orders of each wave mode, which are determined by their mode shapes e.g. first, second and third order torsional wave mode which denotes the number of sinusoidal variation around the circumference. The nomenclature for these wave modes are T(0,1), T(0,2) and T(0,3) whereby T is related to the wave mode type, which in this case is torsional (L if the wave mode is longitudinal). The first number in the brackets is the order of cyclic variation around the circumference of the pipe (which is zero in this case because torsional wave modes are axisymmetric) and the second number is a nominal index which corresponds with the order of the wave modes' cut off frequencies. The index is related to the cut-off frequency of the wave mode because higher order wave modes can only begin to exist at higher frequencies in comparison to previous indexes. With each axisymmetric wave mode there is a family of flexural wave modes based on their mode shapes and their velocity convergence towards a particular axisymmetric wave mode as frequency is increased. Flexural wave modes occur if the excitation is non-uniform around the pipe or if an axisymmetric wave interacts with a non-symmetric feature such as a localised defect. They are called flexural waves because on any one plane they cause a flexing motion of the pipe. The nomenclature is defined as F(a,b) similar to axisymmetric wave modes, whereby the only difference is that F refers to a flexural wave mode. For current guided wave testing commonly used for pipes in the oil and gas industry, the frequency range is below 100kHz and the three axisymmetric wave modes that can exist are L(0,1), T(0,1) and L(0,2).

2.4 Bandwidth and Signal Modulation

The bandwidth of a signal is a range of frequencies given by lower and an upper frequencies limits. Generally, time domain signals are used for guided wave inspection, however frequency domain signals are useful for determining the frequency content of a signal. A Fourier Transform (FT) is used to convert a time-domain signal into a series of amplitude and phase value pairs for a series of frequencies (based on the sinusoidal variations each frequency contributes to the signal). Fourier transform can be used to determine the bandwidth of a signal and is defined by the following equation, Su *et al.* [2006],

$$\boldsymbol{F(\omega) = \int_{-\infty}^{+\infty} f(t) e^{-jwt}} \qquad \textbf{(2.4)}$$

where $F(\omega)$ is the Fourier counterpart, ω is the angular frequency and j in the complex unit.

A modulated pulse is generally used in guided wave inspection to provide clear peak amplitude responses from reflections and reduce the bandwidth of the signal. The bandwidth of the signal is defined by the frequency range with less than a 32dB reduction in amplitude from the main lobe. This is defined as the Teletest Focus+ system noise level. A pulse is transmitted with a set number cycles to determine the time arrival of the signal. A Hann window is commonly used to modulate a signal and is implemented in the Teletest Focus+ system however, there are other similar windowing functions such as Gaussian and Hanning. The equation below modulates a sine wave with a Hann window,

$$\boldsymbol{y(t) = 0.5 sin(2\pi f_c t)\left(1 - cos\left(\frac{2\pi f_t t}{N}\right)\right)} \qquad \textbf{(2.5)}$$

where *y(t)* is the signal, f_c is the centre frequency, *t* is the time and *N* is the number of cycles. Figure 2.7 shows a Hann window applied to a 10 cycle 60kHz sine wave.

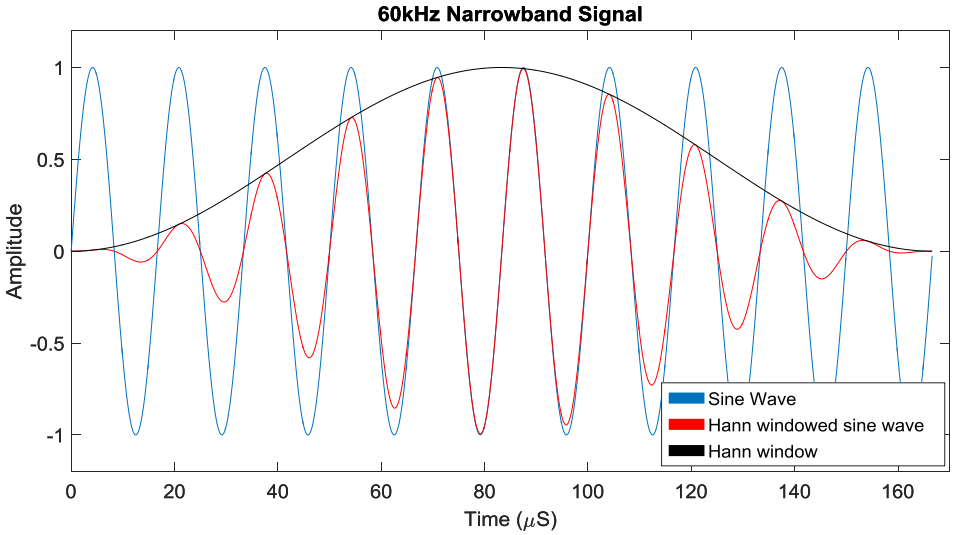

Figure 2.7. Sine wave and Hann windowed 60kHz 10 cycle signal.

In addition to the detectability improvement, a windowing function in comparison to a finite sine wave of the same duration increases the main lobe to side lobe ratio which is desirable for frequency control during transmission. Transmitting a single wave mode is common practice, which is achieved by reducing the bandwidth. The bandwidth of a pulse can also be reduced by increasing the number of cycles. To calculate the bandwidth of the pulse the following equation is used,

$$\boldsymbol{f_R = f_c \pm \frac{(2+k)f_c}{n_c}} \qquad \textbf{(2.6)}$$

where f_R is the frequency range, f_c is the centre frequency, *n* is the number of cycles of the pulse and *k*=0 corresponds to the main lobe of the bandwidth, whereby the subsequent *k*=1 and *k*=2 indicate the second and third lobes of the bandwidth

respectively. Figure 2.8 shows the bandwidth of a 60kHz sine wave and Hann windowed pulses with 10 and 20 cycles.

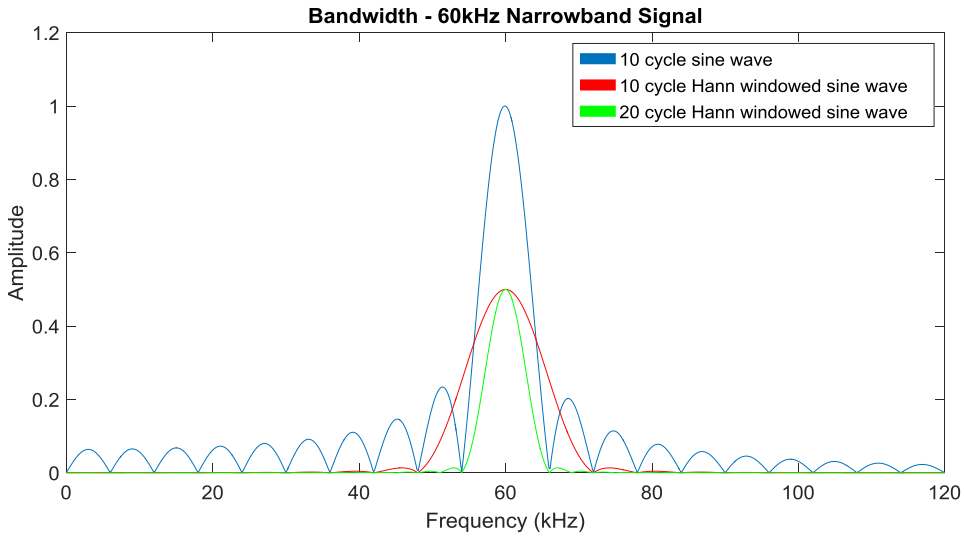

Figure 2.8. Frequency bandwidth of a sine wave and Hann windowed pulse at 60kHz.

Maximum amplitude is achieved when using a sine wave excitation, however the side lobes of the bandwidth are relatively large caused by the finite pulse length. The Hann windowed pulses have less amplitude around the centre frequency (60kHz) but they have less spectral leakage and by decreasing the bandwidth, it can be reduced further. A compromise has to be made between bandwidth and the number of cycles.

2.5 Phase and Group Velocity

When a continuous sinusoidal signal at a single frequency is excited the phase at any position is changing at the same rate. The rate at which this wave propagates is called the phase velocity. The pulses commonly used in guided waves described in section 2.4 have a finite length and contain a frequency range. The frequency components of the pulse can travel at different velocities causing the pulse to spread, a phenomenon known as dispersion (described in section 2.6). The velocity of a pulse can be described by the

phase velocity *(V_{ph})* or the group velocity *(V_{gr})*, which is the apparent velocity of the pulse. The relationship between V_{ph} and V_{gr} is given by the following (Krautkramer et al. [2013]):

$$\boldsymbol{V_{gr} = \frac{V_{ph}}{1 - \frac{f}{V_{ph}} . \frac{dV_{ph}}{df}}} \qquad \textbf{(2.7)}$$

The relationship shows that if V_{ph} does not vary with a change in frequency (f) then both V_{gr} and V_{ph} are equal. T(0,1) is the only fundamental wave mode used in guided wave inspection that has this unique relationship. Figure 2.9 shows how a pulse can propagate with a change in phase velocity and a change in group velocity.

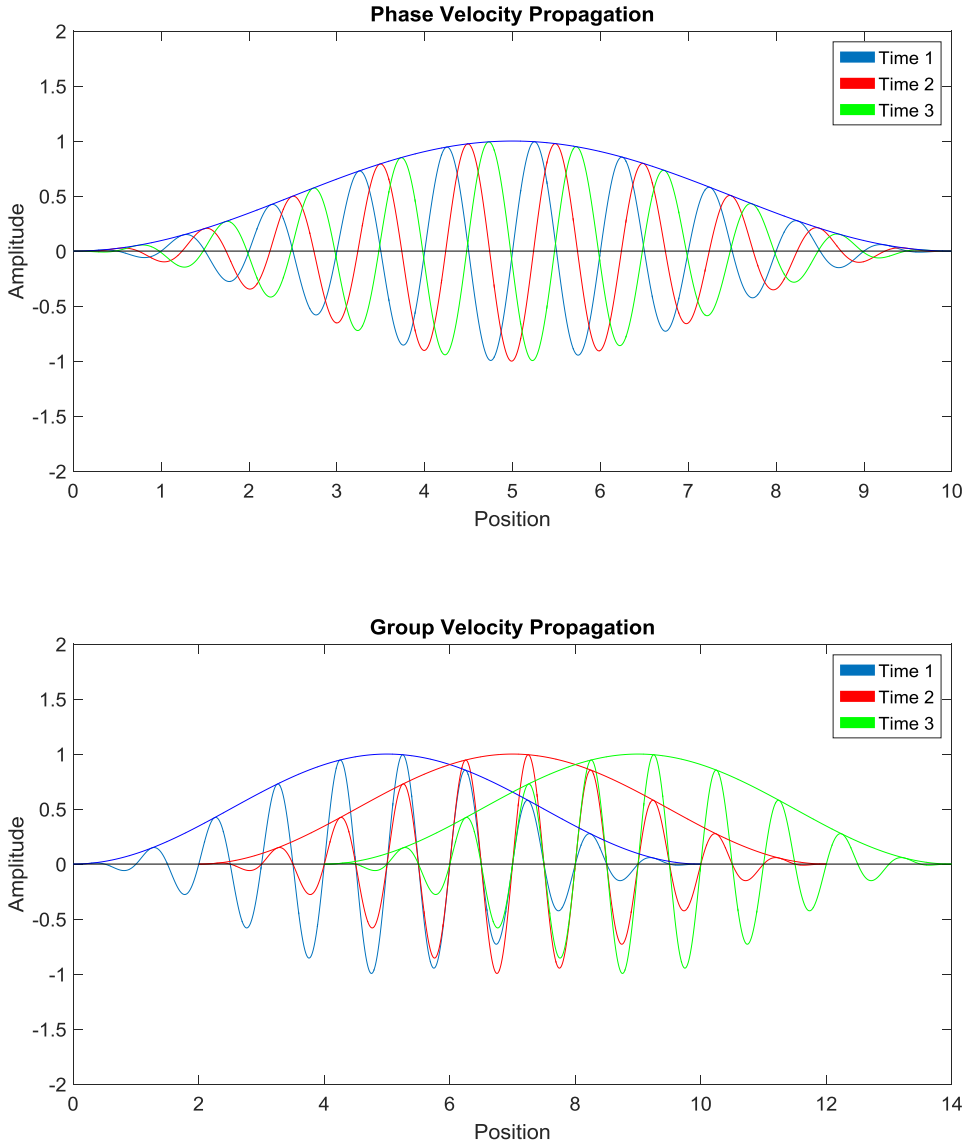

Figure 2.9. Phase velocity (top) with zero group velocity and group velocity (bottom) with no phase change.

2.6 Dispersion

Dispersion occurs when there is a difference in phase and group velocity. This difference causes a signal to spread out and change pulse shape. The greater the change in velocity the more dispersive a signal becomes. Dispersion is an undesirable effect for guided wave inspection because the spreading of the signal distorts the pulse shape, which can affect the peak to peak amplitude of the signal and also cause interference

with reflections. A reduction in amplitude can effectively reduce the signal to noise ratio of a signal making defects less likely to be detected. Considering that the modulated pulses used in guided wave testing have a frequency bandwidth, which is determined by the excitation frequency (centre frequency) and the number of cycles used, the dispersion characteristics become more complex. If a signal is dispersive, proportions of the signal will travel with different velocities at different frequencies, which can enhance the signal spreading and distort the pulse shape further. Therefore, it is important to conduct inspection using narrow band pulses in frequency ranges where wave modes are less dispersive.

Dispersion of wave modes is represented in graphs known as dispersion curves. Dispersion curves present the phase and group velocity of wave modes against frequency. This provides indication to wave mode characteristics at particular frequencies. Figure 2.10 shows dispersion curves for a 6 inch schedule 120 pipe for phase and group velocity against frequency. To calculate the dispersion curve of a particular pipe, a software named ‘Disperse’ was developed by (Pavalakovic *et al.* [1997]). This shows the relationship of each wave mode with respect to velocity and frequency. Therefore, at particular frequencies, wave modes can experience steep velocity gradients (towards their cut-off frequency) making them more dispersive because the difference in phase and group velocities is much greater towards the cut-off frequency.

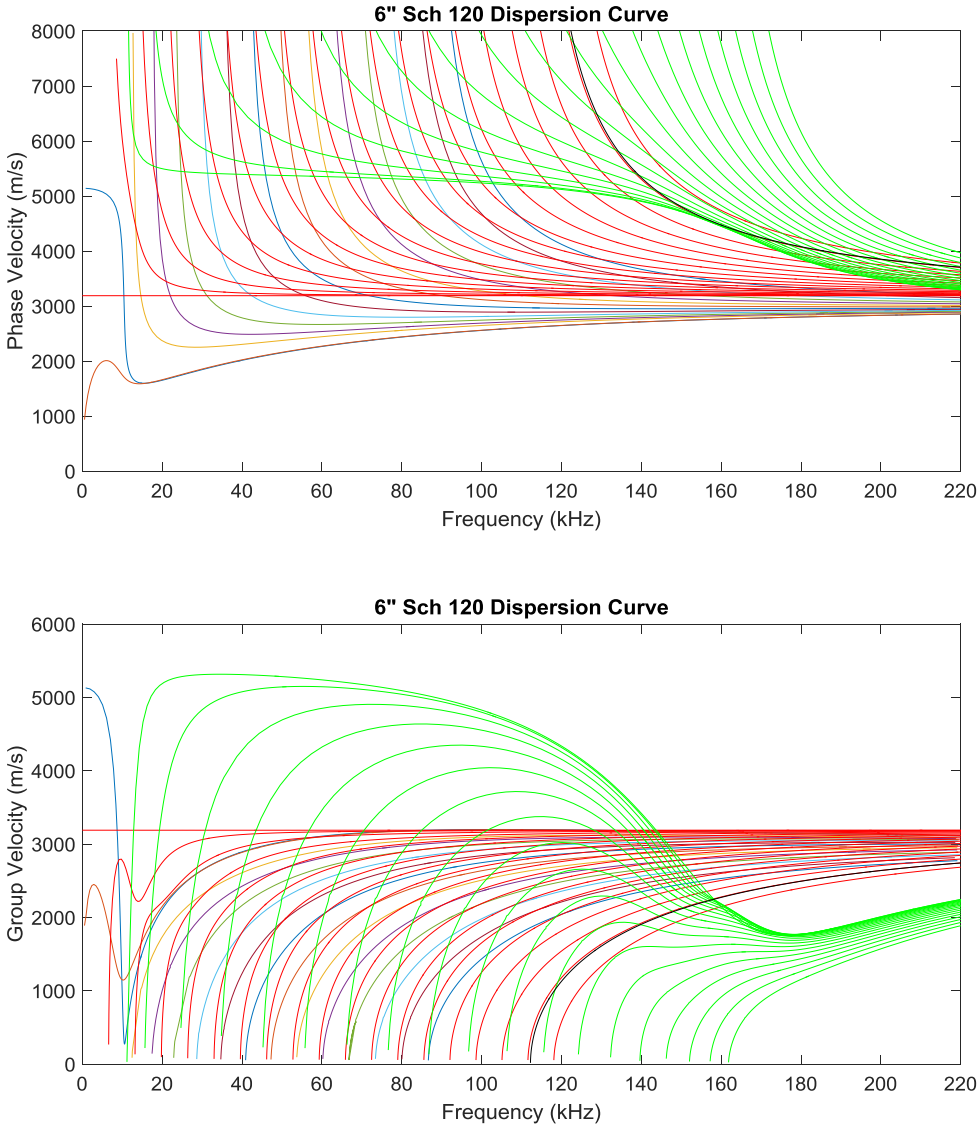

Figure 2.10. Dispersion curves showing phase velocity (top) and group velocity (bottom). L(0,1) wave mode family (blue), T(0,1) wave mode family (red), L(0,2) wave mode family (green) and T(0,2) (black).

2.7 Mode Conversion

Wave mode conversion occurs when a proportion of energy from a particular wave mode converts into another wave mode. This occurs when a propagating wave mode interacts with a boundary of different acoustic impedance in the direction of propagation or at an angle of incidence. The amount of energy that converts into another wave mode

from a feature or a defect also depends on the dimensions of this boundary. For guided wave inspection, the mode conversion usually occurs between the transmitted axisymmetric wave mode and the associated family of flexural wave modes. The dispersion curves in Figure 2.10 show the axisymmetric wave modes and their associated family of flexural wave modes.

3 LITERATURE REVIEW

3.1 Introduction

This chapter reviews previous research made in the field of guided waves. Authors including Helmholtz [1954], Rayleigh (or Strutt) [1885] and Lamb [1910] have researched ultrasound for over a century and development in the field has continued up to the present date. As the field developed further many researchers focused on guided waves. The areas reviewed in this chapter include an overview of the research conducted in guided waves and the application of this to pipe inspection. The following sections include a more specific review based on the technical areas investigated in this thesis, which include the modelling of guided waves, defect sizing and guided wave inspection using medium range frequencies.

3.2 Historical developments in guided waves

Ultrasonic guided wave theory was developed in plate structures by Lamb [1917] and guided waves in plates became known as Lamb waves. Worlton [1951] identified the potential of using Lamb waves for non-destructive testing by using the theory developed by Lamb and showed that an infinite number of wave modes can exist from plate vibration (Worlton [1961]). During the same time period Gazis [1959a]

investigated three dimensional wave propagation in hollow cylinders and developed a characteristic equation, which was followed by its computational numerical validation Gazis [1959b]. This provided velocity and frequency characteristics for longitudinal, torsional and flexural wave modes, which are present in a range of dispersion curves. Similar research based on the linear theory of elasticity was conducted on hollow cylinders by Ghosh [1923], McFadden [1954] and Hermann and Mirsky [1956], and rods by Pochhammer [1876] and Chree [1886], but their research was limited to axial symmetry of motion. The potential of Lamb and Rayleigh waves were further investigated for non-destructive testing which showed application of the theory to ultrasonic flaw detection for a variety of structures which includes tubular specimens or pipes Viktorov [1967]. During the same decade guided waves were researched in wires showing wave mode distortion at specific frequencies Meitzler [1961]. The key finding from this study is the notation for longitudinal, torsional and flexural wave modes which is continued to be used to the present date. This notation was used to annotate the wave modes exhibited in metal tubing and pipes by Silk and Bainton [1979] and their investigation showed the relationship between pipe modes and Lamb modes (or plate modes). A key feature highlighted in their research showed a direct relationship between the axisymmetric Lamb mode A_0 and the first longitudinal wave mode L(0,1), and a direct relationship between the symmetric Lamb mode S_0 and the second longitudinal wave mode L(0,2), based on their wave propagation characteristics. A preliminary investigation into the response between L(0,1) and L(0,2) with defects (saw cuts) showed promising echo responses from L(0,1), but it was highlighted that both wave modes needed further investigation with respect to their signal response from defects in tubular structures.

A decade later Böteger *et al.* [1987] developed an Electromagnetic Acoustic Transducer (EMAT) prototype system for inspecting ferritic tubes. The motivation behind the development of the system was based on the non-destructive inspection of tubes within the nuclear industry. Schneider [1984] previously provided specifications and tested components with specialised computer systems based on the regulations set by the Reactor Safety Commission. The EMAT system showed to be capable of detecting natural defects, but it was highlighted that further research was needed to estimate flaw sizes with respect to depth.

Following the need to inspect heat exchanger tubes in the nuclear industry Ditri *et al.* [1992] provided theoretical research based on using the mechanical energy from surface traction to generate guided waves in hollow cylinders, which compared amplitude response to loading conditions. A multi-element transducer around the circumference of the pipe was investigated and showed that a reduction in gap size reduces the excitation of non-symmetrical wave modes. This provided the foundation for transducer array design, particularly for transmitting axisymmetric wave modes used for identifying features and defects in tubular structures. Li *et al.* [2001] and Li *et al.* [2002] investigated multi-element transducer arrays by coupling angle probes equally spaced around the circumference a pipe. Both axisymmetric and non-axisymmetric wave modes were investigated, showing that by applying controlled uneven loading to the transducers specific flexural wave modes can be generated. Enhancing angle profile tuning showed that more energy could be focused on a defect which improves the signal to noise response. Although the signal to noise signal was improved, the signal responses were still very noisy and in order to generate the low frequencies needed for guided wave testing the angle probes used in the array were relatively large in size, which are relatively difficult to couple to the curvature of the pipe surface.

Showing the potential of guided wave inspection for defect detection, research institutes started taking particular interest in the technique and, with the rise in computer performance, research in the field began to grow rapidly in the 1990s. Imperial College began exploring Lamb waves in plates using angle probes Alleyne *et al.* [1992] and soon after developed a dry-coupled piezoelectric transducer for the purpose of detecting corrosion in chemical plant pipework using a circumferentially distributed array Alleyne *et al.* [1996]. The investigation was based on using L(0,2) over the more dispersive L(0,1) wave mode and provided clear amplitude responses over a distance greater than 15 metres. The transducer array was capable of supressing flexural wave modes enabling the detection of an artificial notch defect. During this period began the development of commercial systems which are discussed in the section 3.3.

3.3 Commercial systems using guided waves

The first commonly recognised commercial guided wave systems to enter the market were developed by Plant Integrity Ltd (a subsidiary of TWI Ltd), Imperial College (available at Guided Ultrasonics Ltd) and South West Research Institute (available at NDT consultants). All systems produced by each individual research centre operate using three vital components for their systems which are a pulser-receiver, transducer arrays and data analysis software. The systems are used to screen many metres of pipe from one location using a pulse-echo technique, which is capable of transmitting ultrasonic signals (or pulses) and receiving the reflected signals from features that create significant acoustic impedance change. All systems were developed to inspect corrosion in pipelines. It must be noted that all guided wave systems are used as a screening tool and signal responses from unknown features may require follow up inspection from other NDT techniques. This usually requires a localised conventional ultrasonic inspection in the areas identified from the guided inspection.

Teletest®Focus^{+} is a guided wave system currently available at Plant Integrity Ltd and is the fourth generation developed from the original system. The original system was used to inspect pipelines for corrosion approximately 30 years ago (Mudge *et al.* [1996] & Mudge *et al.* [1997]). During this period dry-coupled piezoelectric transducers were developed and successfully tested for the purpose of generating Lamb waves by Alleyne *et al.* [1994]. Dry-coupled transducers were then developed and incorporated into the Teletest Focus^{+} for transmission and reception. A variety of transducer mounting mechanisms are available for different pipe diameters ranging from 2-24 inches (collars can be interlinked for larger pipe sizes up to a maximum pipe diameter of 48 inches). The collars consist of a carbon fibre housing with an internal inflatable bladder used to apply pressure to the transducers and sufficiently couple them to the pipe surface. The system can perform both L(0,2) and T(0,1) wave mode inspection, which is determined by transducer orientation and the use of more than one ring of transducers around the circumference of the pipe. The conventional arrangement is to have a multimode setup, which consists of three rings of transducers orientated in the longitudinal direction and two rings of transducers orientated in the torsional direction. Three rings are used in the

longitudinal configuration to suppress the more dispersive L(0,1) and provide unidirectionality for L(0,2). Two rings are used in the torsional configuration to provide unidirectionality for T(0,1). Teletest Focus$^+$ is used for guided wave research at TWI Ltd and this pulser-receiver system was used for the experiments conducted in chapter 5.

The Wavemaker®G4 guided wave system is available at Guided Ultrasonics Ltd (GUL), which was developed by Imperial College. This guided wave system performs guided wave inspection using dry-coupled transducers (Alleyne *et al.* [1994]) similar to those used in the Teletest Focus$^+$ system. The transducers are also deployed using an inflatable bladder in a configuration of two rings, which provides unidirectionality for T(0,1).

The MsSR®3030R guided system was developed by South West Research Institute. This system use magnetostrictive sensors to transmit and receive ultrasonic signals. Similar to Teletest Focus$^+$ the system can either deploy two or three rings to control torsional and longitudinal wave modes respectively. Rather than using piezoelectric transducers a magnetostrictive array consists of ferromagnetic strips wrapped around the circumference of a ferromagnetic pipe. Whereas a piezoelectric transducer converts electrical into mechanical energy to transmit a wave and vice versa to receive the wave, a magnetostrictive strip converts the energy in the magnetic field into mechanical energy and can detect time varying stresses or strains in the ferromagnetic material Kwun *et al.* [1998].

More recent systems have been developed for guided wave inspection. Table 1 lists details and fundamental specifications of each system.

Table 1. Commercially available guided wave systems.

Guided Wave System	Frequency Range	Propagation Distance	Transducer Type	Supplier
Teletest®Focus+	20-100kHz	60m	Piezoelectric	Plant Integrity Ltd
Wavemaker®G4	15-80kHz	60m	Piezoelectric	Guided Ultrasonics Ltd
MsSR®3030R	2-250kHz	Not specified	Magnetostrictive	NDT-Consultants Ltd
Temate®	0.1-1MHz	5m	EMAT	Innerspec Technologies Inc.
PowerFocus™	20-85kHz	150m	Piezoelectric	Structural Integrity Associates Inc.
UltraWave®	15-85kHz	90m	Piezoelectric	Olympus Cooperation

3.4 Analytical and Finite Element Methods (FEM) for guided waves

The combination of analytical and finite element methods was presented by Koshiba *et al*. [1984] for Lamb wave scattering in an elastic plate wave. The investigation of Lamb wave scattering was previously investigated by (Rokhlin [1980a], Rokhlin [1980b]) using a Weiner Hopf method, which could be applied to regular shape defects but difficult to apply to irregular shaped defects. However, the results using analytical and finite element analysis showed to be capable of analysing the scattering of Lamb wave modes with respect to irregular shaped defects.

Almost two decades later Moser *et al.* [1999] showed that the commercially finite element code ANSYS 5.3 [2013] can be used to simulate two-dimensional guided wave propagation. The results for a plate and ring structure were validated with analytical solutions (Viktorov [1967] and Graff [1975]) and compared to experimental results. This research also highlights the importance of mesh size and boundary conditions to simulate real scenarios and provide sufficient temporal resolution from the results.

To analyse the wave propagation in pipe and rails (Sanderson *et al.* [2002], Sanderson *et al.* [2003]) developed three dimensional finite element models using the commercially available ABAQUS Explicit [2012]. The model was used to propagate L(0,2) wave modes and results were presented for notch defects comparing the reflection against increasing a range of defects with partial circumferential lengths with varying depths and axial lengths. During the same period Zhu [2003] investigated finite element methods for generating L(0,1) and L(0,2) wave modes in hollow cylinders using time delay periodic ring arrays. The technique was successful in transmitting each wave with unidirectionality for both wave modes. A variety of defects investigated showed that the reflection coefficients from the axisymmetric wave modes were linear with respect to circumferential extent and were non-linear for change in the depth. The reflection coefficients for mode converted signals were analysed showing the impact of circumferential extent and depth of defects. Hayashi *et al*. [2003] used a semi-analytical finite element method to show dispersion and multimode existence in a plate and pipe. Visualisations of the propagating wave modes are depicted on sets of images for different time intervals showing the effect of dispersion, multimode signals and the mode converted images from pipe elbows. Bartoli *et al.* [2005] used ABAQUS Explicit to investigate the results from transversely type defects in rail tracks. The excitation signal was simulated on an instrumented hammer pulse and the results from the finite element analysis were compared to an experiment. A study of mesh refinement was conducted at various frequencies to sufficiently model mode conversions and evanescent modes.

Hosten *et al.* [2005] presented two finite element methods for guided wave propagation using FEMLAB [2004] software (renamed in 2005 to COMSOL Multiphysics [2012]).

Two dimensional finite elements methods were presented for analysing two structures with weak interfaces. The results were validated by comparing the transmission coefficients to experimental measurements. Rudd *et al.* [2007] implemented the elastodynamic finite integration technique for guided wave propagation in pipes. Results based on the interaction of defects and complex pipe bends were validated with experimental and simulated data using COMSOL Multiphysics [2012].

Bartoli *et al.* [2006] presented a semi-analytical finite element (SAFE) method for arbitrary cross-sections. The main difference of this technique in comparison to other SAFE methods is incorporating viscoelastic properties, which provided the energy, velocity and attenuation curves. The technique was applied to anisotropic viscoelastic layered plates, composite-to-composite adhesive joints and railroad tracks, which were validated to alternative more complex method using the superposition of bulk waves by Lowe [1995].

Ratassep *et al.* [2006] developed an analytical wave propagation model to investigate the longitudinal wave modes in an infinite pipe. Dispersion curves are presented for a number of pipe diameters and a wide range of frequency thickness products to include higher order longitudinal wave modes.

Drozdz [2008] presented two dimensional guided wave propagation using commercially available ABAQUS and COMSOL packages. Mesh parameters, absorbing elements, local mesh refinement and modelling defects were analysed. ABAQUS/Explicit was used for time-domain analysis and ABAQUS/Standard and COMSOL Multiphsyics were used for frequency domain analysis.

Zhou *et al.* [2009] developed a hybrid wave finite element (WFE) and finite element technique to analyse elliptical defects using L(0,2) and T(0,1) wave modes. Energy conservation laws are applied to the power flow of the incident and scattered wave modes to validate numerical methods.

Velichko *et al.* [2009] investigated the relationship between plate and pipe solutions. An infinite plate was modelled to represent the pipe and a forced 3D method was applied. The scattering of the guided wave modes were compared to the plate and pipe solutions for through thickness type defects.

Sanderson [2012] developed a hybrid finite modelling technique for three dimensional wave propagation in pipes. The technique is useful for analysing the excitation arrays and was compared to full ABAQUS Explicit models.

Overall, many different modelling techniques have been developed for guided propagation. From review ABAQUS Explicit is most commonly used for guided wave propagation in pipes. The results for a variety of scenarios have been validated using experimental results particularly for defect analysis. Therefore, ABAQUS Explicit was deemed as the suitable FEM for conducting the defect analysis conducted in chapter 6.

3.5 Defect sizing for guided waves in pipes

During the 1990s Imperial College investigated the reflection coefficients of fully penetrated notches with varying circumferential lengths Lowe *et al.* [1998]. The analysis was based on the reflections of L(0,2) and the mode converted flexural wave modes. The results were validated by comparing finite element modelling and experimental data. Following from this research further defect profiles were investigated using both L(0,1) and L(0,2) by Cawley *et al.* [2002], which included varying defect depth, circumferential extent and axial length. The majority of the results presented were from finite element analysis with some predictions validated experimentally. A similar investigation was carried out by Demma *et al.* [2003] by analysing T(0,1) and the flexural wave mode responses that are present from mode conversion. From the publications mentioned in this paragraph Demma *et al.* [2004] used the results to present a method for predicting the depth and circumferential extent of a notch using an arbitrary axial length. The method is based on the amplitude ratio of

the axisymmetric and flexural wave mode responses from notch type defects and proposes an approximate formula which can extrapolate the results for other pipe diameters. Catton [2009] and Sanderson [2012] further investigated defect sizing using the ratios of T(0,1) and flexural signal response for a variety of notch type defects, as well as the presence of multiple flaws.

In parallel to the research conducted by Demma *et al.* [2004] other researchers were developing other techniques for defect sizing. Mu *et al.* [2007] investigated defect sizing by utilising focusing techniques previously explored by Li *et al.* [2002] and Rose *et al.* [2003]. The technique applies different amplitude and time delays to the circumferential transducer array around the pipe which can focus and enhance the guided wave energy to a chosen location. Catton *et al.* [2008] and Mudge *et al.* [2008] used a combination of amplitude responses and focused responses for angular distribution in order to quantify defects in a classification scheme based on severity. A widely distributed defect with low amplitude would be low priority, whereas a defect with a high amplitude response and a narrow angular profile would be high priority.

Carandente *et al.* [2010] began investigating axisymmetric defects with varying depth profile for T(0,1). The taper angle and length of the defects were varied and the analysis was based on the ratio between axial length and wavelength. However, this method is limited to defects with an increased taper angle and a decreased length because in order to obtain high values for the ratio between axial length and wavelength requires operating at higher frequencies, which was limited in this analysis by the cut-off frequency for T(0,2). Carandente *et al.* [2012] investigated more complex defect profiles to estimate the maximum depth. The majority of the simulated defects were estimated to within a range of 20% depth error. However, the technique is limited to defect profiles with sharp changes and is less accurate for defect profiles with gradual change.

3.6 Medium and high frequency guided waves in pipes

Li *et al.* [2002] used the angle beam method to investigate the operation at frequencies above conventional guided wave systems, which is approximately 100kHz. A circumferential array was designed from angle beam transducers designed to transmit longitudinal wave modes. The transducer array was capable of detecting defects close to the array (less than 1.3 metres), but the results were noisy and the setup was incapable of detecting a defect with a depth of 50% at a distance of approximately 3 metres. To maximise the chances of detecting the defect a conventional full array transmission test was conducted at a relatively high frequency of 500kHz in order to reduce the wavelength and increase defect sensitivity, but was unsuccessful in detection. Nevertheless, the analysis was still based below the higher order longitudinal wave modes, as the cut-off frequency for the higher order L(0,3) wave mode on the pipe tested was approximately 600kHz and is therefore not considering higher order axisymmetric wave modes for inspection . Using the same system Sun *et al.* [2002], Zhang [2005] and Zhang *et al.* [2006] investigated high frequency non- axisymmetric wave mode focusing techniques to enhance resolution from defects. Although the frequencies (200-800kHz) used in this analysis are in the region where higher order axisymmetric wave modes exist, frequency and circumferential angle tuning has been used to excite only the L(0,1) wave mode family. The results showed an improvement in signal to noise ratio however to achieve these results a defect would need to be visible from a conventional transmission inspection. Otherwise energy would need to be focused in multiple areas on the pipe to ensure full coverage, which is time consuming. Yoon *et al.* [2010] conducted similar experiments to that previously mentioned by Li *et al.* [2002] using the angle beam method. The analysis was taken further by investigation of the higher order wave modes, but was only capable of detecting defects with L(0,1). A noisy signal was experienced similar to that of Li and Zhang and only a defect of 50% depth was clearly indicated in the signals.

Kannan *et al.* [2007] investigated the effect of frequency on defect sensitivity of T(0,1) for a range of notches and drilled holes. Magnetostrictive tape was used to construct a circumferential array and frequency range of 0-500kHz was tested, which showed an

optimum testing range of 70-225kHz for this particular pipe. Above this range higher order wave modes are excited providing complex multimode signals. Therefore, any frequencies above the cut-off frequency for higher order axisymmetric wave modes were ignored.

Kwon *et al.* [2010] investigated suppressing higher order wave modes to transmit a purer T(0,1) at higher frequencies. The results showed that the technique was capable of suppressing higher order torsional wave modes at frequencies where they exist. However, the technique requires a test pipe that is attached with a couplant to the end of the pipe under inspection. The test pipe has a thinning region so that only T(0,1) can propagate beyond this region and into the pipe under inspection. Kwon *et al.* [2015] investigated sloping angle of the thinning region to determine the leakage of higher order wave modes beyond this region and the results showed that a slope angle of 0 degrees provide the least leakage. Although the results were promising this technique is not a viable solution, as it requires access to the end of the pipe which is uncommon in the field and a number of test pipes to test a range of pipe sizes. Similar to previous publications mentioned in this section the objective has been to eliminate higher order wave modes rather than investigate them.

Cho *et al.* [2010] and Kim *et al.* [2011] research is based on the generation of torsional wave modes. Magnetostrictive transducers were developed using a meander coil to produce a torsional wave mode in the MHz range using a pitch-catch configuration. The results showed that defect sensitivity was increased for the higher frequency by comparing 150kHz to 1 MHz tests. In this analysis the T(0,2) wave mode appears as a widely spread low amplitude noisy signal, which is caused by operating at a frequency (1MHz) where it exhibits high dispersion.

3.7 Summary

The purpose of the literature review was to identify the gaps in knowledge that could be investigated for improving guided wave inspection. The research into guided waves began over a century ago and has recently become a technique used for inspecting the conditions of pipes. Defect sizing is a popular area of research, but so far has been limited to low range frequencies. Operating at higher frequencies can increase defect sensitivity, spatial resolution and can increase the minimum inspection range which are improvements to the current guided inspection techniques. Some research has previously been conducted at frequencies above 100kHz however, the range was still limited to operating frequencies below the higher order wave modes and there is lack of research on defect sizing at medium range frequencies. Therefore, chapter 4 designs a setup that can be used in both experimental and modelling analysis for the purpose of defect analysis at medium range frequencies.

4 DESIGN OF SETUP FOR EXPERIMENTAL AND FINITE ELEMENT ANALYSIS USING NARROW AND BROADBAND SIGNALS AT MEDIUM FREQUENCIES FOR DEFECT SIZING

Introduction

This chapter describes the development of the setup used to conduct all the experiments and finite element analysis presented in the following chapters. The main aim is to design a procedure to separate all wave modes in order to measure the reflection coefficients, which is used for defect sizing in chapter 6. Reflection coefficients have been used as a method for quantifying signal responses from defects at low range frequencies by Lowe *et al.* [1998], Cawley *et al.* [2002], Demma *et al.* [2003], Catton [2009] and Sanderson [2012]. However, to the best of the author's knowledge, there has

been no research presented in the literature providing methods on defect sizing using higher order axisymmetric wave modes. Considering that reflection coefficients have been researched for the purpose of defect sizing for guided wave testing at low frequencies, the same approach has been used in this research and adapted to medium range frequencies.

The investigation was based on operating in a frequency range where T(0,2) exists and where dispersion is minimised in order to maintain an adequate pulse shape. The criteria for measuring the reflection coefficients were based upon the pipe geometry, transmitter, receiver and defect location. The pipe geometry determined the operating frequency range for this analysis and was carefully selected based on the frequency range constraints of the Teletest Focus+ pulser-receiver (see appendices section 9.1 for technical specifications). The positioning of the transmitter, receiver and defect was used to provide wave mode separation for individual wave mode analysis, which includes the mode converted signals from the defects.

Other techniques were also developed in order to improve the efficiency of the finite element analysis, which included designing modified pipe segment models allowing more defect sizes to be analysed and reduce processing times. Another technique developed is the effective use of broadband signals to provide a wide frequency spectrum from one model. This significantly reduces the number of models needed providing a more efficient method for investigating multiple frequencies using FEA, which is described in chapter 6.

4.1 Pipe Geometry

In order to determine the optimum pipe geometry the dispersion curves for various pipes available for testing were analysed. The dispersion curves provide the cut-off

frequency for each wave mode and the extent of the dispersion at a particular frequency. The criteria influencing the choice of pipe dimensions are:

- The ability to excite T(0,2) at a suitably low frequency to comply with the pulser-receiver's working range.
- A pipe that can be feasibly machined to create axisymmetric defects considering weight and diameter.
- A pipe length long enough to allow T(0,1) and T(0,2) to separate for individual wave mode analysis.
- To ensure the bandwidth of the pulse does not significantly excite in the dispersive region of T(0,3).

A range of 9 pipe sizes were investigated and the frequency range for each size was determined. The pipes sizes are defined using Nominal Pipe Size (NPS) standards describing the inner diameter in inches and the thickness described by another non-dimensional number defined by a schedule. Dispersion curves have been plotted for nominally 2, 3, 4 and 6 inch pipes each with different thicknesses shown in Figure 4.1. The curves represent the torsional wave modes T(0,1), T(0,2) and T(0,3) and the dashed lines provide a frequency range. A 20 cycle Hann windowed pulse (the maximum selectable setting in the Teletest Focus+ software) was used to provide the smallest bandwidth and the maximum possible frequency range. The range is based on the first side lobes of the bandwidth starting after the T(0,2) cut-off frequency and ending before the T(0,3) cut-off frequency. Equations 4.1 and 4.2 were used to determine the centre frequencies (Fc) for the start and end of the range, derived from Eq. 2.6 in chapter 2.

$$\boldsymbol{F_{c1} = \frac{nF_{T02}}{n-k-2}} \qquad \textbf{(4.1)}$$

$$F_{c2} = \frac{nF_{T03}}{n + k + 2} \quad \textbf{(4.2)}$$

where F_{c1} and F_{c2} are the centre frequencies for the beginning and end of the frequency range respectively, F_{T02} and F_{T03} are the cut cut-off frequencies for T(0,2) and T(0,3) respectively, n is the number of cycles of the pulse and k=0 corresponds to the main lobe of the bandwidth, and k=1 was used to include the first side lobes of the bandwidth to reduce the excitation of T(0,2) and T(0,3) in the dispersive regions.

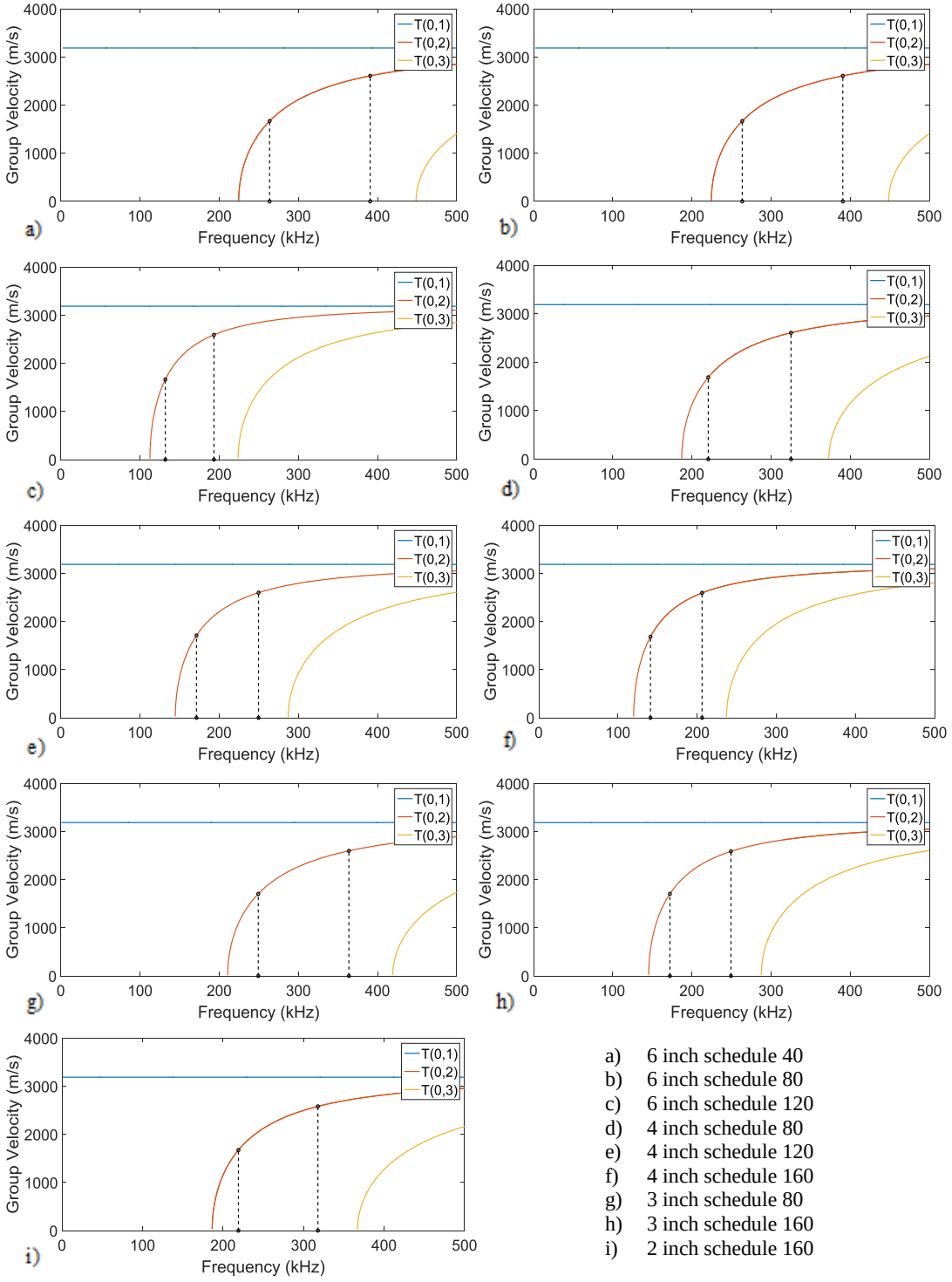

a) 6 inch schedule 40
b) 6 inch schedule 80
c) 6 inch schedule 120
d) 4 inch schedule 80
e) 4 inch schedule 120
f) 4 inch schedule 160
g) 3 inch schedule 80
h) 3 inch schedule 160
i) 2 inch schedule 160

Figure 4.1. Dispersion curves showing group velocity against frequency for torsional wave modes. Dashed lines indicate frequency range based on the first side lobes of the bandwidth starting after the T(0,2) cut-off frequency and ending before the T(0,3) cut-off frequency.

These figures show that as the thickness increases the cut-off frequency for T(0,2) and T(0,3) is reduced. Increasing the thickness of the pipe also reduces the frequency range of operation because the cut-off frequencies for T(0,2) and T(0,3) become closer together. These are important factors when considering the pipe size because operating at a point where the gradient of T(0,2) in the dispersion curve is smaller (maximum frequency in the range) suggests a less dispersive signal, but this is also frequency dependent. Operating at a higher frequency increases the bandwidth of the signal and can excite a higher number of frequencies, whereby the lower frequencies in the range can excite dispersive regions of T(0,2).

To investigate a suitable pipe size, the pipe size with the lowest frequency range and the pipe size with the highest frequency range were considered. The pipe with lowest frequency range and with the lowest maximum frequency of operation is the 6 inch schedule 120 and the pipe with the maximum is the 6 inch schedule 40. Figure 4.2 shows that the 6 inch schedule 120 (actual diameter 168.3mm and wall thickness 14.3mm) has the least dispersive signal at 190kHz (maximum frequency in the testing range) and the 6 inch schedule 40 (wall thickness 7.11mm) has the most dispersive signal at 390kHz over a 12 metre propagating distance (round trip signal for a 6 metre pipe). The gradient represents the change in velocity against frequency, providing a value that can be used to compare dispersion at a particular frequency, i.e. the higher the gradient the more dispersive the wave mode is at a particular frequency. Although a 6 inch schedule 40 had the lowest gradient the bandwidth was large enough to excite more of the dispersive region of T(0,2) in comparison to a 6 inch schedule 120. The results for all 9 pipe sizes are show in Table 2.

The last consideration is the weight of the pipe and all pipes examined met the loading criteria (that is being less than 1/2 tonne) of the lathe used to machine the axisymmetric defects around the pipe circumference.

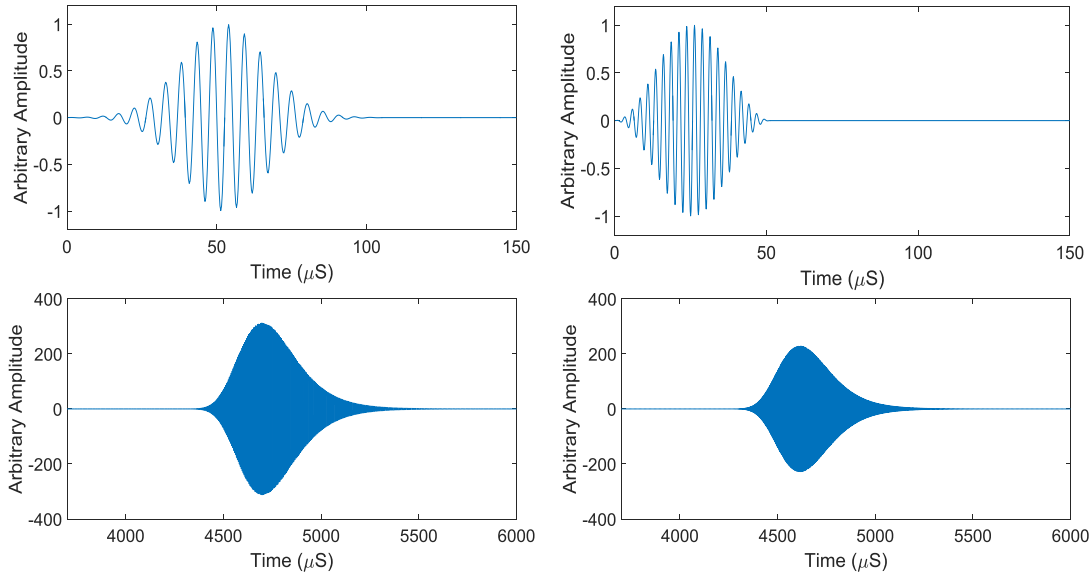

Figure 4.2. Transmitted pulse at 190kHz (top left) and 390kHz (top right). T(0,2) pulse shape for 12 metres propagation in a 6 inch schedule 120 pipe at 190kHz (bottom left) and a 6 inch schedule 40 pipe at 390kHz (bottom right).

Table 2 shows a summary for the results of each pipe investigated and the most suitable pipe size for conducting the experiments is a 6-inch schedule 120. This pipe size has the lowest operating frequency to investigate T(0,2) and this extremely important firstly because the signals have greater sampling due to the Teletest Focus+ system having a maximum sampling frequency of 1MHz, secondly the system has a greater and more uniform voltage output at lower frequencies. Although the frequency test range is the narrowest compared to all the pipes investigated there is still a significant frequency bandwidth range of 58kHz.

Table 2. Nominal pipe sizes and their charactersitics. Values in the brackets for the frequency range indicates the number of single frequencies in the range for 1kHz steps.

Nominal Pipe Size (NPS)	Diameter (mm)	Thickness (mm)	Frequency Range (kHz)	Mass (kg/m)	Gradient at max frequency (ms^{-1}/kHz)
6'' Sch 40	168.3	7.11	263-390 (127)	28.26	3.62
6'' Sch 80	168.3	10.97	171-250 (79)	42.56	5.32
6'' Sch 120	168.3	14.27	132 -190 (58)	54.2	6.88
4'' Sch 80	114.3	8.56	220-324 (104)	22.32	3.98
4'' Sch 120	114.3	11.13	171-249 (78)	28.32	5.27
4'' Sch 160	114.3	13.49	141-206 (65)	33.54	6.43
3'' Sch 80	88.9	7.62	249-364 (115)	15.27	3.57
3'' Sch 160	88.9	11.13	171-249 (78)	21.35	5.37
2'' Sch 160	60.33	8.74	219-218 (99)	11.11	4.17

4.2 Experimental Setup

The experimental setup is based on separating T(0,1) and T(0,2) to identify their individual signal responses. This includes analysing the amplitudes of the incident wave, the reflection from the defect and the pipe end for both wave modes. Considering that the pipe chosen for the experiments is a 6 inch schedule 120 the dispersion curve for this pipe needs to be analysed further in order to identify the group velocity difference for T(0,1) and T(0,2) at a particular frequency. This difference in frequency, the number of cycles used for excitation, the positioning of the transducer array and receiver (Polytec PSV-400-3D-M Scanning Laser Vibrometer Polytec [2009]) are all factors that need investigation in order to sufficiently separate the wave modes for all signals received in the A-scan. The first step is to investigate whether it is possible to set up an

experiment where T(0,2) is least dispersive. The conditions that meet this criterion are to operate at the maximum frequency in the range determined by the dispersion curve shown in Figure 4.3.

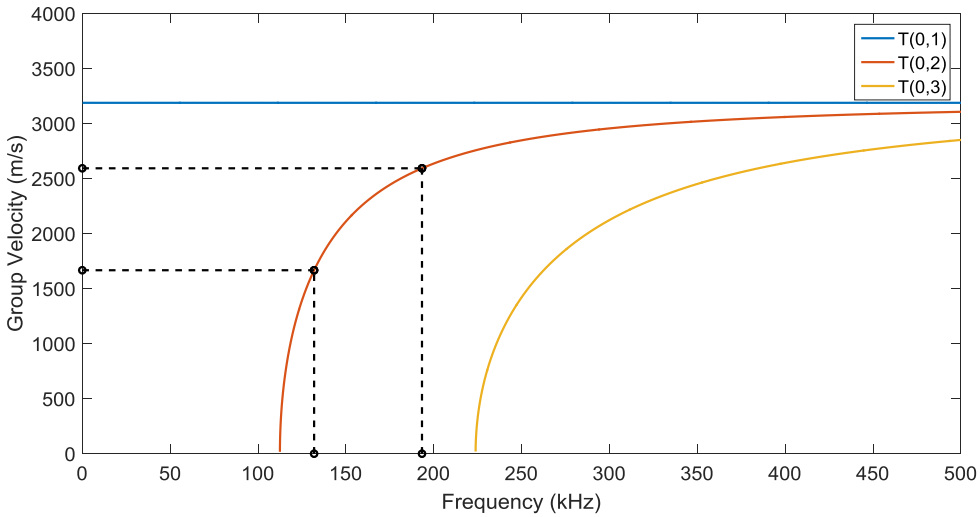

Figure 4.3. Dispersion curve showing group velocity against frequency for a 6 inch schedule 120 pipe. Dashed lines indicate frequency and velocity range.

The other factor that reduces dispersion is to operate with the highest number of cycles possible (20 cycles is the maximum selectable option with the Teletest®Focus+ system). Increasing the number of cycles in the pulse reduces the bandwidth according to Eqn. 2.6 in chapter 2. The number of cycles can be increased above 20 cycles if input waveforms are changed. This will reduce the dispersive nature of the pulse, but consequently increase the pulse length. Dispersion simulations were run and it was found that with 20 cycles the influence of dispersion on the pulse width after a propagation distance of 12 metres was acceptably low.

Both T(0,1) and T(0,2) are generated simultaneously and wave mode conversion occurs at an axisymmetric defect between both wave modes to create 4 reflected pulses (mode conversion is described in chapter 2 section 2.7). Part of the energy of T(0,1) converts

into T(0,2) and vice versa for T(0,2). Therefore, positioning of the transmitter, receiver and defect location were important parameters for separating both the incident and reflected wave modes in order to calculate the reflection coefficients. The location of these features was determined by the time arrival of the incident wave modes, reflected wave modes and the mode converted signals. This was based on the velocities of the T(0,1) and T(0,2) at the upper frequency range of 190kHz and the propagation path. Figure 4.4 shows the setup used to conduct the experiments and Figure 4.5 shows the wave mode separation using data extracted from 'Disperse' software (Pavlakovic [1997]), based strictly on time arrivals without taking relative amplitudes or dispersion into account at this stage.

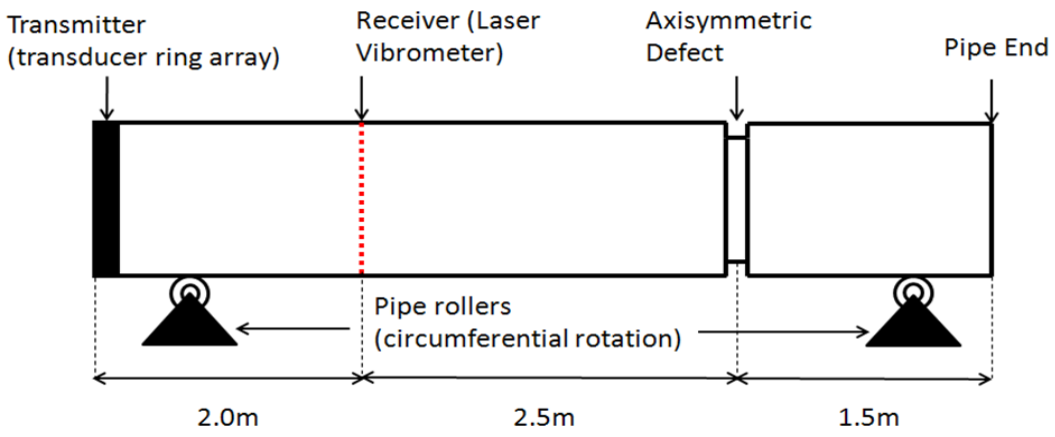

Figure 4.4. Experimental setup showing transmitter, receiver and defect positions.

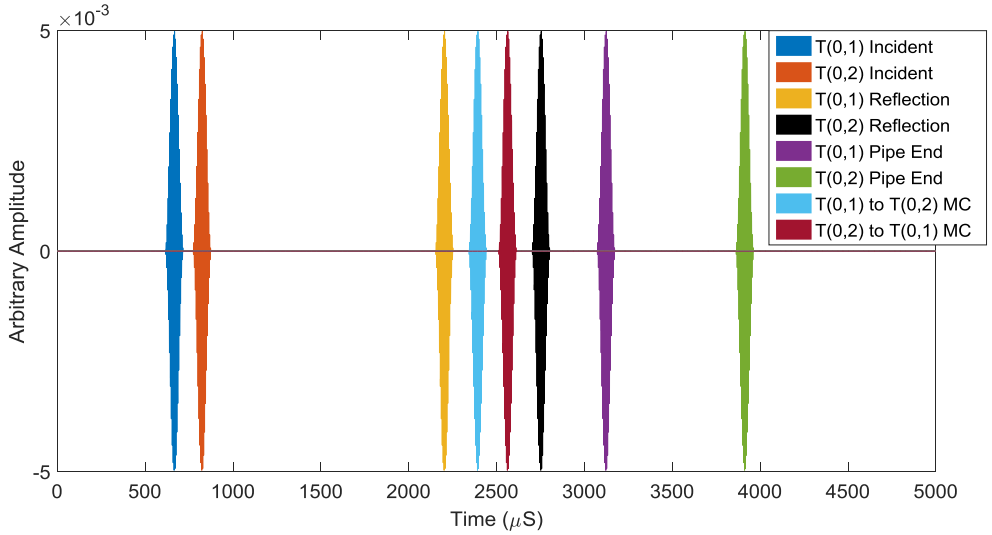

Figure 4.5 Predicted time arrivals of T(0,1) and T(0,2) assuming no dispersion or energy loss. Note that MC stands for mode conversion.

The results in Figure 4.5 show that there is wave mode separation for the incident waves of both T(0,1) and T(0,2) after 2 metres. The reflection from the defect shows that each pulse is separated by approximately the same time intervals. The incident wave for T(0,1) interacts with defect and reflects back to the receiver as two pulses. The first pulse is T(0,1) and the second pulse is a mode conversion into T(0,2). The opposite effect occurs when the incident wave for T(0,2) interacts with the defect causing a direct T(0,2) reflection and a mode conversion into T(0,1). The four pulses that arise from the defect arrive at different time intervals due to the velocity or velocity change they experience during the time of flight. The first pulse that arrives from the defect is T(0,1), which travels at 3260m/s for the full 7m from transmitter to defect and is reflected back to the receiver. The second pulse is the mode conversion from T(0,1) into T(0,2), which travels 4.5m at 3260m/s and 2.5m at 2593m/s. The third pulse is the mode conversion from T(0,2) into T(0,1), which travels 4.5m at 2593m/s and 2.5m at 3260m/s. The final pulse that occurs from the defect is T(0,2), which travels at 2593m/s for 7m. The time arrivals for each wave mode are shown in Table 3.

Table 3. Wave mode path and time arrivals.

Wave Mode Path	Time Arrival (uS)
T(0,1) Incident	613.4
T(0,2) Incident	771.3
T(0,1) Reflection	2147.2
T(0,1) to T(0,2) Mode Conversion	2344.5
T(0,2) to T(0,1) Mode Conversion	2502.3
T(0,2) reflection	2699.6
T(0,1) Pipe End	3067.5
T(0,2) Pipe End	3856.5

The incident wave modes for T(0,1) and T(0,2) are separated at a propagation distance of 2m in Figure 4.5 by 157.9us. Both wave modes move further apart as T(0,1) travels faster than T(0,2) as they propagate towards the defect. The mode conversion that occurs from T(0,1) interacting with the defect converts into a slower T(0,2) and the opposite occurs from T(0,2) converting into T(0,1). Therefore, as the two mode converted wave modes reflect back to the receiver the time arrivals will converge back to the same difference as the two incident waves of 157.9us. The separation between the reflected signal and mode conversion from one of the incident waves is determined by the distance between the receiver and the defect. To provide the same difference in the time arrival as the incident wave modes and the mode converted signals, a separation of 2m would be sufficient i.e. the same distance between the transmitter and receiver. Therefore to provide added wave mode separation a distance of 2.5m is chosen to accommodate for the dispersive nature that T(0,2) experiences, especially the direct reflection that has a propagation path of pure T(0,2). The next step is to consider the dispersive nature of T(0,2), hence Figure 4.6 shows the relative dispersion of T(0,2) to T(0,1) for the incident wave, a virtual defect and the pipe end when considering the experimental setup in Figure 4.4. The pure T(0,2) wave mode is only considered because it is the most dispersive wave mode that exists in comparison to all four reflections that occur from the defect.

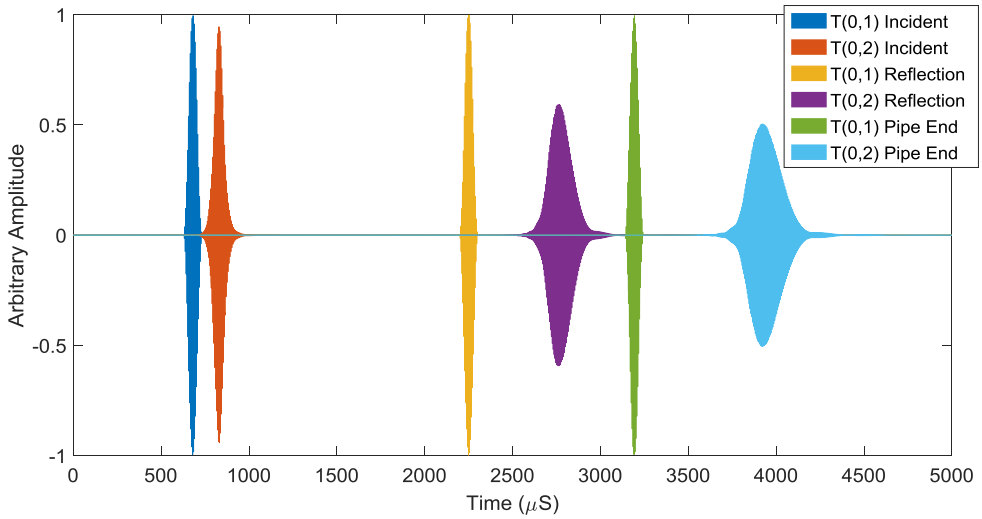

Figure 4.6. Predicted time arrivals of T(0,1) and T(0,2) including dispersion.

The results show that the T(0,2) incident wave mode has relatively the same amplitude as the incident wave mode for T(0,1). The peak to peak amplitude has decreased by a small amount (less than 0.5dB), however the pulse spreading does not interfere with the amplitude values of T(0,1) providing true peak to peak values for T(0,1), which is essential for calculating accurate reflection coefficients. The pulse spread for the second T(0,2) signal shows that the pulse does not interfere with the pipe end response from

T(0,1), which provides accurate peak to peak measurements. The results cannot show the pulse shape and signal spread for the mode converted signals because 'Disperse' can only provide the pulse shape of a particular wave mode that has propagated over an arbitrary distance. Therefore, in order to show that the experimental setup was capable of separating all the relevant signals needed to calculate the reflection coefficients a model of the experimental setup was created in ABAQUS Explicit 6.12 (ABAQUS [2012], further descriptions of FE models are presented in section 4.3). The signals are presented in Figure 4.7 shows a 190kHz 20 cycle Hann windowed pulse orientated in the torsional direction for a 50% wall loss.

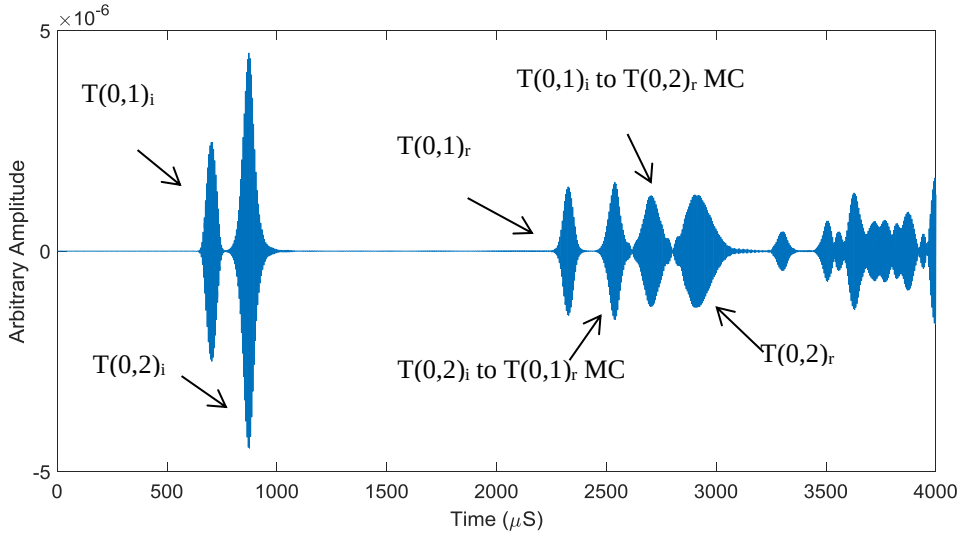

Figure 4.7. FEA signal response for a 50% depth defect using a 190kHz 20 cycle Hann windowed pulse. $T(0,n)_i$ is the incident wave and $T(0,n)_r$ is the reflection. MC is Mode Conversion.

The modelling results show that the incident wave and the signals reflected from the defect are separated sufficiently to calculate the reflection coefficients. The torsional excitation at 190kHz provides T(0,2) with more energy than T(0,1) instead of equal excitability, which is apparent in the difference in amplitudes from the incident wave modes. The four reflection coefficients calculated from the response can provide detailed ratios that can determine the size of the defect and is the basis for the work that follows.

4.3 Finite Element Modelling Setup

4.3.1 Full Pipe Model Setup

This section provides the method for creating a full pipe guided wave model that replicates the pipe and type of defects that were used in the experimental procedure conducted in section 4.2.

The first step was to create the 3D pipe model by extruding the cross section of the pipe to 6 metres (length of the pipe used in the experiments), as shown in Figure 4.8. Considering that torsional wave modes are investigated in this analysis, the pipe was created around its centre axis to ensure the pipe was symmetrically spaced around the circumferential coordinate system shown in Figure 4.8. This ensured that loading points excited the pipe model with the torsional conditions used in the experiments and received them in the same manner.

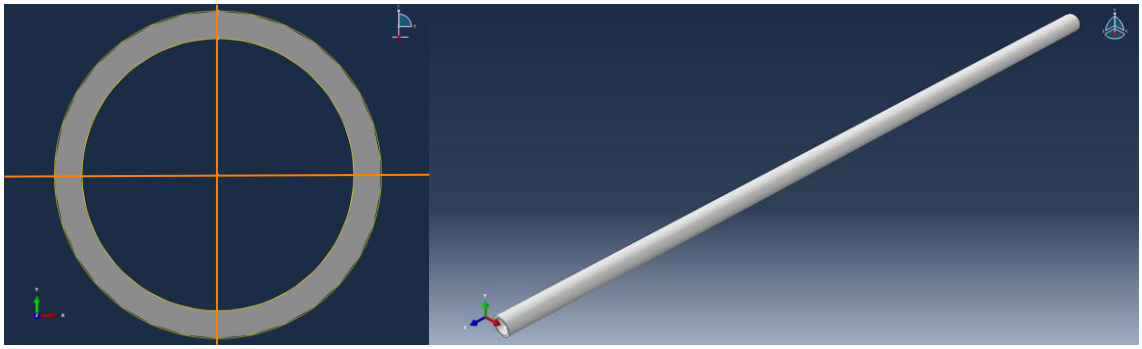

Figure 4.8. Cross-sectional area (left) and 3D representation of pipe model (right).

Steel material properties were assigned to the model (density = 7850kg/m^3, Young's Modulus = 207GPa and Poisson's Ratio = 0.3). The next step was to create partitions. These were used to provide points for loading (transmitted signal from the transducers

in the experimental setup), the receiver positions in the history output (the virtual equivalent of the vibrometry points used to receive signals experimentally) and to create different size defects from one fully meshed model shown in Figure 4.9. A set of equally spaced nodes were created for transmitting and receiving the signals.

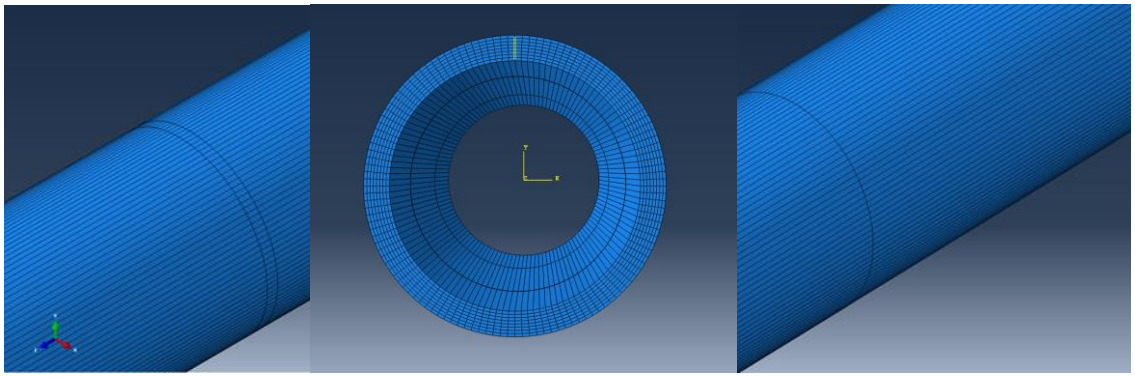

Figure 4.9. Partitions for defects (left), partitions for loading (middle) and partitions for receivers (right). A fully meshed model will contain 256 nodes around the circumference and 4000 nodes in the axial direction in one path.

To recreate the time domain signal received in the experiment two steps were needed. Step 1 was principally for the time duration of the transmitted signal and step 2 is the time duration of the signal response from the received position recorded in the history output. The time duration for the transmitted pulse (190kHz, 20 cycle pulse) is 105.4μs and the time duration is 3900μs, which provides full coverage of the pipe i.e. enough time to receive both T(0,1) and T(0,2) from the pipe end calculated in section 4.3.

The time increment t_{inc} is calculated by estimating the ratio of the smallest element length L_{ele} and the maximum bulk velocity V_{bulk} (approximately 6000m/s) using the following rule:

$$t_{inc} = \frac{L_{ele}}{V_{bulk}} \tag{4.4}$$

To determine a suitable element length enough nodes must be present to sufficiently sample the signal. The parameters that affect this length are the maximum frequency

F_{max}, minimum phase velocity V_{min} and the number of sampling points per wavelength N_{points}. The following rule was used to determine element size:

$$L_{ele} = \frac{V_{min}}{F_{max} . N_{points}} \quad \textbf{(4.5)}$$

To determine the element length, it is necessary to identify the wave mode on the dispersion curve with slowest phase velocity at the maximum frequency the model is intended to process. In this case the wave mode with the slowest phase velocity is T(0,1) at 3260m/s and the maximum frequency is 190kHz. To adequately sample the signal, 8 nodes/points per wavelength were used. Therefore, to achieve a minimum of 8 points per wavelength for this pipe, the element length was calculated to be approximately 2mm and a time increment of 0.2μs. This value was applied to the set of nodes used to receive the signal in the history output. Considering that the model was used to measure torsional/circumferential displacements the output variable U_θ is selected, which is equivalent to the y-axis in a rectangular coordinate system. Other variables are set to default, but these were removed to improve computational time. To separate the T(0,1) and T(0,2) a history output was created for the set of nodes created for the inner receive point (this technique is described in chapter 6).

In order to excite the transmitted signal, a time domain input signal of arbitrary amplitude was created. Both narrowband and broadband signals were used in the analysis and are described in sections 4.4 and 4.5 respectively. These signals were applied to the nodes used to transmit the signal using a concentrated force. Lowe *et al.* [1998], Sanderson et al. [2003] and Bartoli et al. [2005] have previously used nodes or point excitation to successfully propagate guided waves using finite element analysis; hence the same approach was used to transmit the signals. To ensure that torsional wave modes were excited a concentrated force (CF) was applied circumferentially (CF2 in a cylindrical coordinate system) with arbitrary values. Figure 4.10 shows an example for a 190kHz 20 cycle pulse indicating the circumferential loading arrows around the pipe circumference.

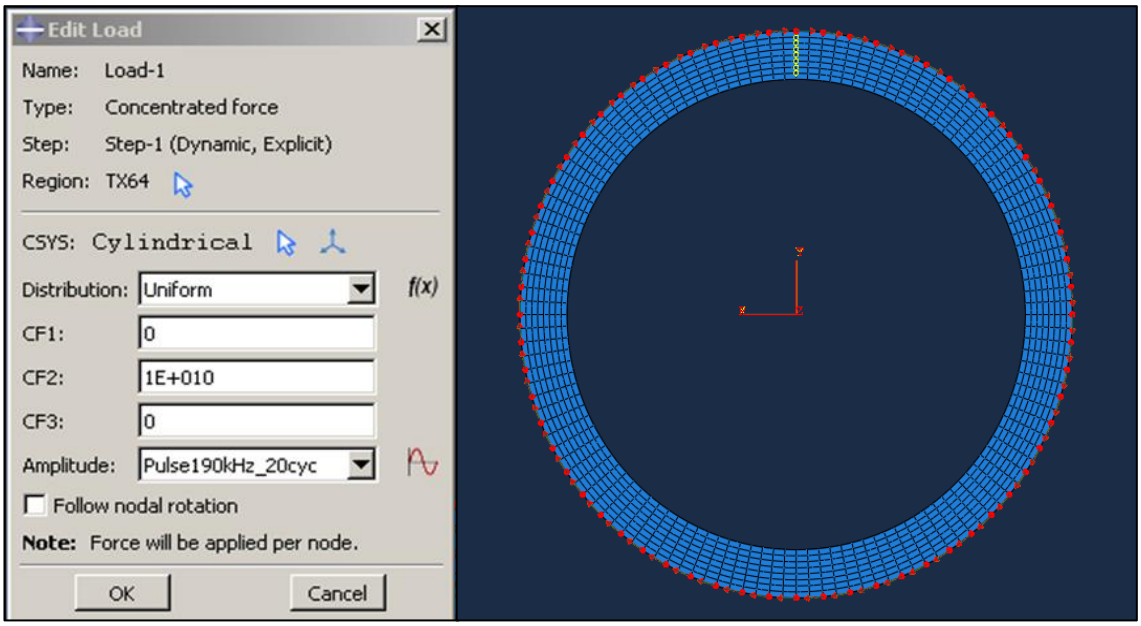

Figure 4.10. Cylindrical loading points.

A structured hexahedral mesh was used to mesh the pipe. Using tetrahedrals would double the number of elements needed in the model, which increases processing time and limits the number of defects that could be analysed. ABAQUS has an element number limit constrained by the particular package and processing capabilities available (the resources available were limited to approximately 10 million elements).

Following the selection of the mesh the next step was to assign the element type. The first step was to select between two options; ‘Standard’ and ‘Explicit’, which are related to the solution methods used. Both methods are acceptable to use, but for this problem ‘Explicit’ runs faster as there is no repetitive calculations. The processed model also takes up less disk space in comparison to standard mode. The downfall with the ‘Explicit’ solution is instability in processing for some models, which arises from poor quality meshes. However, the element sizes used in the pipe model were of equal size and the time increment used in the analysis satisfied the stability criterion. The stability limit is an important consideration when identifying the time increment value because

this may need to be reduced at higher frequencies, otherwise errors in data processing might occur. The stability limit is determined by the following inequality:

$$\Delta t \leq \frac{2}{\omega_{max}} \tag{4.6}$$

hence,

$$\Delta t \leq \frac{2}{2\pi f_{max}} \tag{4.7}$$

whereby, Δt is the time increment or step, ω_{max} is the maximum angular frequency and f_{max} is the maximum frequency. Linear elements were used in this analysis, which are suitable for guided wave propagation as the element length and displacements are relatively small, whereas quadratic elements provide greater accuracy when there are large deformations. Reduced integration was also used to decrease the time duration for processing the results and hourglass control was used to prevent the possibility of spurious deformation results, which can be caused when using reduced integration. Hourglassing is when deformation occurs but no strain is measured.

To satisfy the mesh conditions 8-node linear brick elements were used (C3D8R) with reduced integration and hourglass control. The next step was to create the defects incrementally by removing the appropriate elements around the partitioned defect region and creating the input files for each defect. Figure 4.11 shows the meshed pipe with elements removed in the defect area.

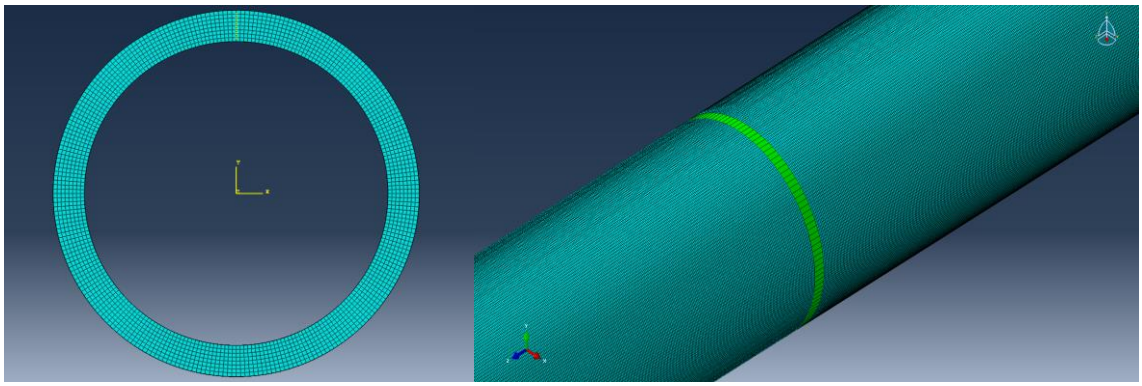

Figure 4.11. Meshed pipe model with area removed for defect analysis.

In order to receive torsional signals the coordinate system was applied to the receive node set. This was achieved by navigating in the input file and entering the receive node set name under the cylindrical coordinate transform, which was applied to the loading conditions.

The final step was to run the model and analyse the results. Before extracting the data the output file shows the area where the mesh has been removed from the analysis. These areas represent the defect that was created and this shows that the correct numbers of elements/layers have been removed, as can be seen in Figure 4.12. The results should show equal results at all received positions. Any variation in signals suggests the defect created is possibly non-axisymmetric or load points are not uniform around the circumference.

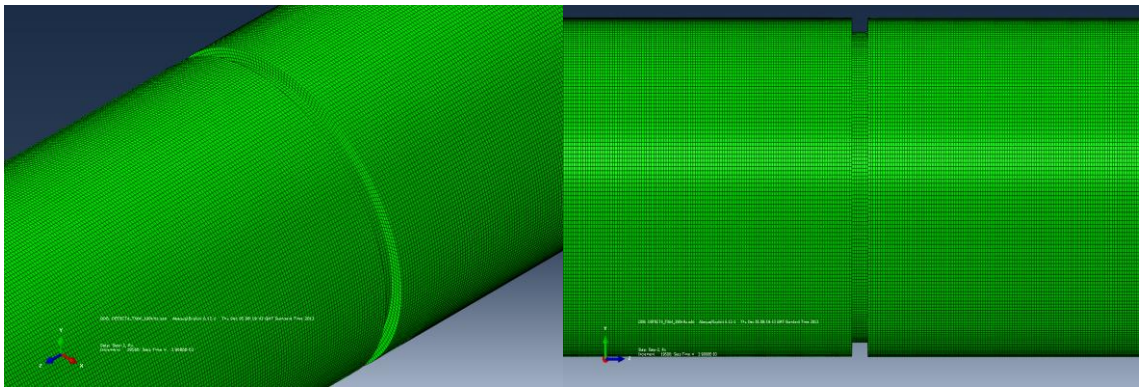

Figure 4.12. Full pipe model showing an axisymmetric defect of 50% depth. Element lengths are approximately 1.79mm.

4.3.2 Modified Pipe Segment Model Setup

The modified pipe segment model is a segment of the pipe sliced axially. The modified pipe segment has been developed to provide an alternative technique of modelling a full pipe and achieving similar results. The purpose of developing the pipe segment model was to provide a way of increasing the number of elements without reaching computational limitations. This allows more defects to be analysed and reduces processing time considering that the model has reduced the number of elements significantly in comparison to a full pipe. The number of elements in the full pipe model uses approximately the maximum capacity (over 8 million elements) of the solving system therefore with this mesh only 8 defects can be investigated. On the other hand, the pipe segment method has the potential for a much finer mesh that allows the investigation of 32 defect sizes. Much of the procedure used for creating and running the modified pipe segment is the same as the previous section describing the full 3D model, apart for the tie constraints applied to the pipe segment, which will be described in this section.

The pipe segment shown in this procedure has the same element size as the full pipe model, but results in the use of 256 times fewer elements. The segment has an angular

width of 1.4 degrees (to 1 decimal place) which is 1 element wide and 4000 elements in the axial direction, which is the same number elements in the axial direction as the full pipe model. The segment only needs one element (approximately 2mm in circumferential length) in between the sides that will be tie constrained. A tie constraint will fuse the surfaces of both sides of the pipe segment together, so that the displacement of one side of the segment is directly translated to the other side. A tie constraint constrains the Cartesian displacements on each surface face to be equal to the other, which could be a problem if the angle of the segment was increased, as the displacement from one surface to another would become more out of plane than circumferentially aligned. However, the angle of the segment is relatively small at 1.4 degrees and, therefore, the node forced in the shear direction (circumferentially in a full pipe model) will transfer the majority of the displacement in the same direction to the neighbouring node, which effectively simulates a full pipe model. Positioning the segment with respect to the axis is crucial for achieving circumferential excitation (loading) and reception (history output). Imagine slicing a segment from the pipe model 1 element in the circumferential distance, whereby the position of the segment should remain at the same distance from the axis, as shown in Figure 4.13. Otherwise, an alternative position of the cylindrical datum axis has to be determined to create the same setup if the segment was positioned elsewhere.

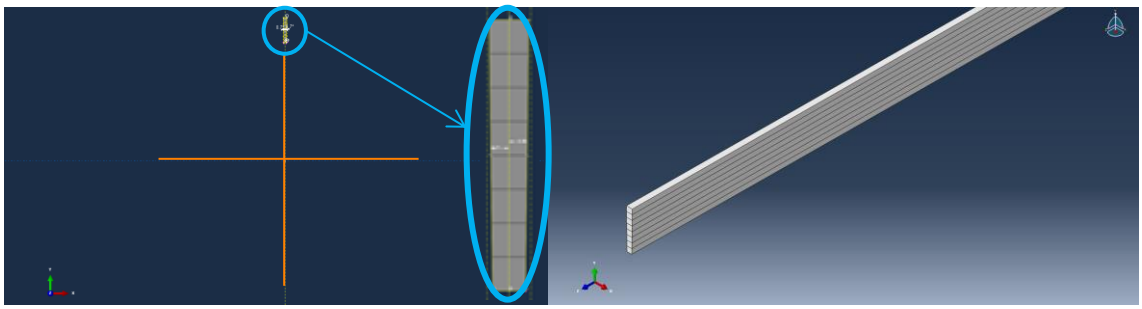

Figure 4.13. Pipe segment model showing positioning relative to axis.

Creating the appropriate partitions for the pipe segment was significantly quicker than the full pipe. The only partitions needed were to create the defect and select the receive position for the history output. The need to partition around the cross-section of the pipe to create multiple loading points has been eliminated in this model, as only one loading point is needed and one node for receiving. Figure 4.14 shows the partitions and loading point.

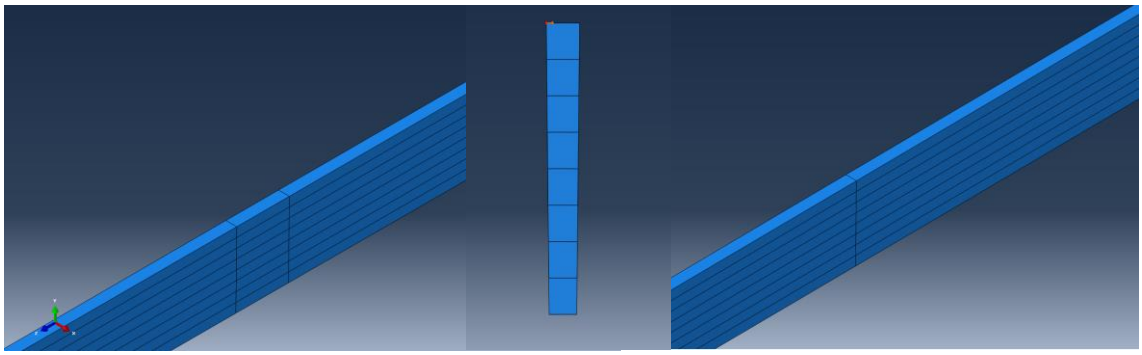

Figure 4.14. Partitions for defects (left), loading point (middle) and partition for receivers (right).

In order to produce a model that replicates a full pipe tie constraints were assigned to the sides of the pipe segment shown in Figure 4.15. All surfaces were selected apart from the region where the mesh is removed to create the defect, ensuring that all degrees of freedom were assigned to the tie constraint. The model will not run if an unmeshed region is tie constrained. Finally, the mesh was removed for the appropriate defects size shown in Figure 4.15, following the same steps used for the full pipe model.

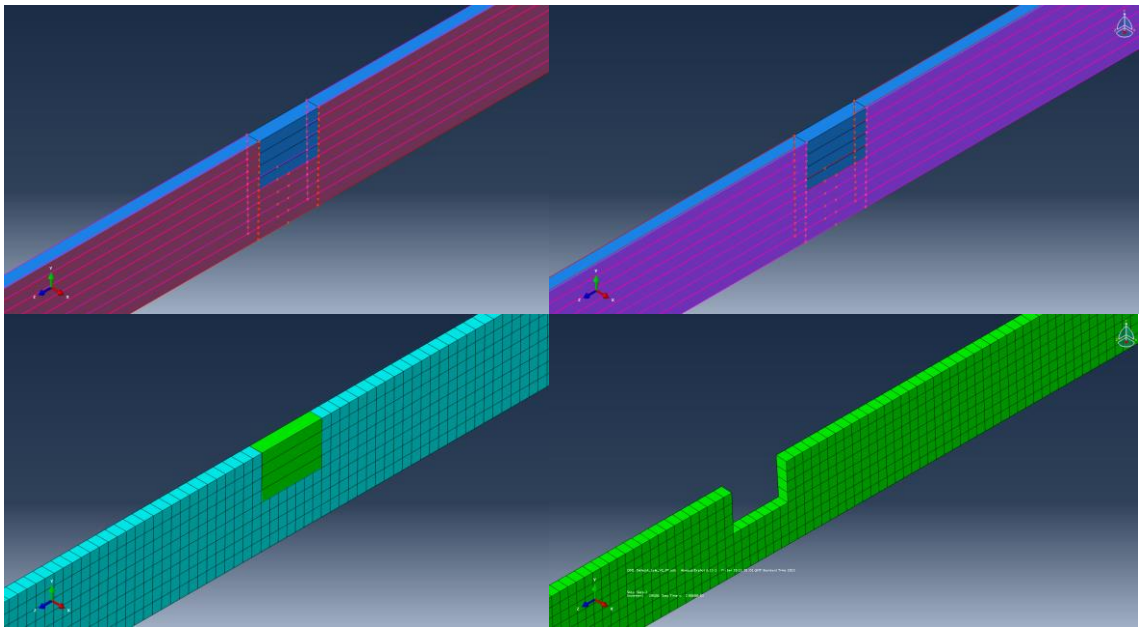

Figure 4.15. Tie constraints applied to pipe segment model (top). Pipe segment model showing an axisymmetric defect of 50% depth (bottom). Element lengths are approximately 1.79mm.

4.4 Narrowband Signals

To create the narrowband signals which are used in Teletest Focus+, a modulated Hann window is applied to a finite sinusoidal signal. A finite sinusoidal wave can be designed using the following equation:

$$y(t) = sin(2\pi f_c t) \quad \textbf{(4.8)}$$

where *fc* is the centre frequency and *t* is the time. To sample the signal and create the pulse duration use the following range of values for *t*:

$$\mathbf{0} \leq \boldsymbol{t} \leq \frac{\boldsymbol{N}}{\boldsymbol{f_c}} \tag{4.9}$$

where N is the number of cycles and t is the instantaneous time. The next step is to modulate the pulse using a Hann window using the following equation:

$$\boldsymbol{\omega(t)} = \mathbf{0.5}\left(\mathbf{1} - \boldsymbol{cos}\left(\frac{\mathbf{2\pi} \boldsymbol{f_c t}}{\boldsymbol{N}}\right)\right) \tag{4.10}$$

Therefore the Hann windowed pulse is the following:

$$\boldsymbol{x(t)} = \mathbf{0.5}\boldsymbol{sin}(\mathbf{2\pi} \boldsymbol{f_c t})\left(\mathbf{1} - \boldsymbol{cos}\left(\frac{\mathbf{2\pi} \boldsymbol{f_c t}}{\boldsymbol{N}}\right)\right) \tag{4.11}$$

Figure 4.16 shows a sine wave, the Hann windowed pulse and the Hann function used to create the narrowband signals used in the following chapters.

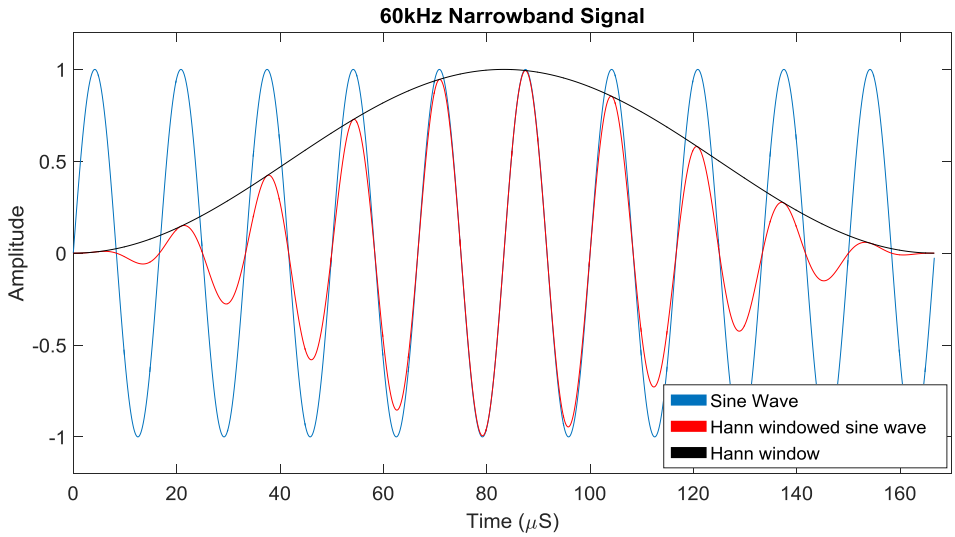

Figure 4.16. Sine wave and Hann windowed 60kHz 10 cycle signal.

An example of a signal generated for 50% defect for 200kHz is shown in Figure 4.17. The top graph shows the raw signal highlighting in blue markers the maximum amplitude values for the T(0,2) incident wave. The first step to removing T(0,2) from the signal was to normalise the T(0,2) incident wave on the outer and inner surfaces, which provides an equal incident wave on both surfaces (the difference is due to the curvature of the pipe). The displacement pattern for T(0,1) is approximately equal on the outer and inner surfaces. Normalising the T(0,2) incident wave, the displacement patterns on the outer and inner surfaces become equal and in the opposite direction. Therefore, by adding the outer and inner surfaces provides a signal of T(0,1). The same method applies to removing T(0,1); however, in this case, the outer and inner surfaces are subtracted as the displacement patterns for T(0,1) are equal and in the same direction (signal separation using FEA is described in chapter 6 section 6.2). The following equations are used to provide separate T(0,1) and T(0,2) signals from a superimposed signal:

$$\boldsymbol{T(0,1) = Signal_{Outer} + Signal_{Inner}} \quad \textbf{(4.12)}$$

$$\boldsymbol{T(0,2) = Signal_{Outer} - Signal_{Inner}} \quad \textbf{(4.13)}$$

The bottom graph highlights the reflected wave modes by overlapping the T(0,1) and T(0,2) signals. This is used to check that there is negligible interference from each wave mode at the peaks from the reflected signals. These peaks are measured by setting gates around the pulses based on their time of flight, which is calculated by the velocity or change in velocity for the mode converted signals. An algorithm was developed to automatically alter the gates with respect to frequency in order to gate and record the maximum amplitudes at the incident and reflected signals. The gates are derived from group velocity obtained from the dispersion curves, which provide a velocity and frequency relationship. The time arrival of a particular wave mode is predicted, which indicates the first gate, and the second gate is determined by the pulse width. Therefore, automatically providing the reflection coefficients for all defects and frequencies tested.

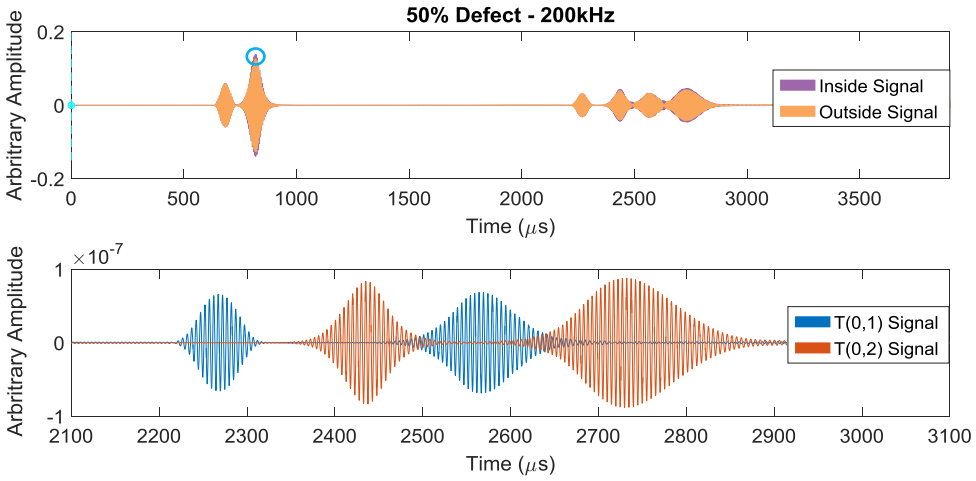

Figure 4.17. Signal response the outer and inner surface of the pipe for a 50% using a 200kHz 20 cycle Hann windowed pulse (top). Reflections from the defects showing T(0,1), T(0,2) and the mode converted signals (bottom).

4.5 Broadband Signals

A broadband signal is a signal that contains a wide frequency bandwidth. The potential benefits of using a broadband signal is the ability to gather inspection data for a range of frequencies from one inspection. However, narrowband signals are used in guided wave

inspection to prevent the excitation of unwanted wave modes and avoid multi-mode excitation. Broadband signals generally have complex signal responses because the velocities of particular wave modes are frequency dependent, which will change the pulse shape as the wave propagates. Alleyne [1992] expressed the view that broadband signals should be avoided and narrowband signals should be used to reduce dispersion. Until recently, research on guided waves has been conducted using narrowband however, Thornicroft [2015] investigated the use of broadband signals for guided wave inspection. The research was based on extracting narrowband signals from broadband signals for single fundamental axisymmetric wave modes. The same approach was used in this work to extract narrowband signal responses from medium range signals, which have multimode signal content i.e. T(0,1) and T(0,2). The purpose of exploring this technique for finite element analysis is to reduce the number of models needed for each frequency and defect size, considering that one set of data contains a wide range of frequencies. Testing a defect with a range of individual frequencies is time consuming as multiple models would need to be processed for each frequency, which requires a large amount of data. To the best of the author's knowledge the use of broadband signals for guided wave inspection in FEA has not been presented in the literature. The following sections describe the method for extracting narrowband signals from broadband signals and validation of the technique is presented in chapter 6.

To create the broadband signals used in the FEA a modulated Tukey window is applied to finite sinusoidal signal containing a range of frequencies known as a Chirp signal. A chirp signal can be designed using the following equation:

$$\boldsymbol{y(t) = sin(2\pi f_1 t + \pi k t^2)} \qquad \textbf{(4.14)}$$

where f_1 is the lower frequency of the chirp signal and k is the rate of change of frequency and is defined using the following equation where f_2 is the upper frequency:

$$k = \frac{f_2 - f_1}{t} \tag{4.15}$$

The time t is determined using the following range where N is the number of cycles and f_c is the centre which is determined by the following:

$$t = 0 \leq t \leq \frac{N}{f_c} \tag{4.16}$$

$$f_c = \frac{f_2 - f_1}{2} \tag{4.17}$$

The next stage is to window the chirp signal using a Tukey window:

$$\omega(t)_{Tukey} = \begin{cases} \frac{1}{2}\left[1 + cos\left(\pi\left(\frac{2t}{\alpha\tau} - 1\right)\right)\right] & \text{if } 0 \leq t \leq \frac{\alpha\tau}{2}, \\ 1 & \text{if } \frac{\alpha\tau}{2} \leq t \leq \tau\left(1 - \frac{\alpha}{2}\right), \\ \frac{1}{2}\left[1 + cos\left(\pi\left(\frac{2t}{\alpha\tau} + 1\right)\right)\right] & \text{if } \tau\left(1 - \frac{\alpha}{2}\right) \leq t \leq \tau. \end{cases} \tag{4.18}$$

where τ is the total time period of the chirp, which can be defined or calculated using the following equation and α is the Tukey ratio which defines the slope:

$$\tau = \frac{N}{f_c} \tag{4.19}$$

Therefore to apply the Tukey window to the chirp signal use the following equation:

$$\boldsymbol{x(t) = y(t).\omega(t)} \qquad \textbf{(4.20)}$$

Figure 4.18 shows a chirp signal from 20 to 200kHz with a pulse duration of 300µS. The chirp signal is also presented with a modulated Tukey window with a Tukey ratio of α = 0.2. A Tukey ratio of α = 0 provides a rectangular window and α = 1 provides a Hann window. In order to show the construction of the broadband signal a large frequency range was used. The signal starts at the lowest frequency 20kHz indicated by a longer wavelength and finishes with the higher frequency of 200kHz indicated by a shorter wavelength. The chirp input signal used for the medium range testing in chapter 6 has a duration of 300uS with a Tukey window (Tukey ratio 0.2) and a frequency range of 145-215kHz , as shown in Figure 4.19.

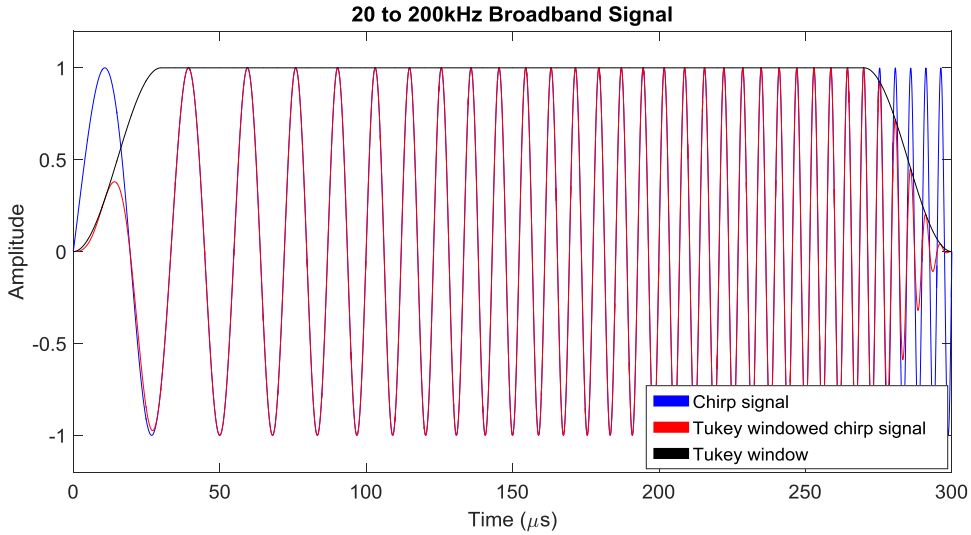

Figure 4.18. Chirp signal and a Tukey windowed chirp signal from 20-200kHz.

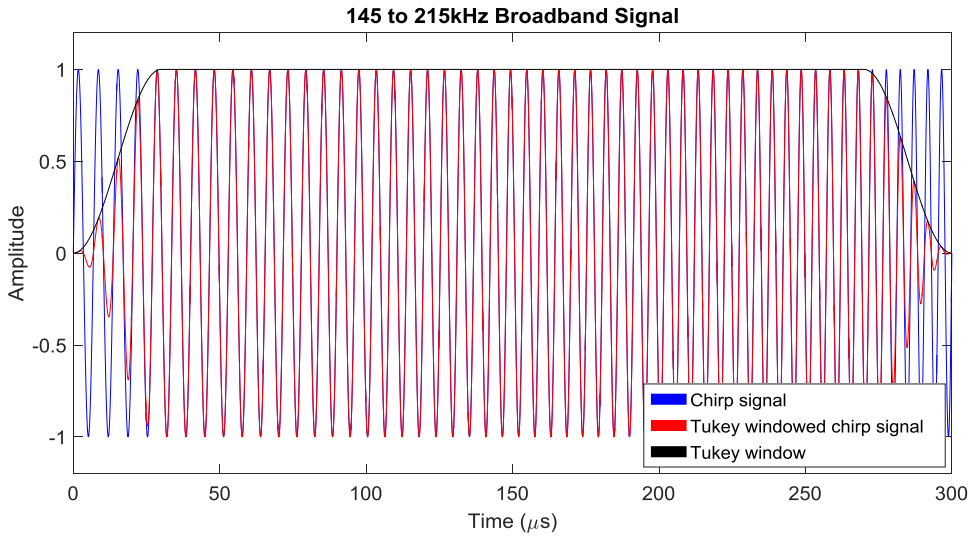

Figure 4.19. Chirp signal and a Tukey windowed chirp signal from 145-215kHz.

A model with a 50% depth defect was processed using a chirp signal and is shown in Figure 4.20. The broadband response is complex with no clear indications of the incident and reflected wave modes. The results for the same model using a narrowband signal was previously shown in Figure 4.7 (section 4.2).

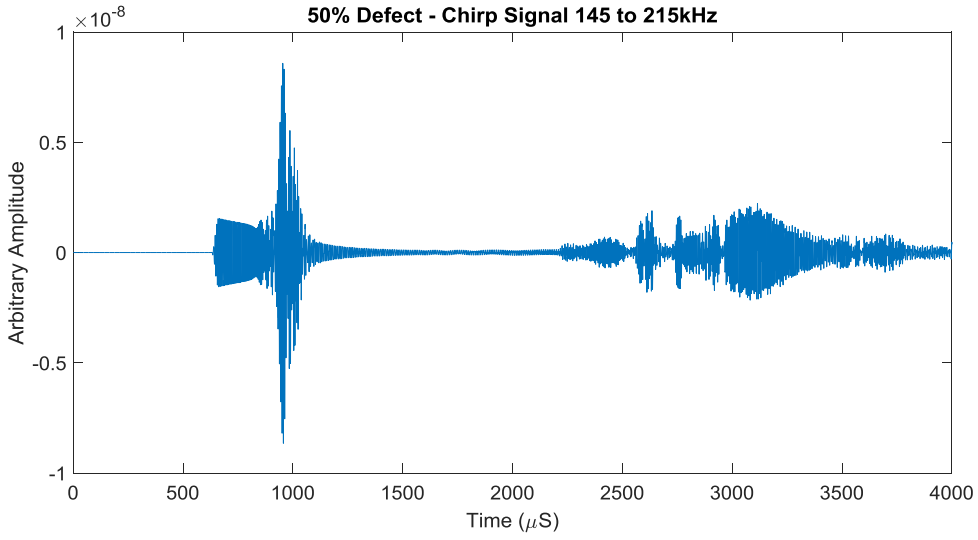

Figure 4.20. FEA signal response the outer and inner surface of the pipe for a 50% using a 145-215kHz Tukey windowed pulse.

Filtering was needed to extract the transmitted or desired output narrowband signals from the broadband signals. Thornicroft [2015] conducted experiments and developed a technique for extracting narrowband signals from broadband signals, however to the best of the author's knowledge this technique has never been applied to numerical modelling of ultrasonic guided waves. The filtering technique can be expressed by the following equations:

$$\boldsymbol{Y_{Hann,R} = X_{Hann,T} \cdot Z} \tag{4.21}$$

$$\boldsymbol{Y_{Chirp,R} = X_{Chirp,T} \cdot Z} \tag{4.22}$$

Where Y denotes the Fourier transform of the received signal and X denotes the transmitted signal. The propagation distance is denoted by Z. Therefore,

$$\boldsymbol{Y_{Hann,R} = \frac{X_{Hann,T}}{X_{Chirp,T}} \cdot Y_{Chirp,R}} \tag{4.23}$$

The filter that is applied to the received Chirp signal in order to extract a narrowband Hann signal can be expressed in the frequency domain as:

$$\boldsymbol{W = \frac{X_{Hann,T}}{X_{Chirp,T}}} \tag{4.24}$$

To present the narrowband signal in the time domain, the inverse FFT is applied. The results for the filtered results into a 200kHz Hann windowed for a 50% wall loss signal are presented in Figure 4.21. The results have negligible difference to a narrowband

200kHz response. This technique is explored in chapter 6 and is used to improve the efficiency of FEA by reducing the number of models required to analyse different frequencies against different size defects.

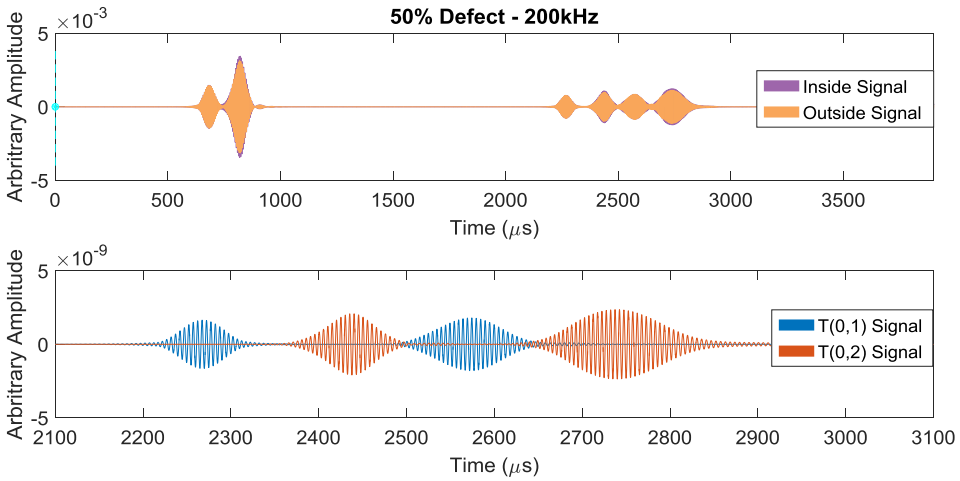

Figure 4.21. Signal response the outer and inner surface of the pipe for a 50% using a 145-215kHz Tukey windowed pulse filtered to a 200kHz Hann windowed (top). Reflections from the defects showing T(0,1), T(0,2) and the mode converted signals (bottom).

4.6 Conclusions

This chapter provides a method for conducting experimental and FE analysis for the purpose of defect sizing using medium range frequencies. The literature has shown that defect sizing for low range frequencies has been explored; however this chapter provides an alternative method using medium range frequencies.

Using medium frequencies generates higher order wave modes, which have been utilised for the purpose of defect sizing in chapter 6. Operating at medium range frequencies decreases the wavelength of a signal, which reduces dead zones (transmission period) providing the capability of inspection near to the transducer array. Another benefit of using medium frequencies is that they can be used to increase the

spatial resolution potentially increasing defect detectability. Reducing the dead zone and increasing the spatial resolution can give a technique that can be used to inspect shorter sections of pipe with higher resolution that current low range frequency cannot achieve. The method provides transmitter, receiver and defect positioning in order to separate the T(0,1) and T(0,2) responses for defect analysis.

Conducting the analysis in FEA allows multiple different size defects to be analysed, but is limited to the element size of the model. Operating at medium frequencies requires smaller sized elements in comparison to low range frequencies in order to provide adequate sampling of the waves. Therefore, a modified pipe model was created to provide a way of analysing multiple defects with small incremental size changes, without reaching the computing capacity. Defect sizes with an incremental change of less 0.5mm were investigated in chapter 6, which are extremely difficult to accurately machine into the pipe sample used in the experiments.

Conventional narrowband signals are used for guided wave testing, which is the adopted approach used in the Teletest Focus^{+} system. However, considering that there is a range of frequencies that require investigation, using narrowband pulses for each defect size can be infeasibly time consuming. Therefore, using broadband signals and a filtering processing technique described in this chapter, multiple frequencies can be investigated from one particular finite element model. This significantly reduces the processing time and the amount of data stored for each particular defect being analysed. This technique enables the measurements to be taken for all wave modes present for a range of frequencies in order to provide a defect sizing technique presented in chapter 6. To the best of the author's knowledge using T(0,2) for the purpose of defect sizing has not been presented in the literature.

The method described in this chapter is used experimentally and for finite element analysis in both chapter 5 and chapter 6 respectively. Chapter 5 uses this method of separating wave modes to investigate the performance of the existing transducer array

used in guided wave testing against the developed high density transducer developed for the purpose of medium range frequency inspection. Chapter 6 uses the method for developing a defect sizing technique based on the T(0,2) wave mode.

5 EXPERIMENTAL FEASIBILITY STUDY USING HIGHER ORDER T(0,2) WAVE MODES FOR PIPE INSPECTION

5.1 Introduction

This chapter gives consideration to the approach generally taken to design a piezoelectric transducer array for low frequencies (<100kHz), used for oil and gas pipeline inspection, and evaluates the feasibility of adapting these methods to medium range frequencies. Current commercial systems (described in chapter 3 section 3.3) use low frequency (typically <100kHz) for guided wave testing that can inspect a pipeline up to 100m from a single location. Many new applications have been identified within the industry that require shorter testing ranges with higher ultrasonic sensitivity such as sprinkler pipe inspection. Other applications include identifying and quantifying defect sizes not feasible with current commercial systems, which could potentially be achieved by implementing medium range frequency inspection.

During the literature review it was seen that little experimental work has been carried out at medium range frequencies (between the cut-off frequencies for T(0,2) and T(0,3)) and it was not clear if measuring the amplitude of T(0,1) and T(0,2) was experimentally feasible with the common approaches used in the literature at the typical, low ultrasonic frequency range (below the T(0,2) cut-off frequency). To investigate the feasibility of developing a transducer array design capable of performing under medium frequencies, an investigation was conducted on the current process of designing a low range frequency transducer array. The challenges that occur at medium range frequencies is the capability to supress the increased number of flexural wave modes that exist at medium range frequencies, in order to provide pure axisymmetric T(0,1) and T(0,2) wave modes. Using higher numbers of transducers in densely packed arrays, wave mode control can be achieved that allows for axisymmetric testing with sufficiently low interference from flexural modes. In order to investigate this hypothesis this chapter will address challenges in producing high density arrays, such as sourcing the development of a suitable transducer equivalent to the commonly used low frequency systems and investigating the current array design used in the Teletest Focus+ system.

The areas investigated in this chapter include:

- Dispersion curves
- Wave modes generated
- Types of piezoelectric transducers
- Transducers array design

Investigating dispersion curves provides details on the number of wave modes that exist at the operating frequency, which determines the number of transducers needed to supress flexural wave modes. Considering that the current piezoelectric transducers are dimensionally not suitable for a high density array, alternative transducers were needed to develop the array. During the design stages for the high density array the transducer spacing used in the existing transducer array was investigated to further supress flexural wave mode content and improve the design.

This chapter analyses the methods for designing the current transducer array for guided wave testing of pipes and investigates the feasibility of developing these procedures to produce a new transducer array that can be used for medium range frequency inspection.

5.2 Methods Used For Existing Transducer Array Design

In order to design a transducer array the desired wave mode or wave modes must be determined first. Current commercial systems (described in chapter 3 section 3.3) generally use axisymmetric wave modes as their desired transmission output to cover full circumferential coverage of the pipe. For example, to transmit the fundamental axisymmetric torsional wave mode T(0,1) for the pipe used in this analysis (6 inch Schedule 120), the Teletest Focus+ system uses 24 shear transducers which are positioned in a ring to shear around the circumference of the pipe and are all excited in phase. This is a sufficient number of transducers for low range frequency testing as there are more transducers than the highest order flexural wave modes below 100kHz. The following describes the number of transducers in relation to highest flexural wave mode. Figure 5.1 shows the dispersion curves for T(0,1) and the family of flexural wave modes up to F(18,2) as well as T(0,2) for a 6 inch Schedule 120 using 'Disperse' software (Pavlakovic [1997]).

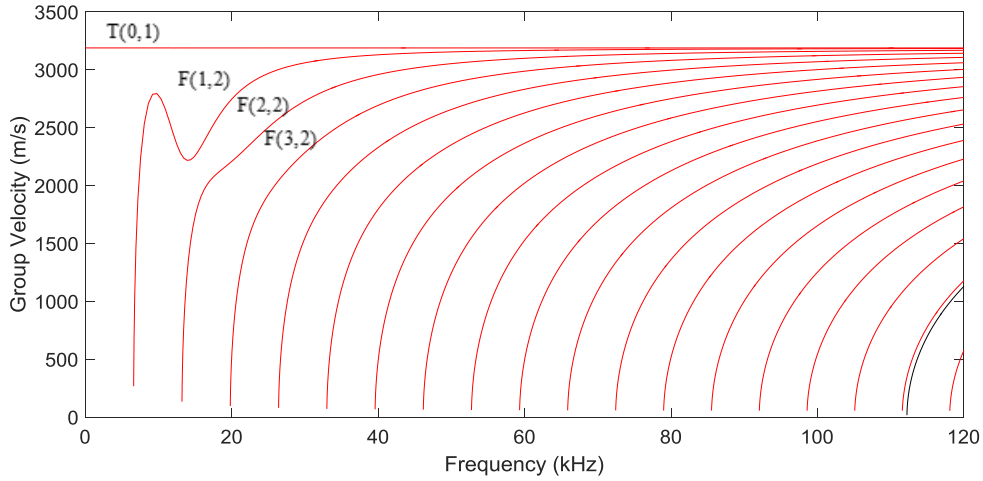

Figure 5.1. Dispersion curve showing group velocity against frequency for the T(0,1) family wave modes (red), starting from T(0,1) followed by F(1,2) to F(18,2) sequentially and T(0,2) (black).

Each flexural wave mode has a sinusoidal variation circumferentially around the pipe. The number of cycles depends on the order of wave mode i.e. F(1,n) and F(2,n) have one and two sinusoidal cycles per circumference respectively. The minimum number of transducers needed to cancel a flexural mode from a signal is one more than the highest wave mode that can exist for the frequency range excited. This current method is sufficient for analysing axisymmetric wave modes, as a summation of each signal received at the transducers would enhance these wave modes and eliminate flexural wave modes. Figure 5.2 shows two examples for F(3,n) and F(7,n). The sinusoidal line represents the circumferential pattern and the vertical lines represent equally spaced transducers around the circumference, whereby the dots represent the interception points with the flexural modes. The axisymmetric signal is produced by summing the signals from all the transducers and it can be seen that when the values of all the points in each figure are summed, they equate to zero for each flexural mode (when the number of points is higher than the order of the flexural). This shows that having one more equally spaced transducer can suppress the flexural modes at any phase as the addition of the interception points will always equal zero.

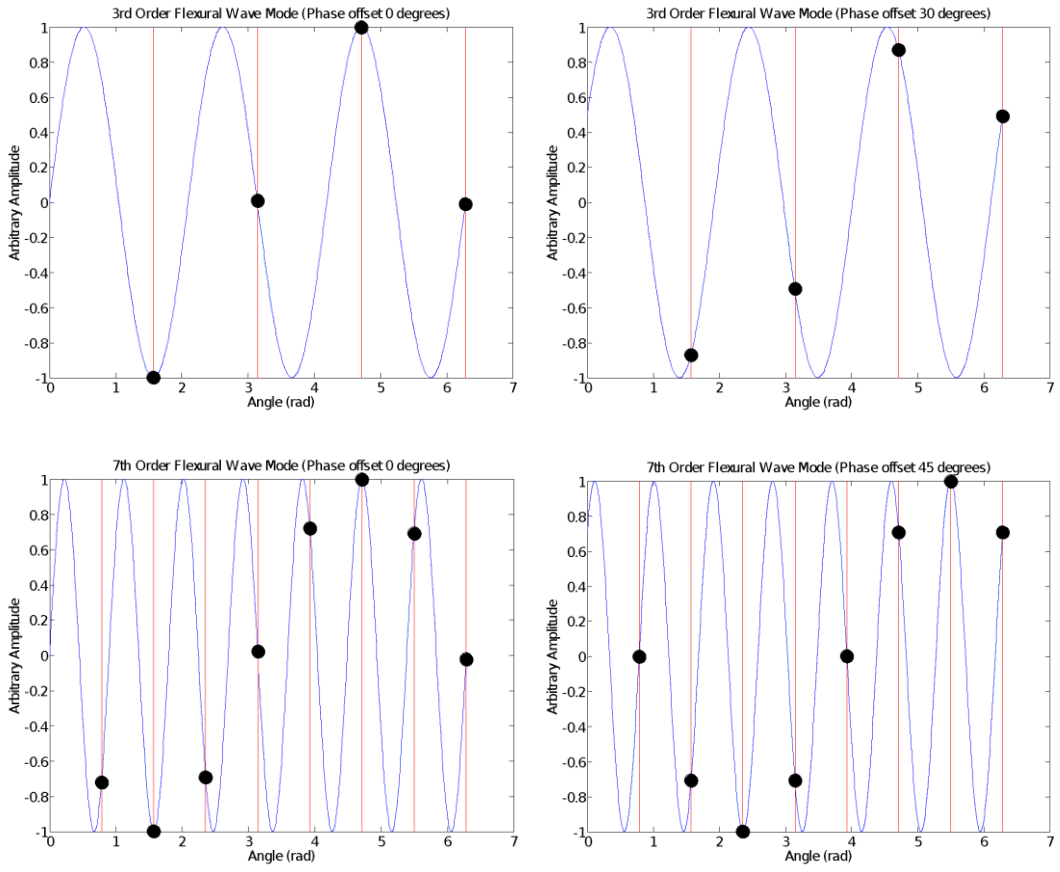

Figure 5.2. Sampling of a third and seventh order wave mode.

This allows for the transmission of pure axisymmetric modes, but the problem with this approach is that analysing the flexural wave mode content would be inaccurate as the signals are under sampled. Considering, that the objective is to improve wave mode control the number of transducers in the array must be increased to sample sufficiently, which must be greater than the Nyquist frequency to identify the wave mode content accurately and prevent aliasing.

The current Teletest Focus+ system used for the experiments conducted in this chapter can be configured to independently transmit and receive on 24 transducers. Considering that the sampling must be greater than the Nyquist frequency this setup is only able to sufficiently sample up to F(11,n). Therefore, by analysing the wave mode control based on the current system alone is an inaccurate technique because higher order flexural wave modes exist at medium range frequencies (>100kHz). To test the wave mode control a Polytec PSV-400-3D-M Scanning Laser Vibrometer (Polytec [2009]) was used to receive the transmitted signal shown in Figure 5.3. The vibrometer measures the transmitted signal without coupling and the signals are based solely on the transmitting capabilities because in order to develop an array the transmitted signal must be pure before the reception capabilities of the transducers are investigated. The vibrometer also provides the enhanced ability to receive a greater number of reception positions around the circumference.

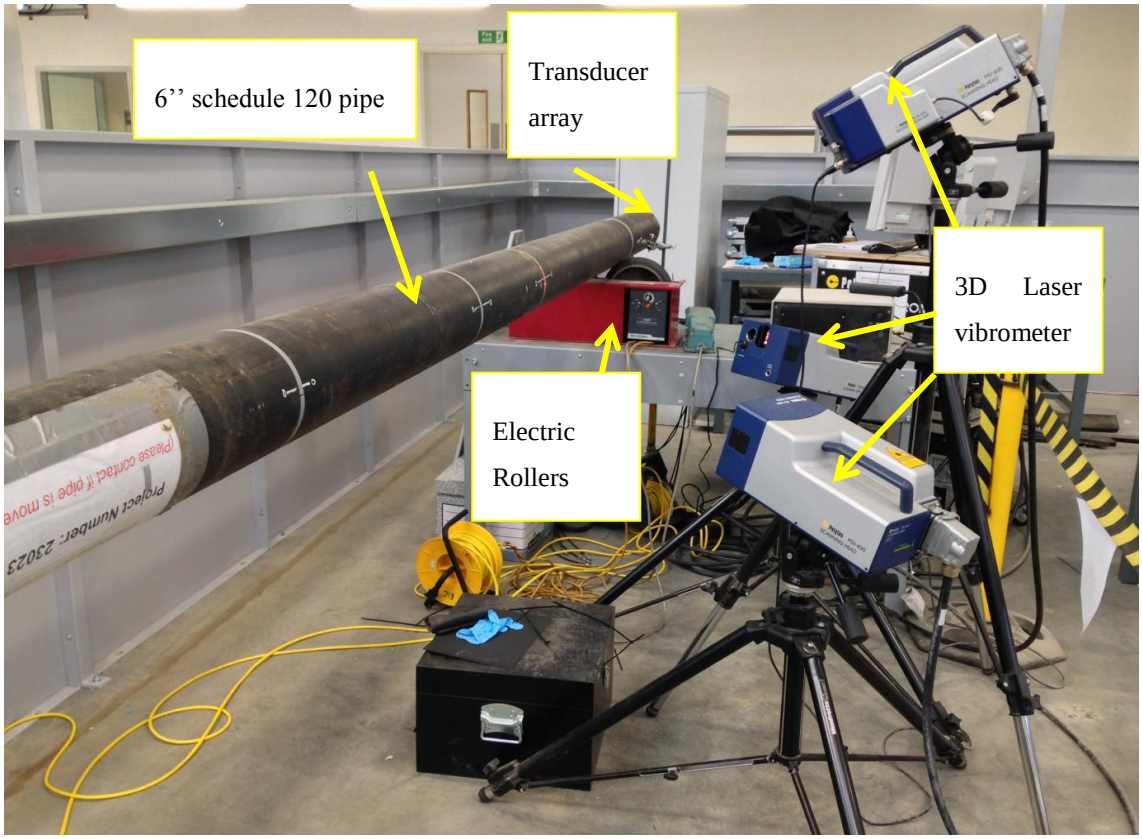

Figure 5.3. Experimental setup showing a Polytec PSV-400-3D-M Scanning Laser Vibrometer positioned on a 6 inch schedule 120 pipe.

5.3 Results for Existing Transducer Array

The existing transducer array consists of 24 transducers positioned in a ring array. Figure 5.4 shows the experiment conducted using the setup created in chapter 4.

Figure 5.4. Existing transducer array coupled to a 6 inch schedule 120 pipe showing the gap in the transducer array.

The transducers are positioned on the pipe end, a mounting collar is inflated and used to provide coupling to the pipe. The laser vibrometer was used to record the transmitted signal from the array in the torsional direction. The pipe was rotated and 118 equal positions were recorded with an equal increment spacing of 4.5mm. Reducing the next number of equally spaced increments that can be measured to 0.5mm accuracy (minimum value on measuring tape) to 59 (9mm spacing) could cause under sampling for higher order wave modes, which is discussed in section 5.4. Using a high amount of reception points improves the sampling of the signals and provides further accuracy to the amplitudes of the flexural wave mode content. Figure 5.5 shows the results for a typical low range frequency experiment at 60 kHz.

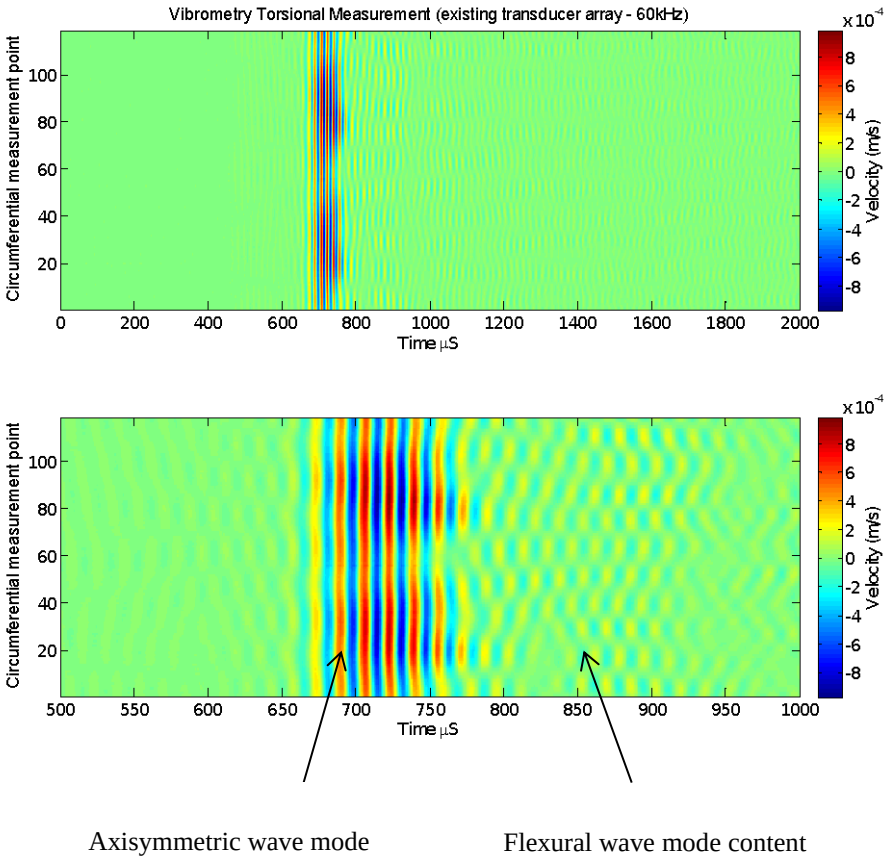

Figure 5.5. Laser vibrometer results showing surface velocity against time for 118 circumferential positions using a 20 cycle Hann windowed pulse at 60kHz for the existing transducer array.

The transducer array shows interference from flexural wave modes, which is unexpected considering the transducer array is designed to propagate T(0,1) and the signal response is not completely axisymmetric around the circumference. This is possibly due to imbalance of the outputs of each transducer in the array caused by coupling variation or the uneven distribution of transducers around the circumference due to the gap in the mounting mechanism. The Teletest Focus+ system setup does not allow each transducer to be accessed individually and therefore normalisation cannot be applied to each transducer to balance the power outputs of the transducers. Therefore, variation in the transducer outputs can cause the generation of flexural wave modes. This may be acceptable for inspection at low frequencies, but is not be suitable for a laboratory study where mode purity is of high importance.

The other concern is the gap in the transducer array caused by the mounting mechanism shown in Figure 5.4. The extent of this gap has been evaluated through an FEA analysis (ABAQUS Explicit 6.12). This shows 24 equally spaced transducers (top left of Figure 5.6) and 24 transducers with the gap that is present in the array (top right of Figure 5.6), both arrays consisting of perfectly calibrated (uniform) simulated transducers. The field output shows a pure, uniform T(0,1) for the equally spaced transducer array (middle left of Figure 5.6), and T(0,1) with a contamination of flexural wave modes from the gap in the transducer array (middle right of Figure 5.6). The results for the equally space array (bottom left of Figure 5.6) and the array with a gap (bottom right of Figure 5.6) are presented as two A-scans showing that the existing array can generate flexural wave modes and produce coherent noise in the signal. This shows that the wave mode purity of the developed array can be improved if the spacing between the transducers is equal although access to each individual transducer for normalisation cannot be achieved with the current inspection system.

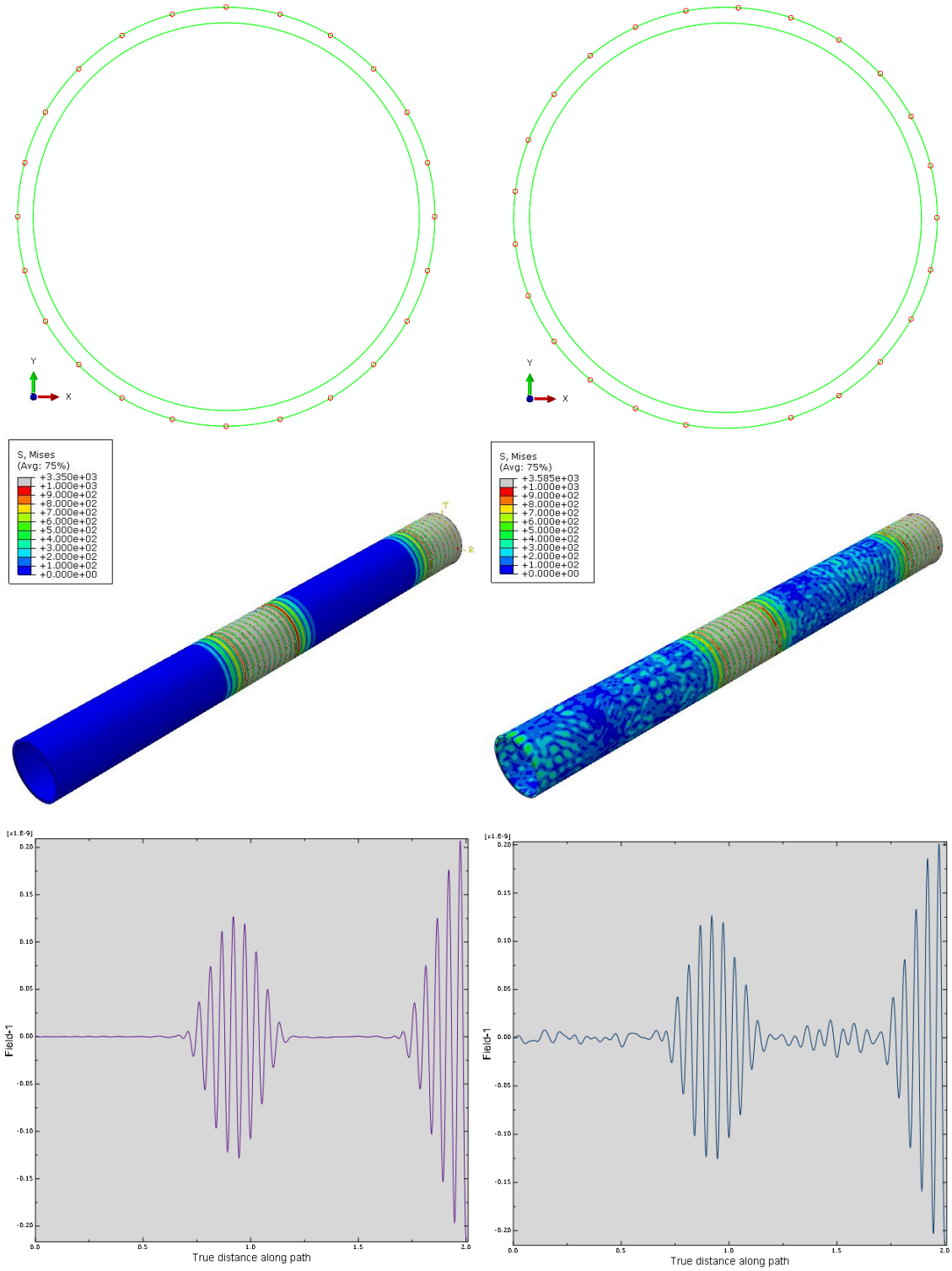

Figure 5.6. 24 equally spaced transducers and 24 unevenly spaced transducers representing the gap in the existing array (top). Visualization of wave mode content for both conditions (middle). Signal response for both conditions (bottom).

According to the analysis conducted in chapter 4 section 4.1, a suitable maximum frequency for a 6 inch schedule 120 pipe is 190kHz, which is the least dispersive frequency within the range determined. Therefore, using the existing array the experiment was then repeated at 190kHz and shown in Figure 5.7.

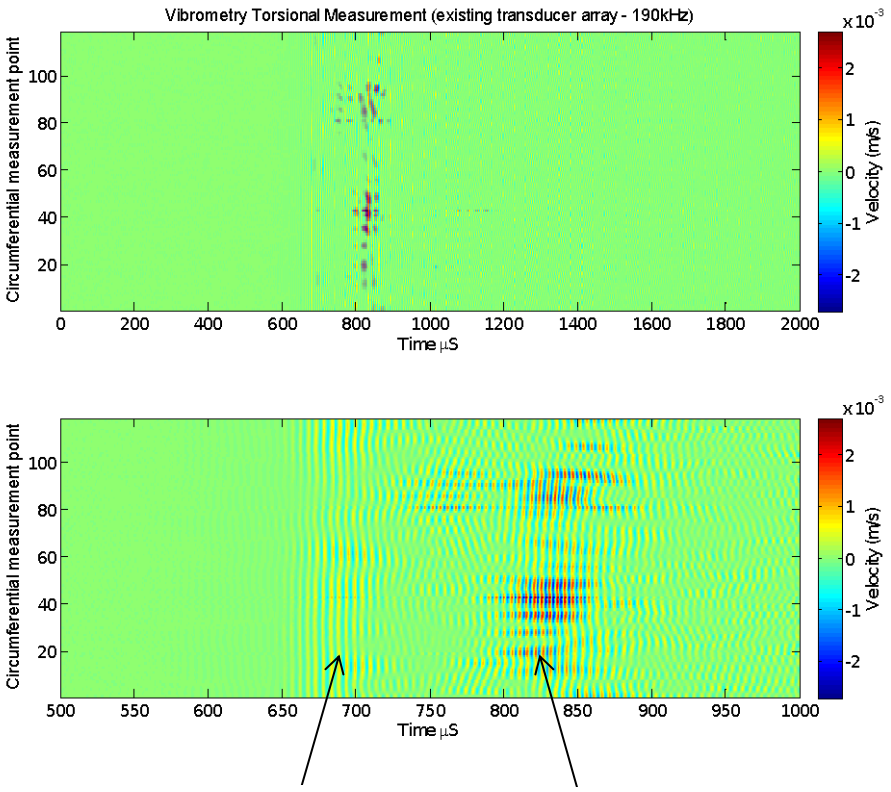

Figure 5.7. Laser vibrometer results showing surface velocity against time for 118 circumferential positions using a 20 cycle Hann windowed pulse at 190kHz for the existing transducer array.

Operating at 190kHz using the existing transducer array introduces the second order torsional wave mode T(0,2), which occurs after T(0,1). Many flexural wave modes also exist in this frequency range and make the signal very complex.

In order to investigate the wave mode content further signal processing is needed to identify the wave modes that exist and their relative excitability. This is achieved by conducting a spatial Fourier transform for each time sample. Generally a Fourier

transform is used to convert a time-domain signal into a series of amplitude and phase value pairs for a series of frequencies (based on the sinusoidal variations each frequency contributes to the signal). For a spatial Fourier transform the time domain signal is substituted for a spatial domain, which in this case is the circumference of the pipe measured by the laser vibrometer. At each time sample a Fourier transform is performed on the amplitude measured against the circumferential position, which provides the amplitude and spatial frequency relationship around the circumference, for example the amplitude response of 1 sinusoidal variation around the circumference corresponds to an order 1 wave mode. This is performed at each time interval to give amplitude and time responses for each wave mode, hence providing a decomposition of the signal with respect to wave mode number. Lowe *et al.* [1998] previously used this technique to separate L(0,2), F(1,3) and F(2,3) wave modes.

Figure 5.8 and Figure 5.9 show the surface velocity magnitude against time for each order wave mode for 60kHz and 190kHz respectively. The results at 60kHz show that there is a high amplitude response for T(0,1), which is expected as the existing transducer array has been designed to generate an axisymmetric T(0,1) wave mode. Although the existing transducer array generates mainly T(0,1) there are also some higher order flexural wave modes generated, with the second order having the highest amplitude. The difference between the amplitude of T(0,1) and F(2,2) is 16.8 decibels (dB), which is used as a baseline to compare to the results from the high density array developed in section 5.5. The results for 190kHz show that T(0,1) and T(0,2) are both excited at this frequency and that T(0,2) has the highest amplitude. This is also shown in the FEA results (Figure 4.7 section 4.3). Other results show that flexural wave modes are highly excitable in comparison to the results recorded at 60kHz. These signals can cause a greater interference with defect responses in comparison to 60kHz. Therefore, false defects can be shown in a signal by constructive interference or become undetectable by destructive interference.

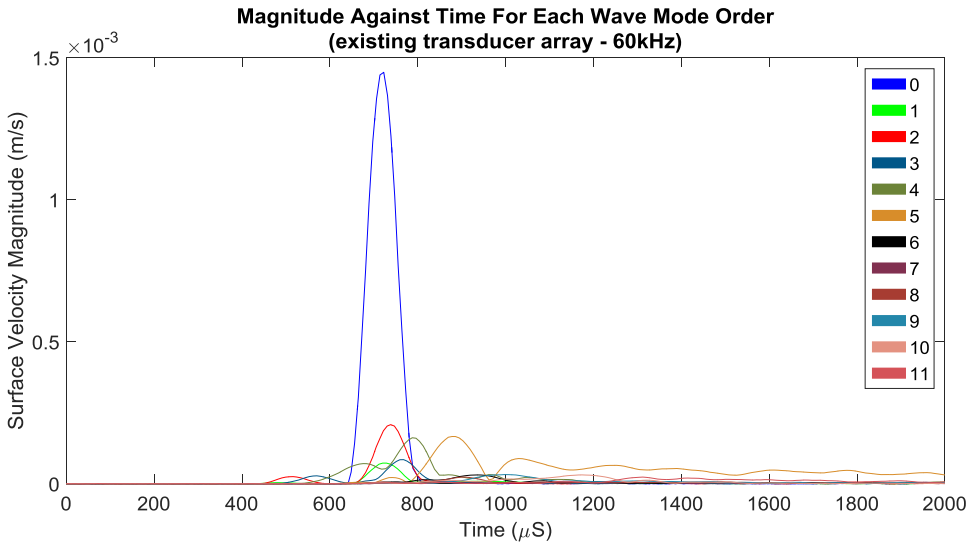

Figure 5.8. Wave mode content of the signals from the laser vibrometer results at 60kHz for the existing transducer array. Order of wave modes are indicated by numbers in the legend.

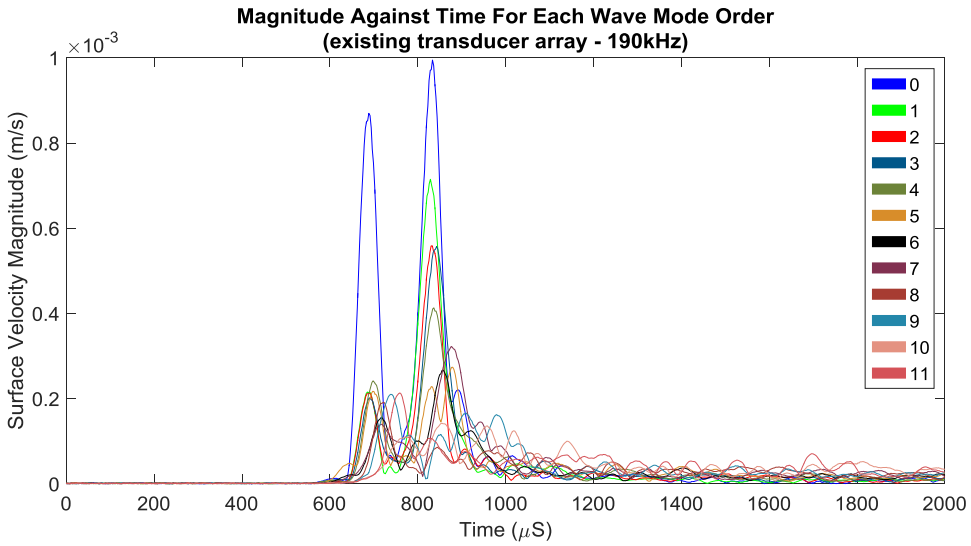

Figure 5.9. Wave mode content of the signals from the laser vibrometer results at 190kHz for the existing transducer array. Order of wave modes are indicated by numbers in the legend.

The tests have shown that the current array is not suitable for medium range frequencies, as predicted from the dispersion curves shown in Figure 5.1. Considering the design is not currently suitable for medium range inspection and there are features within the

current transducer array design that can be improved for low frequency testing, developments to the design are investigated in section 5.4.

5.4 Transducer and Array Investigation

In order to develop an improved array design the number of transducers needed to be calculated in order to satisfy the Nyquist frequency for the highest wave mode that exists at 190kHz. According to the dispersion curve Figure 5.1 the highest flexural mode that the 'Disperse' software was able to plot is F(18,n), which cuts of significantly below the medium operational frequency of 190kHz. Therefore to identify the highest flexural wave mode that exists at 190kHz an extrapolation for the cut-off frequencies can be calculated using the linear equation shown in Figure 5.10. This shows that the highest order in the T(0,1) family of flexural wave modes that exists is F(31,2) for 209kHz, which is the main lobe maximum frequency bandwidth for 190kHz, calculated using the following equation:

$$\boldsymbol{f_R = f_c \pm \frac{(2+k)f_c}{n_c}} \qquad \textbf{(5.1)}$$

Therefore in order to satisfy the Nyquist frequency 64 transducers are needed to sample every possible wave mode that can be theoretically excited.

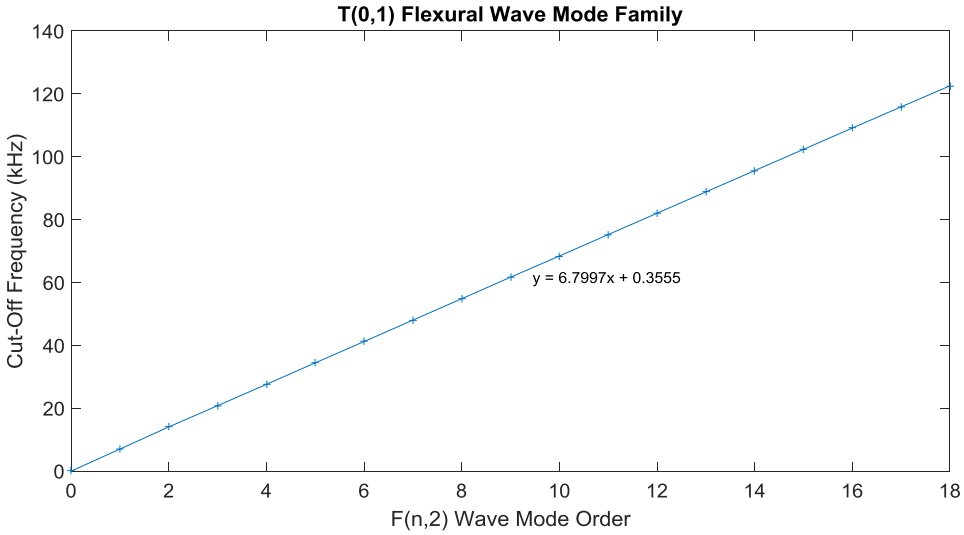

Figure 5.10. Cut-off frequency against wave mode order for the T(0,1) family of flexural wave modes up to F(18,2).

This posed a difficult challenge as the current transducer are 13mm long in the shear direction and the maximum number of transducers that can be physically attached to the 6" diameter pipe is 40. Therefore in order for the array to accommodate 64 transducers the design was changed and new piezoelectric elements were produced in which the polarisation of the transducer was rotated 90 degrees in-plane to the element to allow it to shear across the width. Figure 5.11 shows the current transducer used whereby the proposed alternative design is a piezoelectric element that shears across the width. The transversely polarised array can accommodate 64 transducers around the circumference of the pipe, eliminating the gap in the transducer array and providing enough sampling around the circumference for medium range frequency testing.

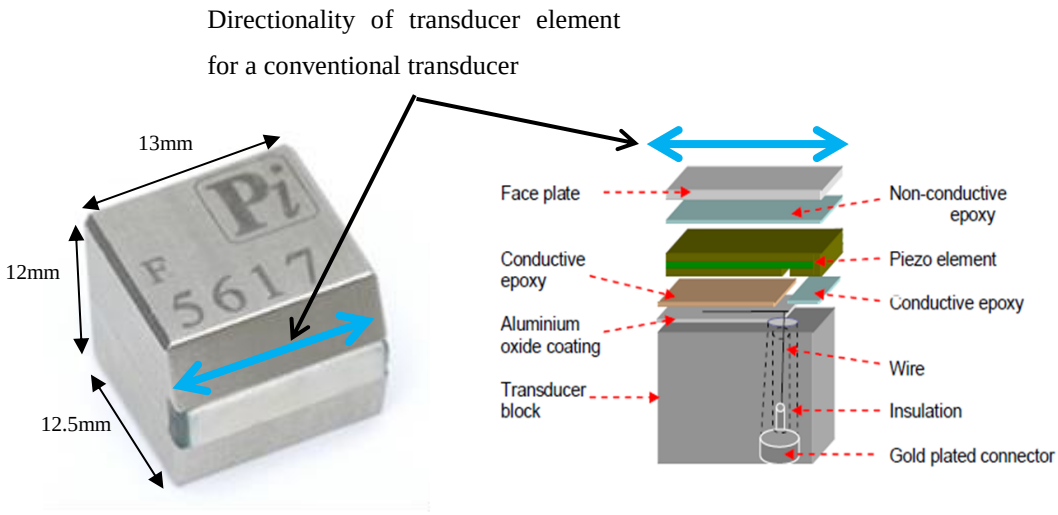

Figure 5.11. Teletest®Focus^{+} transducer.

Before using the transversely polarised transducers as an appropriate alternative, a preliminary test was conducted to compare the transmission responses of both transducers. The current transducers have a backing mass to dampen resonances whereas the alternative design is a piezoelectric element without the backing mass. To test both transducers equally they were attached to the pipe using Araldite epoxy resin. Figure 5.12 shows a comparison of the response for both transducers at 60kHz.

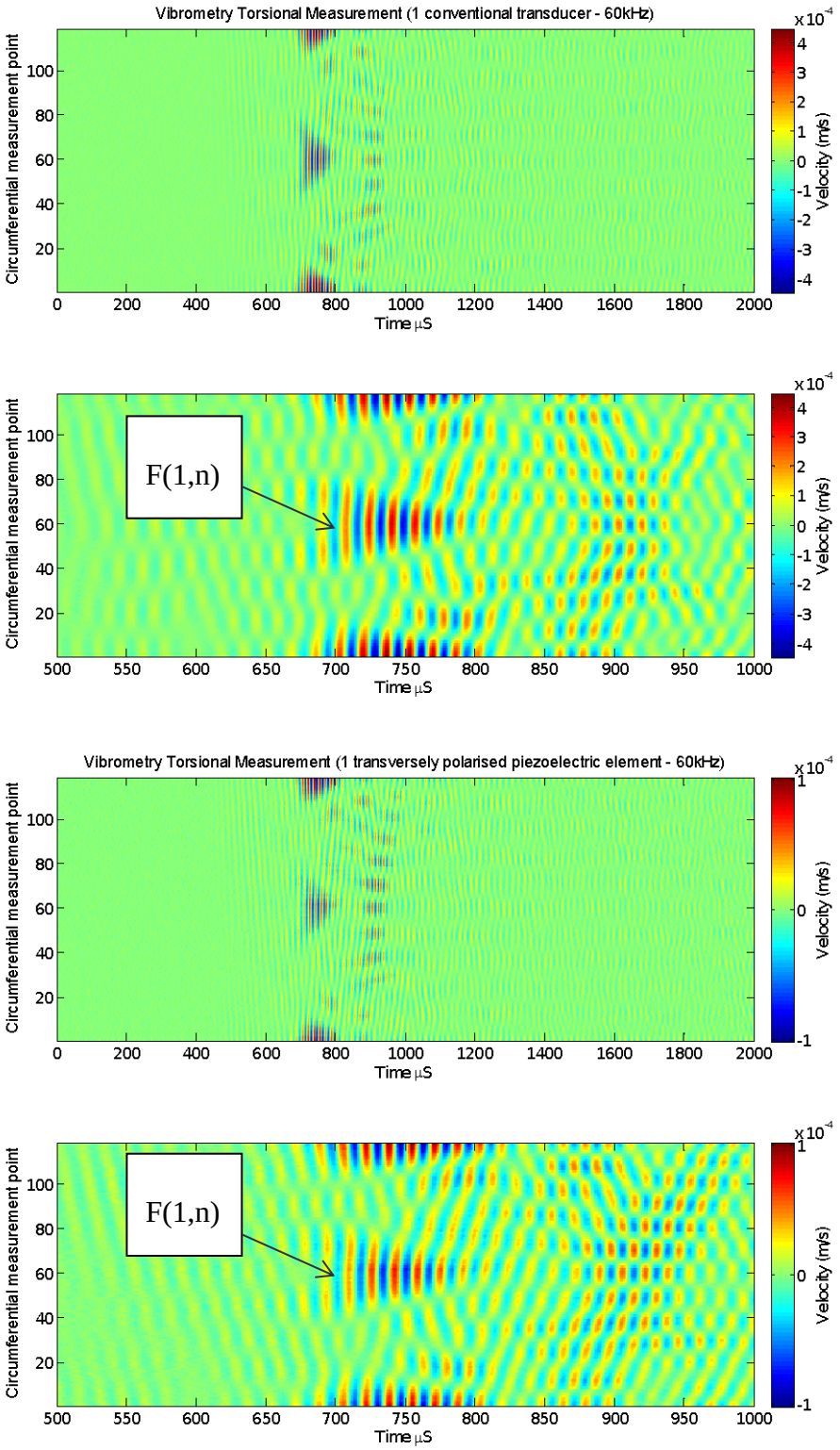

Figure 5.12. Laser vibrometer results showing surface velocity against time for 118 circumferential positions using a 20 cycle Hann windowed pulse at 60kHz for the 1 Teletest transducer (top) and 1 laterally polarised transducer (bottom).

The results show that both transducers generate very similar excitation conditions. Unlike the predominantly axisymmetric response for the existing transducer array shown in Figure 5.5, transmitting with one transducer can generate all wave modes. Catton [2009] researched the excitability of wave modes with respect to part circumferential excitation and showed that all wave modes can be excited using one transducer. The same tests were also conducted at 190kHz, with the results shown in Figure 5.13.

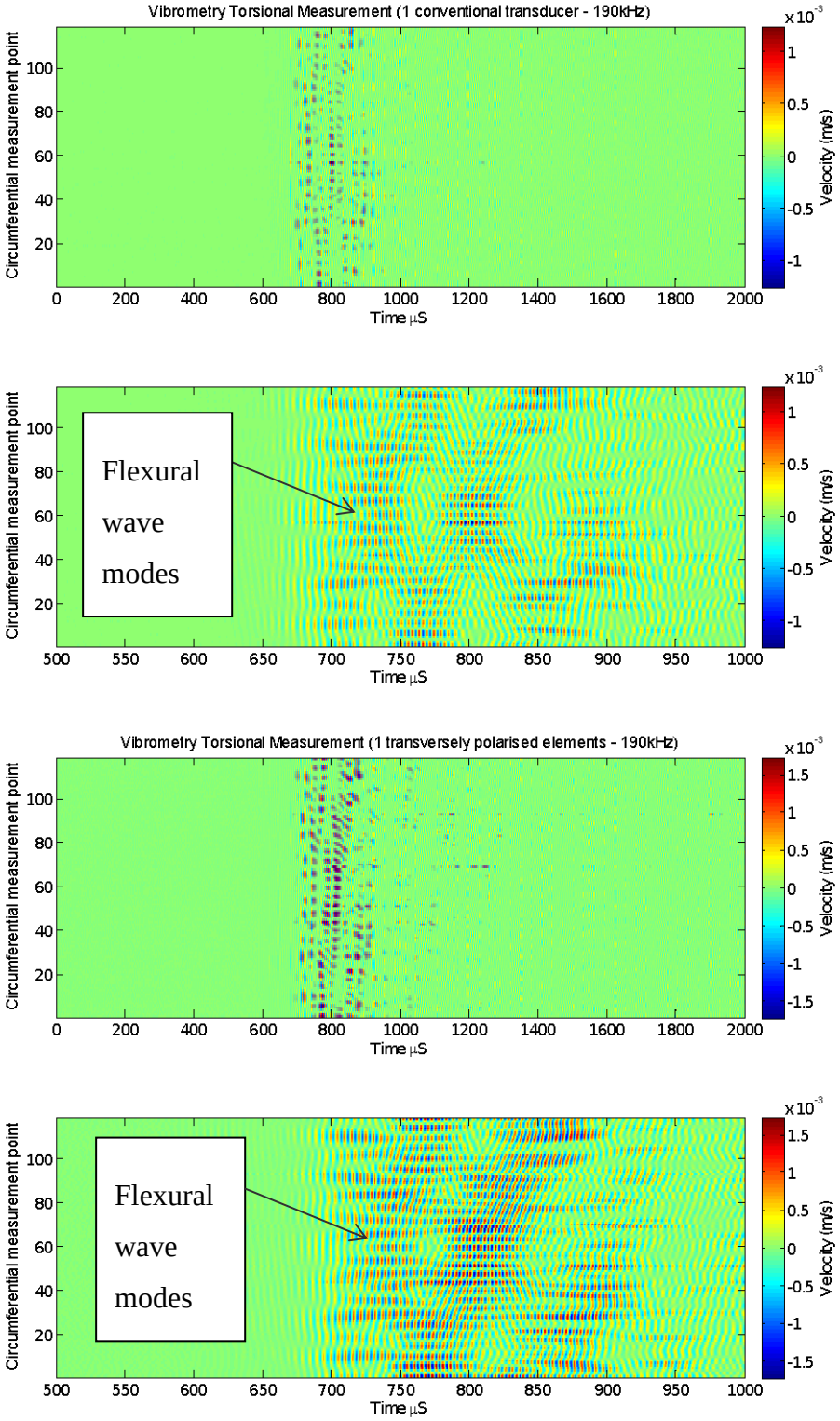

Figure 5.13. Laser vibrometer results showing surface velocity against time for 118 circumferential positions using a 20 cycle Hann windowed pulse at 190kHz for the 1 Teletest transducer (top) and 1 laterally polarised transducer (bottom).

The wave mode response at 190kHz is a lot more complex in comparison to 60kHz due to the generation of more flexural wave modes. The performance of both transducers could not adequately be compared at this frequency using this technique because of the superposition of many wave modes.

The next stage was to separate the wave modes to identify any significant differences in the signal responses that might indicate the laterally polarised transducers are not suitable for generating axisymmetric wave modes at low and medium range frequencies. Figure 5.14 and Figure 5.15 shows the surface velocity magnitude against time for 1 conventional Teletest Focus+ transducer and 1 laterally polarised transducer at 60kHz respectively. The results show that there are similar wave mode responses for both transducers and that there are no significant changes in any particular wave modes. Considering the axisymmetric wave mode is of most interest, Figure 5.16 and Figure 5.17 show a comparison of T(0,1) for both types of transducers at 60kHz. The wave mode shape is almost identical for both transducers and therefore the laterally polarised transducers are a suitable replacement for Teletest Focus+ transducers for experiments conducted at low range frequencies.

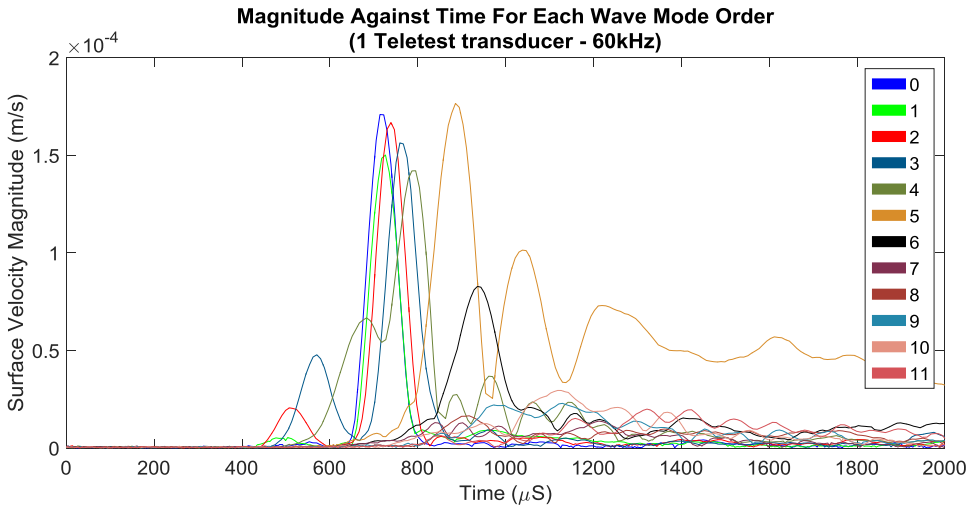

Figure 5.14. Wave mode content of the signals from the laser vibrometer results at 60kHz for 1 Teletest transducer. Order of wave modes are indicated by numbers in the legend.

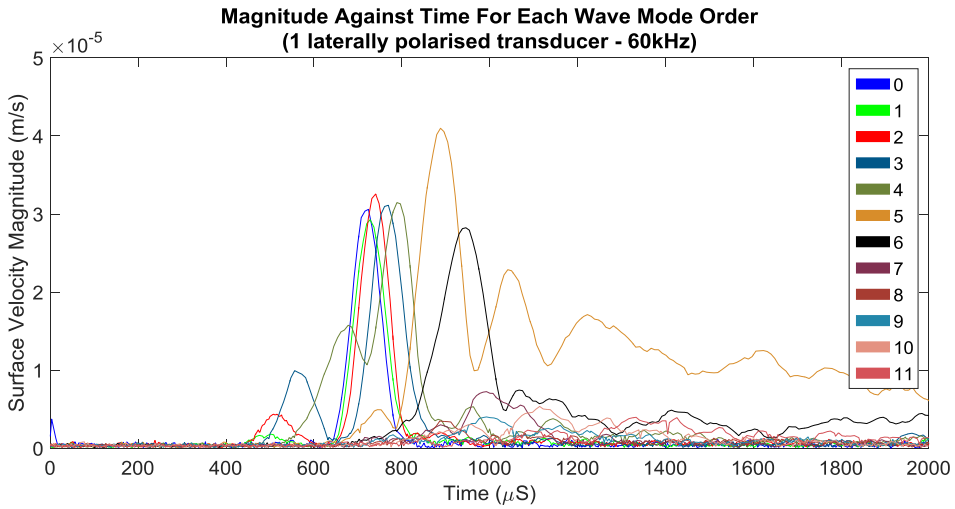

Figure 5.15. Wave mode content of the signals from the laser vibrometer results at 60kHz for 1 laterally polarised transducer. Order of wave modes is indicated by numbers in the legend.

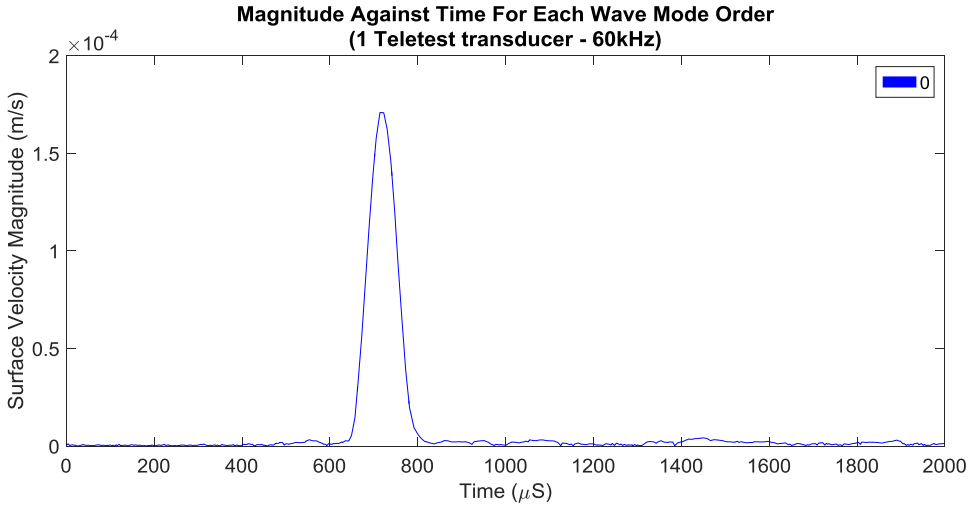

Figure 5.16. T(0,1) surface velocity against time for 1 Teletest transducer at 60kHz.

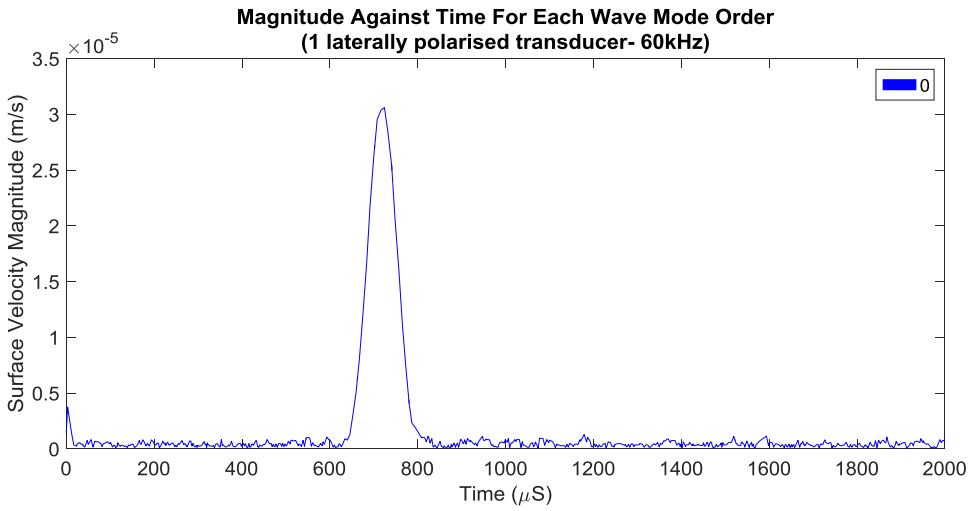

Figure 5.17. T(0,1) surface velocity against time for 1 laterally polarised transducer at 60kHz.

The next stage was to compare the fundamental and higher order flexural wave modes for both transducers at 190kHz shown in Figure 5.18 and Figure 5.19. There is more of a difference in wave mode responses for both transducers at 190kHz in comparison to 60kHz. The difference could be due to the excitability of particular wave modes at medium range frequencies, as transducer motion could vary at higher or particular frequencies. Another factor that can influence the recorded responses is measurement accuracy from the laser vibrometry, considering that any measurement error would have more of an impact at 190kHz due to the wavelength being approximately three times shorter than for a 60kHz signal.

To investigate the extent of this variation the axisymmetric signal response was compared for both transducers at 190kHz and is shown in Figure 5.20 and Figure 5.21. The results from both transducers show that there is leakage from other wave modes, considering that the signal should only consist of the torsional axisymmetric wave modes T(0,1) and T(0,2) at 190kHz for this experimental setup. The experiment shows that there is likely to be contamination from higher order flexural wave modes, which is possibly caused by a measurement offset in the axial direction during the rotation of the pipe. This could cause flexural wave modes to be sampled as axisymmetric wave modes depending on the extent of the axial shift. The positive response from both signals is that the highest amplitude occurs from T(0,1) and T(0,2) respectively. The wave mode

response at 190kHz is a lot more complex in comparison to 60kHz due to the generation and leakage of more flexural wave modes. Considering that the transducers performed relatively equal at 60kHz and that both T(0,1) and T(0,2) were predominant in the axisymmetric filtering for 190kHz, the high density transducer array designed in section 5.5 was developed with the laterally polarised transducers. The array design is based on suppressing the flexural wave modes that exist at both the low and medium frequency testing.

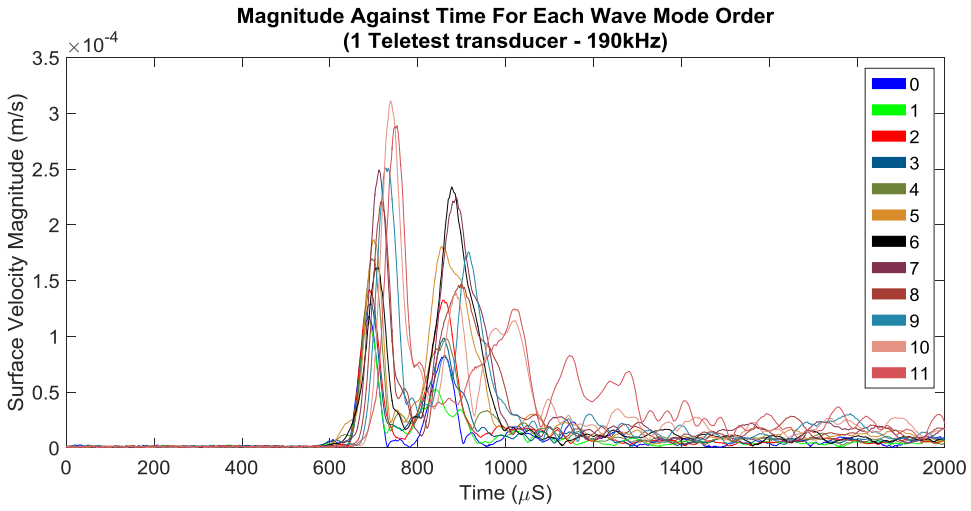

Figure 5.18. Wave mode content of the signals from the laser vibrometer results at 190kHz for 1 Teletest transducer. Order of wave modes are indicated by numbers in the legend.

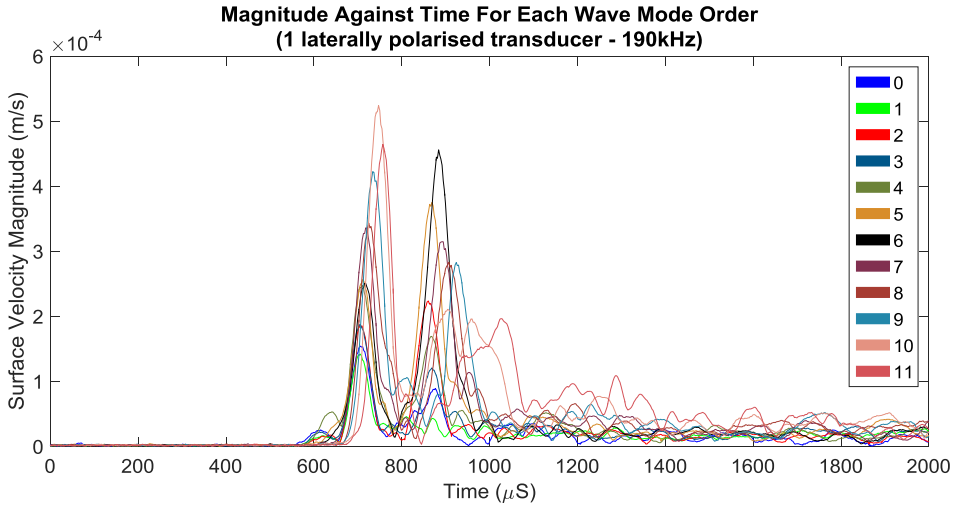

Figure 5.19. Wave mode content of the signals from the laser vibrometer results at 190kHz for 1 laterally polarised transducer. Order of wave modes is indicated by numbers in the legend.

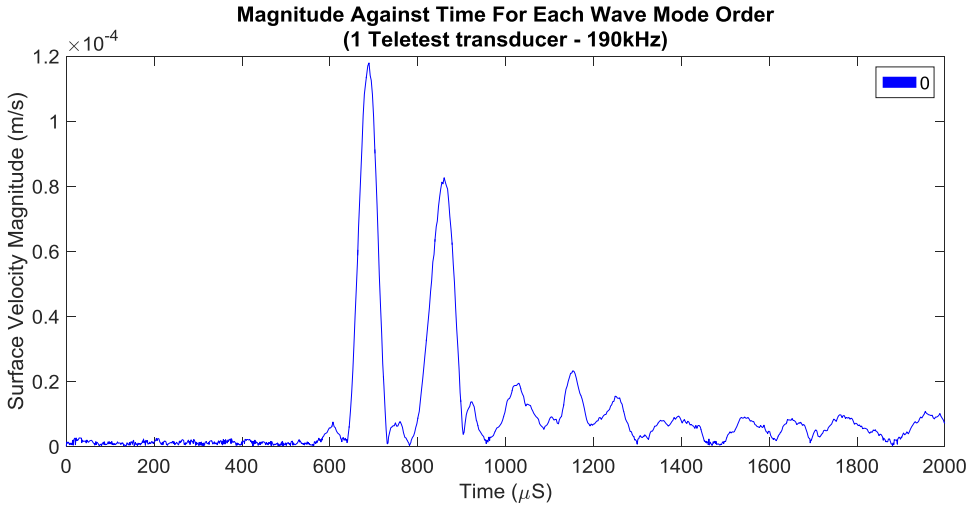

Figure 5.20. T(0,1) surface velocity against time for 1 Teletest transducer at 190kHz.

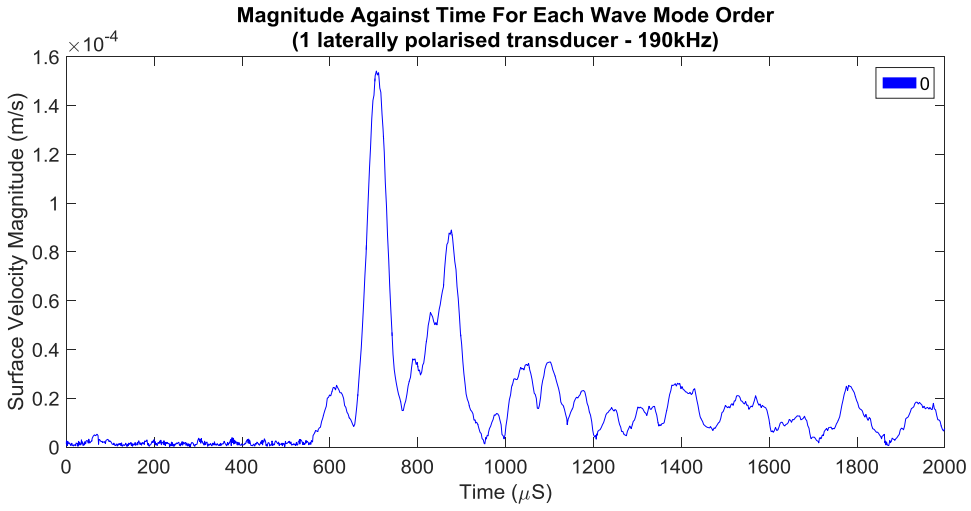

Figure 5.21. T(0,1) surface velocity against time for 1 laterally polarised transducer at 190kHz.

5.5 High Density Array Design

The high density array, developed using the transversely polarised transducers, is shown in Figure 5.22. Each transducer is equally spaced around the circumference and are attached to the pipe using Araldite epoxy resin. Connecting cables were developed to

connect to the pulser-receiver unit. The array has 64 equally spaced transducer elements and are connected in parallel, in blocks of 8 to 8 separate channels on the pulser-receiver unit. The experiment conducted in section 5.3 was repeated and the results for the transmitted signal at 60kHz are shown in Figure 5.23.

Figure 5.22. High density transducer array with 64 piezoelectric elements.

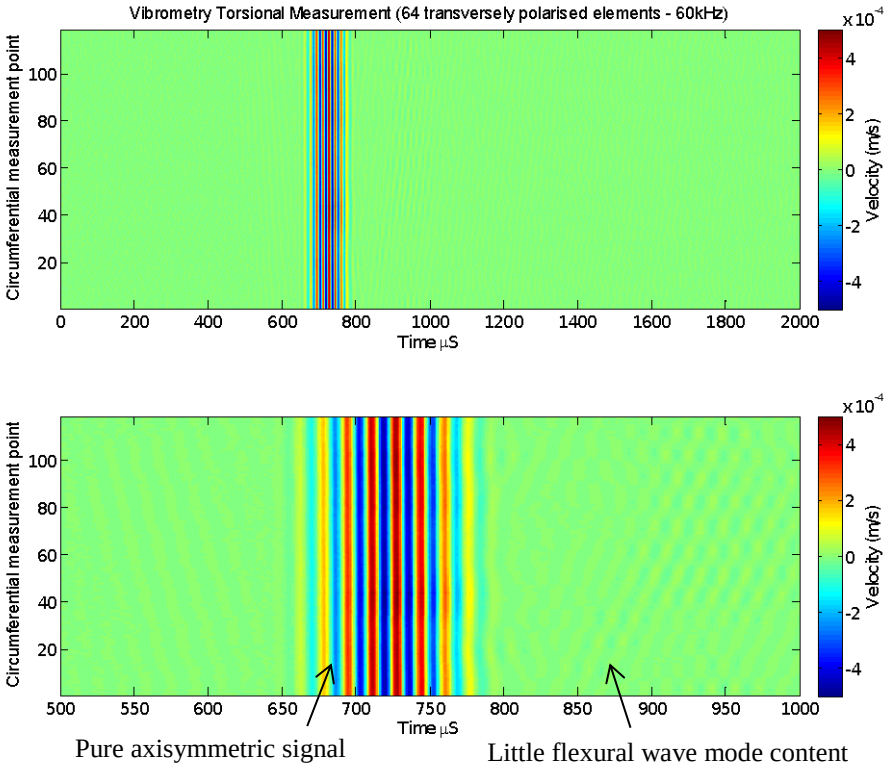

Figure 5.23 Laser vibrometer results showing surface velocity against time for 118 circumferential positions using a 20 cycle Hann windowed pulse at 60kHz for the high density array.

The results show that the high density array provides a purer axisymmetric T(0,1) wave mode response at a low frequency. This will improve the accuracy of defect analysis as the transmitted signal has less contamination from other wave modes. Figure 5.24 shows the results at 190kHz.

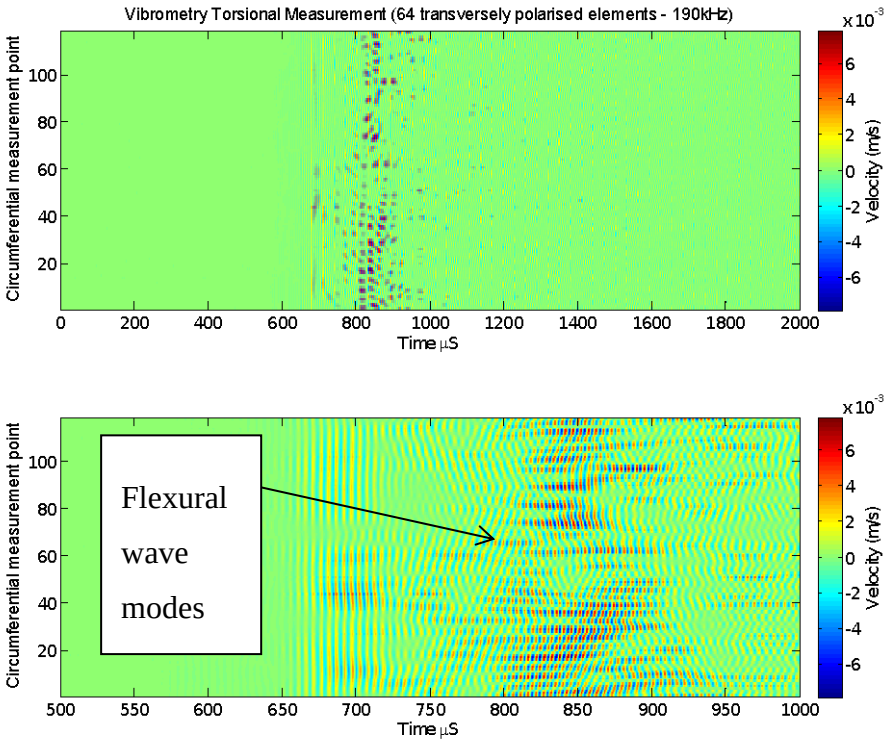

Figure 5.24. Laser vibrometer results showing surface velocity against time for 118 circumferential positions using a 20 cycle Hann windowed pulse at 190kHz for the high density array.

The wave modes are significantly less pure when the frequency is raised to 190kHz. The expected wave modes to be transmitted at this frequency are T(0,1) and T(0,2). The results show that there is a combination of flexural wave modes with this transducer array at 190kHz. These results show that there could possibly be an impact caused by a variation in the transmitted output by one or more transducer elements in the array. Considering that when operating at 190kHz the wavelength is just over three times shorter than when operating at 60kHz the accuracy of the measurements appears to be a lot more sensitive to variations around the circumference and in the axial direction. The pipe used in the experiments was not completely cylindrical due to manufacturing

tolerances and the laser vibrometer has measuring tolerances (Polytec [2009]) when calculating the three dimensional coordinate system. Comparing the results from Figure 5.24 to those with the existing transducer array in Figure 5.7 shows that both arrays contain flexural wave mode content. Therefore, the next stage was to separate the axisymmetric and flexural wave mode content and compare the results to the existing transducer array shown in section 5.3. Figure 5.25 and Figure 5.26 show the magnitude against time for each wave mode up to F(11,n) for 60kHz and 190kHz respectively. The results at 60kHz show that there is a 27.5dB difference between T(0,1) and the highest flexural wave mode present, which is F(1,n). Comparing this to the existing transducer array (Figure 5.5) provides an improvement of 10.7dB for signal to coherent noise. Therefore, the high density array could be capable of detecting smaller defects as there is less contamination from flexural wave modes. Considering the high density array is an improvement at 60kHz the next step was to investigate the wave mode content at 190kHz shown in Figure 5.26. The wave mode content shows that T(0,1) and T(0,2) have the highest amplitude, which was predicted as the array was designed to excite axisymmetric signals. Comparing the results to the existing array presented an unexpected result for direct comparisons of T(0,1) and T(0,2) for each transducer array. The results for the existing transducer array (Figure 5.9) showed that T(0,2) has a higher amplitude response in comparison to T(0,1) whereas the high density transducer array has a higher T(0,1) response (Figure 5.26). To determine this variation further analysis on both transducer arrays were conducted in section 5.6.

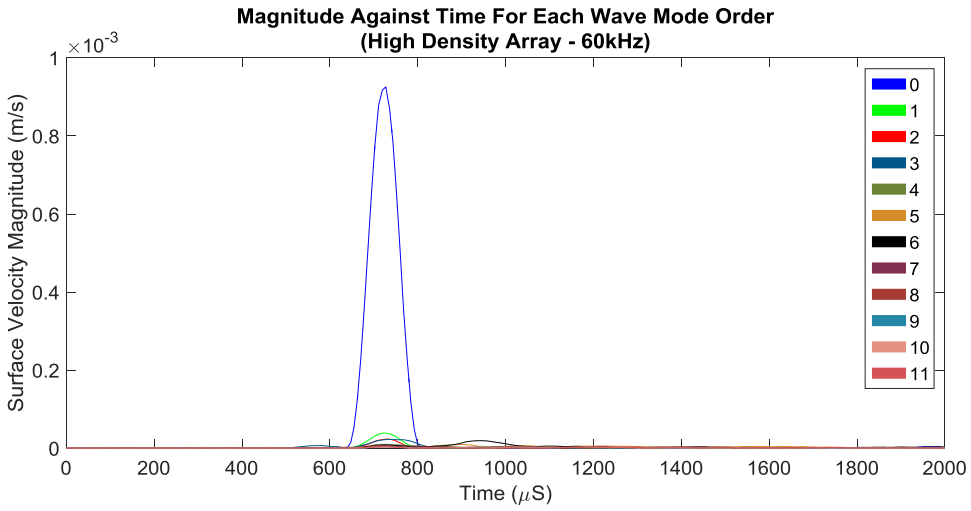

Figure 5.25. Wave mode content of the signals from the laser vibrometer results at 60kHz for the high density array. Order of wave modes are indicated by numbers in the legend.

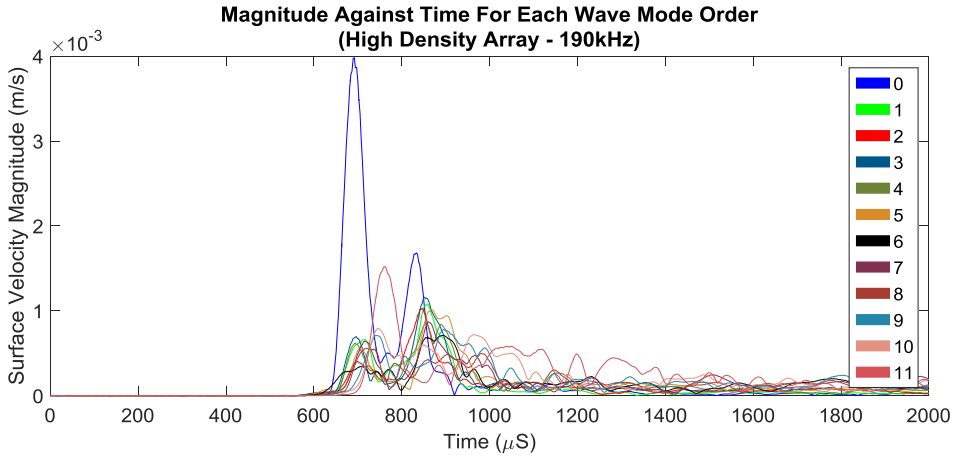

Figure 5.26. Wave mode content of the signals from the laser vibrometer results at 190kHz for the high density array. Order of wave modes are indicated by numbers in the legend.

5.6 Existing Transducer Array versus High Density Transducer Array

To identify the axisymmetric response from both the existing transducer array and the high density array the sum of the signals from each reception position collected by the

laser vibrometer was analysed. Summing the signals at every reception point should produce a signal containing only T(0,1) and T(0,2) wave modes, as they are both axisymmetric and all the other wave modes that exist at this frequency are flexural. Figure 5.27 shows the amplitude of T(0,1) for the existing transducer array (left) and the high density array (right) for 60kHz using the laser vibrometer to record the incident wave.

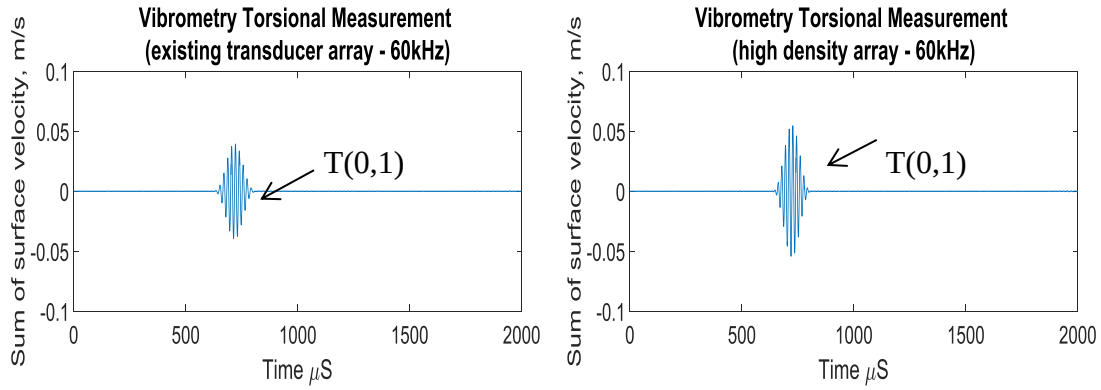

Figure 5.27. T(0,1) surface velocity against time for the existing transducer array (left) and the high density array (right) at 60kHz.

The results show that the signal to noise ratio for the high density array is 3.5dB greater than the existing transducer array. This increase will provide greater response from features and defects making their detection easier and more likely. The results for 190kHz for the existing transducer array and the high density array are shown in Figure 5.28.

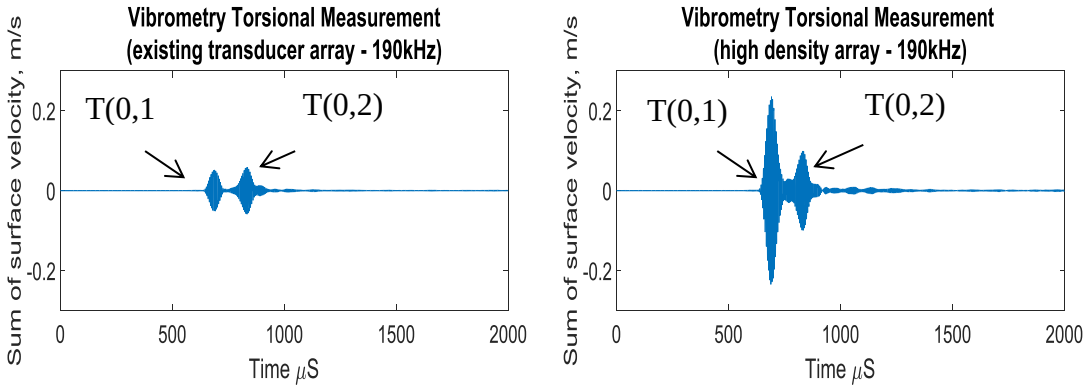

Figure 5.28. T(0,1) and T(0,2) surface velocity against time for the existing transducer array (left) and the high density array (right) at 190kHz.

The results show that there is some leakage of flexural wave modes into the axisymmetric signals of T(0,1) and T(0,2). The first difference between both arrays is that the T(0,1) wave mode is approximately 12dB more than the existing transducer. This can provide a greater response from defects and greater propagation distances as the signal will take a longer distance to fully attenuate. Attenuation has more of an impact for higher frequencies therefore a power increase in the transmitted signal is important. The amplitude for T(0,2) is approximately 6dB greater in the higher density array. The main difference between both transducer arrays is the ratio of T(0,1) and T(0,2). The existing array excites T(0,2) with a greater amplitude than T(0,1) while the opposite occurs for the high density array. To investigate this variation finite element modelling of both transducer arrays was conducted.

To investigate the variation in the experimental results a model representing the pipe experiment was created in ABAQUS Explicit 6.12 (described in chapter 4 section 4.3) and the high density array was applied by assigning 64 point loads. Each point had a 190kHz 20 cycle Hann windowed pulse input signal with equal amplitudes. Figure 5.29 shows the finite element results for T(0,1) and T(0,2).

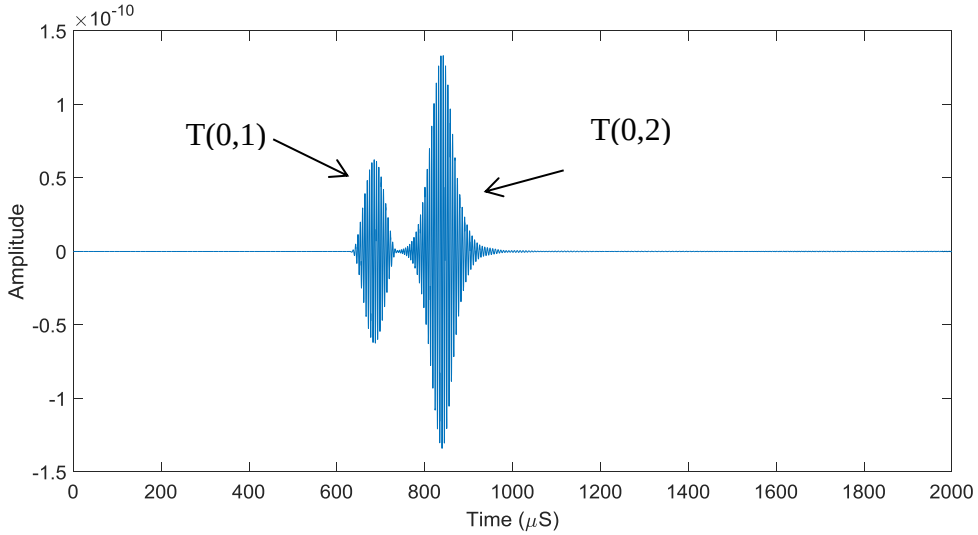

Figure 5.29. FEA signal of T(0,1) and T(0,2) for a point load at 190kHz.

The finite element results show that there is more similarity to the existing array rather than the high density array due to T(0,2) having a higher amplitude than T(0,1). The next stage was to investigate the transducers used and the loading conditions of the model. Considering that the transducers in the high density transducer array have an active length of 10mm, rather than applying the loading as point sources the model was altered to a line, which consisted of 14 excitation points (constrained by element length) to represent the 10mm length of the transducers. Figure 5.30 shows the response for T(0,1) and T(0,2), which is a more accurate representation of the experimental results considering T(0,1) is now greater in amplitude than T(0,2).

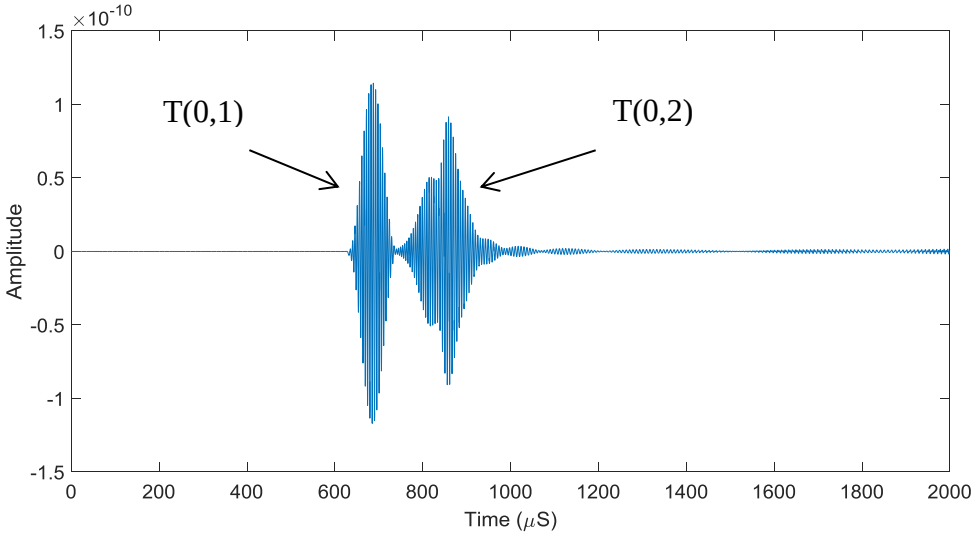

Figure 5.30. FEA signal of T(0,1) and T(0,2) for a line of point loads at 190kHz.

In order to get a direct comparison of the experimental results for the high density array and both models, a normalised graph with respect to T(0,1) is shown in Figure 5.31.

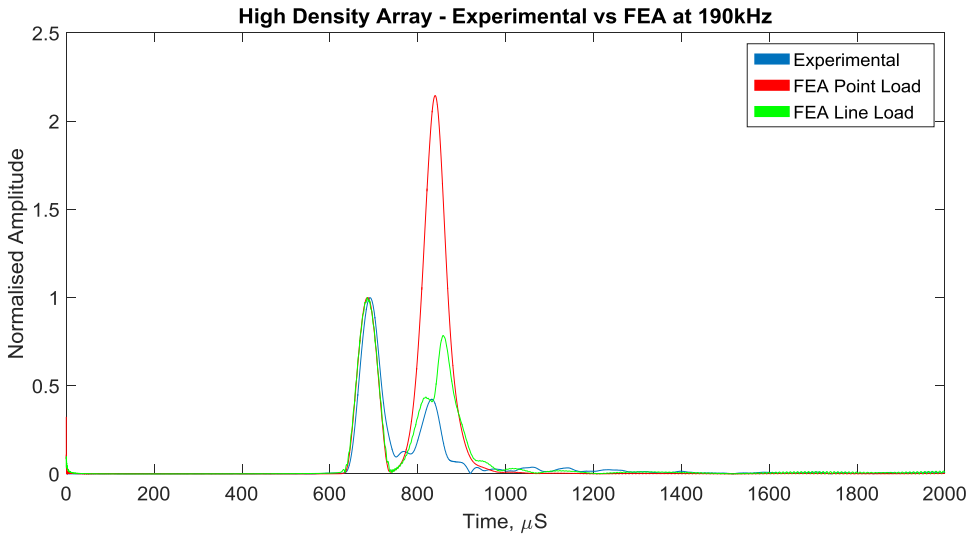

Figure 5.31. Experimental, FEA point load and FEA line of point loads for 190kHz. Signals are normalised to T(0,1).

The results which are normalised to T(0,1) show that the T(0,1) pulse shape is unchanged suggesting that the transducer length has a negligible impact on this wave mode, but has a significant impact on T(0,2). However, the relationship between transducer lengths were investigated further for both wave modes with respect to the design setup used. The first step was to investigate the wavelengths of T(0,1) and T(0,2) at 190kHz from the relative velocities obtained from the dispersion curves shown in Figure 5.32.

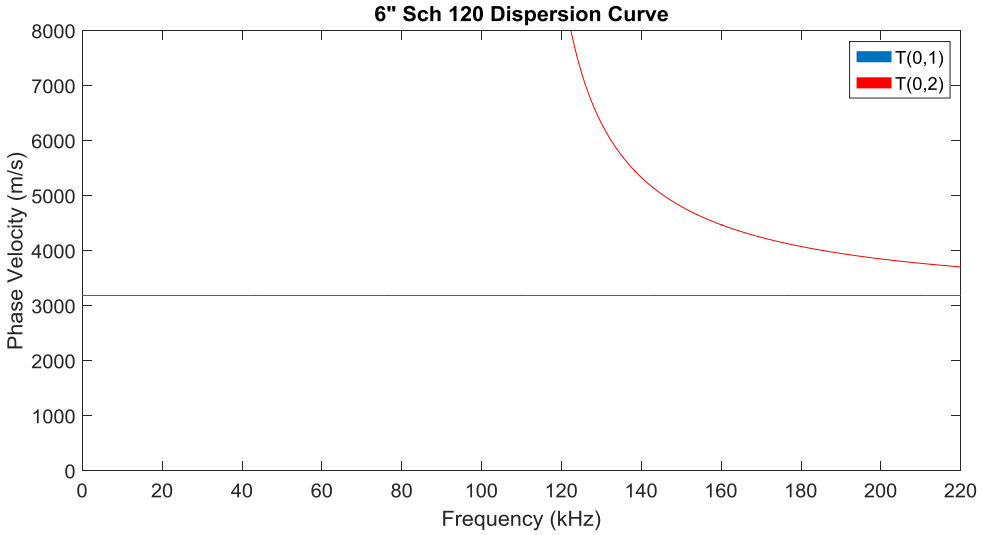

Figure 5.32. Dispersion curve showing phase velocity against frequency for T(0,1) and T(0,2).

The phase velocity for T(0,1) and T(0,2) is 3189m/s and 3952m/s for 190kHz respectively. Using Eqn. 5.2 where C is phase velocity, f is frequency and $\boldsymbol{\lambda}$ is wavelength, the corresponding wavelength for T(0,1) and T(0,2) is 16.7mm and 20.8mm respectively.

$$\boldsymbol{C = f\lambda} \qquad \textbf{(5.2)}$$

The next step was to compare the wavelength of both wave modes to a varying transducer length. A number of equally spaced point sources were considered to

represent a variable length transducer. Each point was considered to transmit a sine wave of 190 kHz to a common receiver point. However, to equally distribute the transmission energy along the transducer, the signals were normalised by dividing the total results from each transducer length by the number of points. The peak amplitude, A, due to superposition of a set of points (with each point P at a distance away from a receiver of x_p) can be calculated for a frequency, f, using the following equation:

$$\boldsymbol{A = max\left(\frac{1}{N}\sum_{P=1}^{N} sin\left(2\pi ft - kx_p\right)\right)} \tag{5.3}$$

$$\boldsymbol{0 \leq t < \frac{1}{f}} \tag{5.4}$$

where k is the wavenumber ($2\pi/\lambda$) and N is the total number of points. The length of a transducer can be evaluated using this equation by considering different sets of points where the points are distributed over various lengths. Figure 5.33 shows the transmission amplitude of T(0,1) and T(0,2) for a variety of transducer lengths based on the superposition of equally distributed excitation points along the length. This depicts the results for individual frequencies, whereas testing will be conducted with a bandwidth.

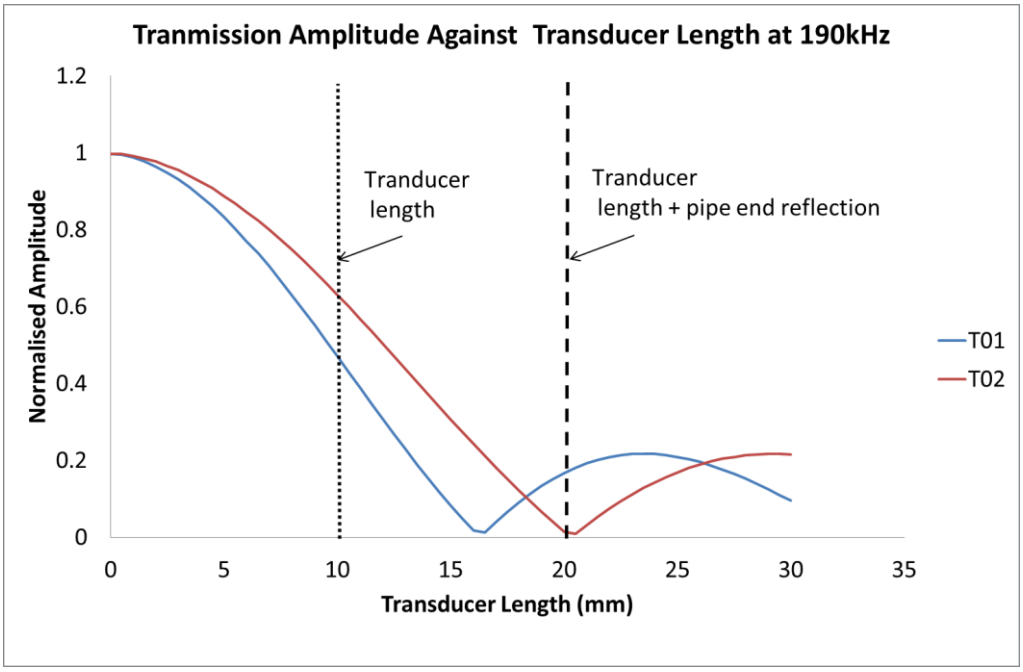

Figure 5.33. Transmission amplitude against transducer length for T(0,1) and T(0,2).

This only considers the effect of superposition and these results do not include the excitability of each mode. The results show that as the length of a transducer increases from a point source, the superposition of the signals decrease the total amplitude of the transmitted signal. When the transducer length is 1 wavelength of both wave modes, the transmitted signal is at a minimum. The length of the transducer is 10mm, which shows that T(0,2) should be less affected than T(0,1); however, the results show the opposite effect. The additional influence that affects the transmitted signal is the superposition of the signals reflected from the pipe end. By positioning the transducers on the pipe end effectively doubles the length of the transducer because the backward propagating signal from the maximum 10mm length reflects off the pipe end and travels another 10mm back to the same position. This gives an effective transducer length of 20mm, which is approximately the wavelength of T(0,2), where the transmitted signal has minimum amplitude shown in Figure 5.33. Under the same condition T(0,1) has a greater transmitted signal in comparison to T(0,2). Figure 5.33 can also be described as a diffraction curve (Stamnes [1986]). This negative impact has reduced T(0,2) from having the highest transmitted amplitude shown in Figure 5.29 in comparison to T(0,1), to the least transmitted amplitude shown in Figure 5.30.

5.7 Defect Analysis

Although the length of the transducers and the pipe end positioning have a negative impact on T(0,2) it is important to analyse the performance of the high density arrays with defects. To create axisymmetric defects the pipe was rotated in a lathe which grooved full circumferential slots. Three different size slots (machined in the same location) were analysed at 12.5%, 25% and 50% depth. Figure 5.34 shows the results for a low frequency test at 60kHz for the summation of all 118 equally spaced receiver positions.

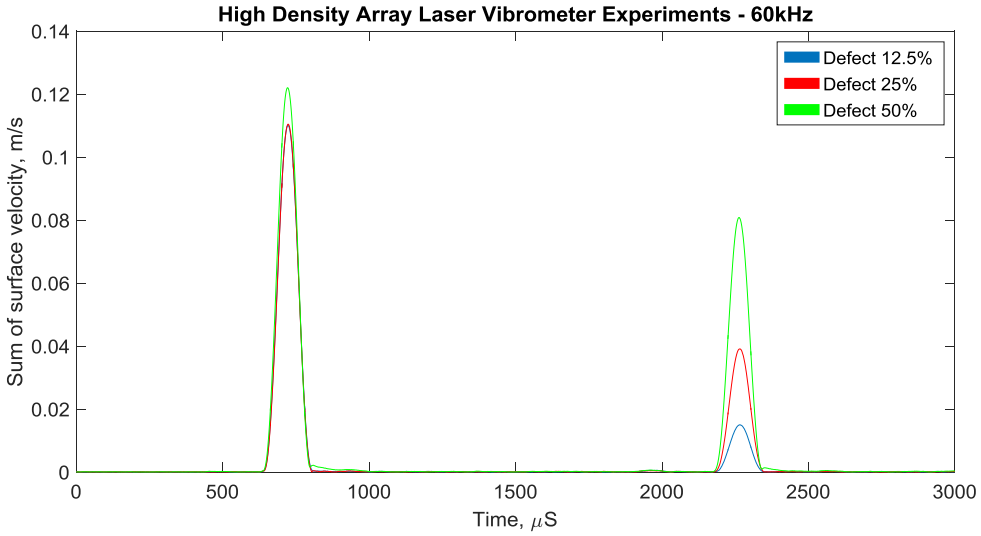

Figure 5.34. Signal responses for a axisymmetric defects with depths of 12.5%, 25% and 50% at 60kHz.

The first pulse shows the T(0,1) incident wave for all three defect cases. The incident waves for the 12.5% and 25% cases show that they are almost identical and there is a less than 1dB difference between these two cases and the 50% defect, which shows that there were negligible differences or changes to the performance between all three experiments. The second pulse shows the defect response for all three defects and as expected the reflected amplitude from defect increases when the depth and size increases. The reflection coefficient values for T(0,1) are linear with respect to defect

size, which was validated by Carandente *et al.* [2012] up to an approximate depth of 75%.

The second set of experiments were conducted at 190kHz and the steps taken for the previous experiments at 60kHz were repeated. Figure 5.35 shows the results for a 12.5%, a 25% and a 50% defect. It is important to note that for each defect size the experimental setup was conducted using the same steps apart from the frequency change from 60kHz to 190kHz.

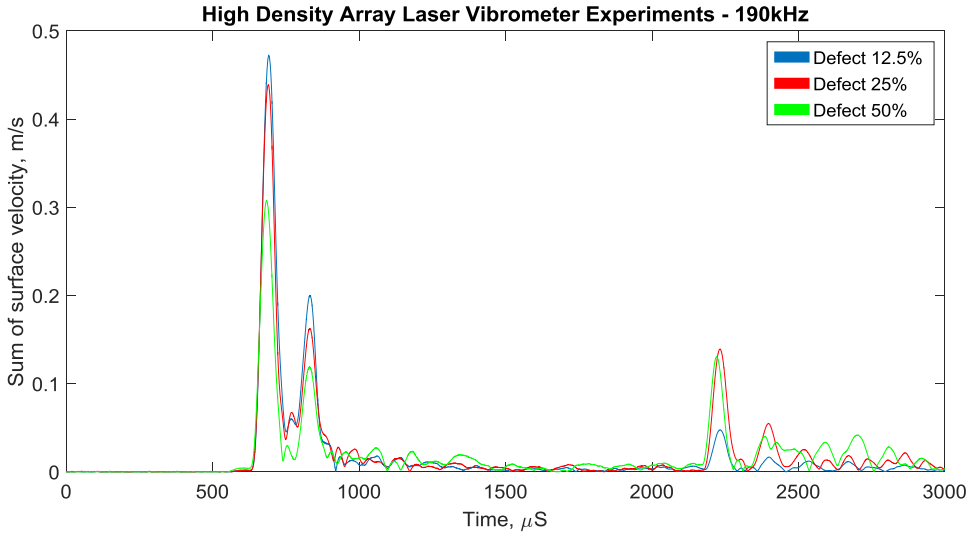

Figure 5.35. Signal responses for a axisymmetric defects with depths of 12.5%, 25% and 50% at 190kHz.

The results show that at 190kHz both T(0,1) and T(0,2) are excited and are clearly separated as they propagate 2 metres, as predicted in chapter 4 section 4.2. The defect responses are clearly shown for T(0,1) for all size defects and there are peaks related to the mode conversion of T(0,1) into T(0,2). The peaks for T(0,2) are relatively difficult to determine due to the reduction in amplitude caused by the length of the transducers.

5.8 Conclusions

This chapter investigated the feasibility of developing a transducer array design capable of performing under medium frequencies. The experimental setup described in chapter 4 was used to investigate the current transducer array and to develop the high density transducer array for medium range inspection. The analysis was based on identifying the current performance of the current array design and improving the array to perform using medium range frequencies. The areas investigated were transducer array design to improve the transmission of torsional wave modes at medium range frequencies and sufficiently sample higher order flexural wave modes, based on the dispersion curves and their characteristics. The next step was to address the transducer array gap in the existing transducer array to improve the transmission of axisymmetric wave modes and supress flexural wave modes. Different size defects were then analysed to compare the performance of the high density array with respect to the current array design using both low and medium range frequencies for the purpose of defect sizing.

The high density array provides greater wave mode purity at 60kHz in comparison to the existing array because there is a consistent signal response from each received position around the circumference. Eliminating the gap that is currently present in the existing transducer array provided a reduction in flexural wave mode content and wave mode separation also showed that there is a significant improvement on the signal to coherent noise ratio of 10.7dB , which can improve defect detection and identify smaller defects.

Applying the methods used for low frequency array design for medium frequency was challenging. The high density transducer introduced destructive interference to the axisymmetric wave modes caused by the length of the transducers, which has relatively low impact at low frequencies. Therefore, additional measures need to be included in the guidelines to feasibly adapt the current methods used in transducer design for medium frequencies. To adequately transmit T(0,2) with constructive interference in

comparison to the destructive interference exhibited in this chapter a recommended transducer length of approximately ¼ wavelength or less for T(0,2) should be used.

Other factors could have had an impact on the accuracy of the results. The first is an unbalanced transducer array caused by the output of the transducers, which can have a noticeable effect at medium frequencies as many more flexural modes can be excited with greater amplitudes. In order to overcome this, a pulser-receiver with a greater number of channels needs to be developed so that each transducer can be addressed individually, this can allow normalisation of each transducer and provide a more balanced transducer array. Considering that this equipment is currently unavailable to conduct this analysis, this was not an option to progress the study of medium range frequency inspection. Another impact on the accuracy of the results was the current method used for low frequency finite element modelling, which is based on point loading. The analysis in this chapter showed point loading is an inaccurate way to model at medium range frequencies if the transducer length has an impact on the transmitted wave mode. The smaller the length of the transducer, the closer the excited wave modes are to the finite element modelling. This was proven by comparing the high density transducer array with the existing transducer. Therefore, to continue the study of medium range frequencies, technique development and signal processing has been investigated in chapter 6 for defect sizing using finite element modelling. This provides a technique to be explored experimentally using the development of smaller length transducers.

6 DEFECT SIZING USING WAVE MODE T(0,2) BASED ON FINITE ELEMENT ANALYSIS

6.1 Introduction

This chapter provides a technique for defect sizing using T(0,2) based on FEA. From the experimental analysis in chapter 5, it was discovered that the length of the transducer has a significant impact when operating at medium range frequencies. The defect analysis performed is this chapter is based on the capability of testing the technique using smaller transducers (approximately ¼ the wavelength of T(0,2)).

This chapter investigates the use of guided waves at medium range frequencies (160-200kHz) using FEA for the inspection of pipes. Considering there is an industrial need for this type of inspection (described in chapter 5), a technique based on medium range frequency using the second order torsional wave mode T(0,2) would provide additional defect sizing information unavailable at low range frequencies. Operating at medium range frequencies can also improve defect sensitivity, spatial resolution and reduce dead

zones enabling shorter range inspection. To the best of the author's knowledge, sizing defects using medium range frequencies particularly using the T(0,2) mode has not been presented in the literature. Enhanced modelling techniques for guided wave inspection are also presented in this chapter to feasibly investigate relatively small defects (below 0.5mm increments), which are difficult to accurately machine experimentally. In order to investigate these small defects a modified pipe model was created (see chapter 4 section 4.3). In addition to this broadband signals were used to gather a range of frequency data for one particular model. This made the FEA a feasible exercise for obtaining a large range of frequency responses for each defect size without running individual models for each frequency.

In order to investigate the characteristics of torsional excitation a variety of pipe models and parameters were created to replicate the pipe investigated in chapter 5. The areas investigated in this chapter include:

- Defect sizing using a full FEA model to replicate the experiments conducted in chapter 5.
- Modified finite element models in order to investigate more defect sizes and improve computational performance.
- Broadband signal inspection to allow multiple frequency analysis from one processed model.
- A technique for identifying defect sizes using T(0,2) based on reflection coefficients.

The chapter begins by investigating the wave mode characteristics of T(0,1) and T(0,2) for the purpose of signal separation. This is primarily used to validate the pipe model conditions used. Following from this a range of defect sizes are investigated using a full pipe model and for a simplified pipe model segment to allow for smaller defect sizes to be analysed. Further enhancements to the FEA procedure were investigated using broadband signals to feasibly investigate defects with a wide frequency spectrum to

reduce the number of simulations. Finally, using the results a technique based on T(0,2) for defect sizing was developed.

6.2 Wave Characteristics and Signal Separation

The wave mode characteristics of T(0,1) and T(0,2) are fundamental to proving the finite element model parameters are correctly configured in order to produce pure torsional wave propagation. Particularly, the wave mode shape which determines through thickness displacement and the axisymmetric nature of T(0,1) and T(0,2), which are used to separate the signals.

The unique advantage of finite element modelling is the capability of recording signals on the inner surface whereas this is relatively impossible in practical conditions. It is important to note that the following technique is to prove model conditions are setup correctly and is not expected to be conducted in practical applications. The advantage of this is the ability to separate T(0,1) and T(0,2) due to the nature of their displacement patterns, shown in Figure 6.1 created from Disperse software (Pavlakovic et al [1997]). To separate or remove T(0,1) from the signal the outer signal response minus the inner signal response will leave an A-scan consisting only of T(0,2). To separate or remove T(0,2) from the signal the outer signal response plus the inner signal response will leave an A-scan consisting only T(0,1). Processing the signals using this method gives a clear indication to amplitudes and pulse shapes of each transmitted, received and mode converted signal. Before each wave mode can be completely separated a scale factor needs to be applied either at the outer or inner surface of the incident wave mode to the mode intended to be removed from the signal, which is determined by the amplitude difference on the inner and outer surface of the pipe. The displacements vary slightly on the inner and outer surface for each wave mode due to circumferential variation, whereas if the was pipe unrolled into a plate it would have the same displacement pattern on the bottom and top for the equivalent SH_0 and AH_1 plate wave modes shown in Figure 6.2.

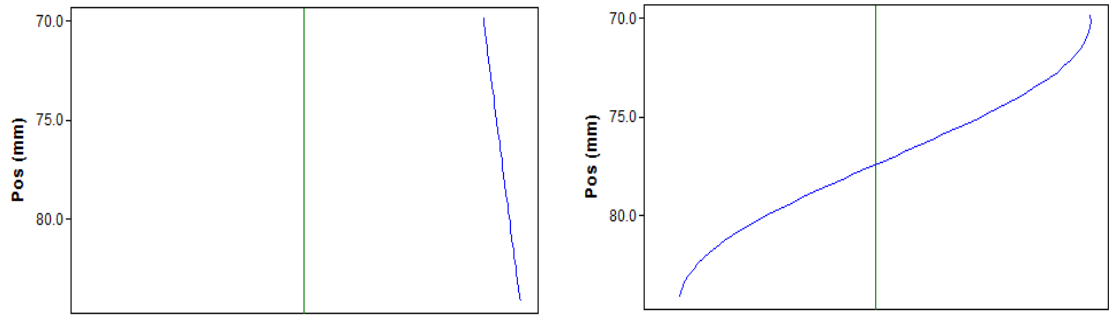

Figure 6.1. T(0,1) (left) and T(0,2) (right) through thickness displacement patterns.

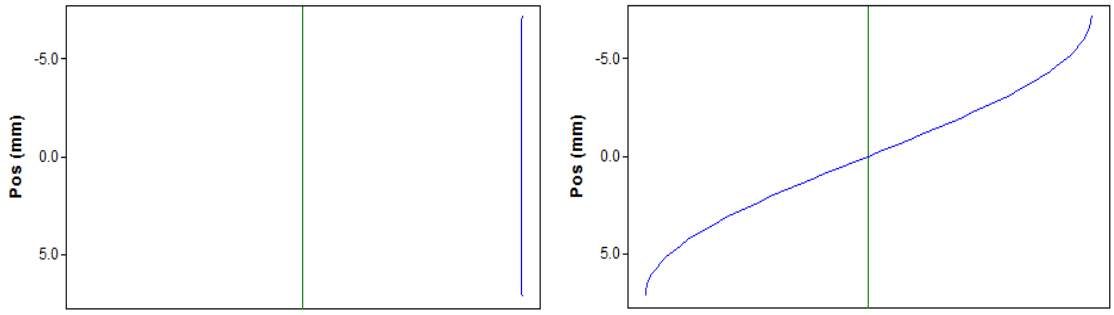

Figure 6.2. SH_0 (left) and AH_1 (right) through thickness displacement patterns.

This technique was performed on a full pipe model to represent the experiments conducted in chapter 5 (details of the model are given in chapter 4 section 4.3). The signal response in Figure 6.3 is for an axisymmetric defect of 50% depth at a frequency of 190kHz. According to the dispersion curves in chapter 4 the only two axisymmetric wave modes that exist at 190kHz are T(0,1) and T(0,2). Figures 6.4 and 6.5 show the separated T(0,1) and T(0,2) responses respectively whereby the sum of each signal returns to the original signal to show the correct scale factors have been applied to each wave mode.

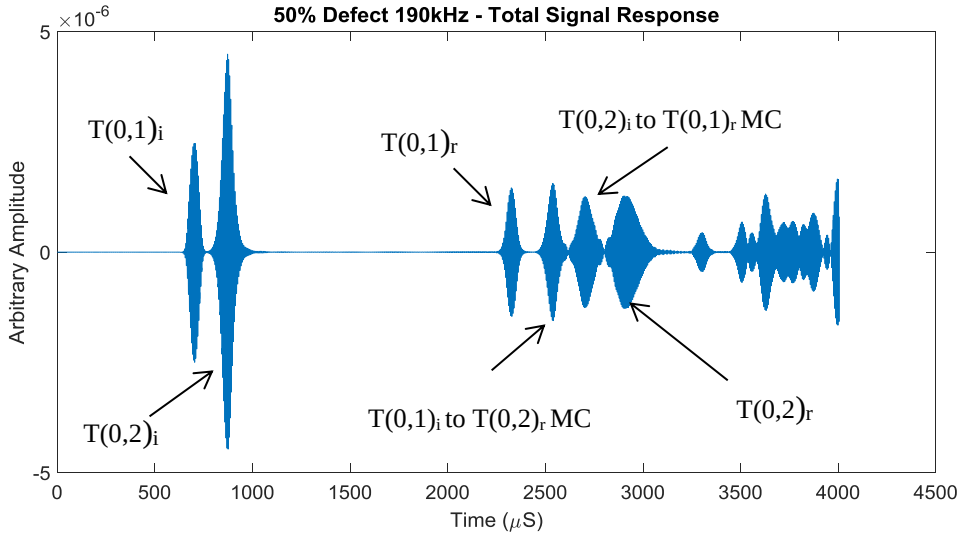

Figure 6.3. FEA signal response for a 50% depth defect using a 190kHz 20 cycle Hann windowed pulse. $T(0,n)_i$ is the incident wave and $T(0,n)_r$ is the reflection. MC is Mode Conversion.

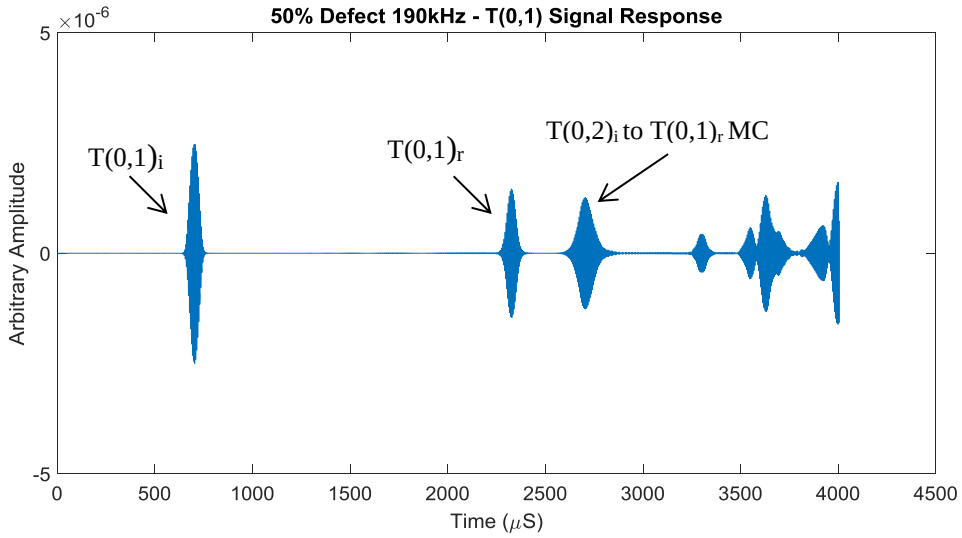

Figure 6.4. T(0,1) signal response for a 50% depth defect using a 190kHz 20 cycle Hann windowed pulse. $T(0,n)_i$ is the incident wave and $T(0,n)_r$ is the reflection. MC is Mode Conversion.

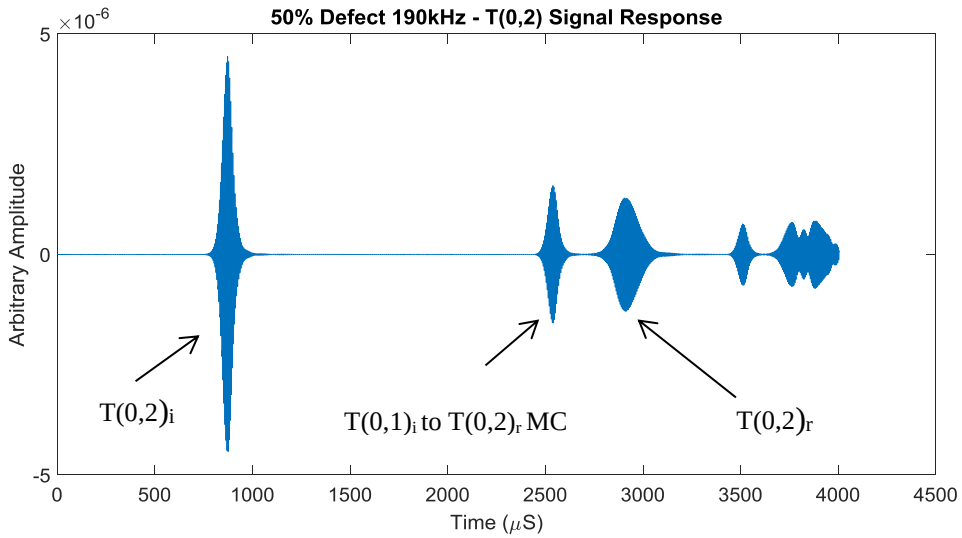

Figure 6.5. T(0,2) signal response for a 50% depth defect using a 190kHz 20 cycle Hann windowed pulse. $T(0,n)_i$ is the incident wave and $T(0,n)_r$ is the reflection. MC is Mode Conversion.

To check that the array of excitation points around the pipe are uniformly distributed each signal from any receive point in the same axial position should be identical. Non identical signal responses will show flexural wave mode contamination and this suggests an uneven distribution of excitation points or a non-symmetrical reflector. The received signals were identical at each received point around the circumference validating that the model was correctly setup.

6.3 Defect Sizing Using Narrowband Signals - Full Pipe FEA Model

The full pipe model used in this section is set up to represent the experiments conducted in chapter 5 using the high density array. Publications mentioned in chapter 3 section 3.4 have successfully used finite element modelling for guided wave analysis, which have been validated experimentally. Therefore, the same approach has been used to investigate medium range frequencies. The purpose of this model is to investigate the T(0,2) with respect to a number of defects, which will be used to validate the modified pipe segment model in section 6.4. The pipe modelled is a 6 inch schedule 120

(168.3mm outer diameter and 14.3mm in thickness) and is 6 metres in length. The material properties of the steel used were:

- Density = 7850kg/m^3
- Young's Modulus = 207GPa
- Poisson's Ratio = 0.3

The signal input used was a 190kHz 20 cycle Hann windowed pulse and was applied as a concentrated force to 64 equally spaced point loads to represent the positioning of the transducers for the experiment conducted in chapter 5 section 5.5. To analyse the response of T(0,1) and T(0,2) from the received position 8 models were created to investigate 8 defect depths (the setup is shown in chapter 4 Figure 4.4), which is the maximum capacity for this particular model dictated by the number of elements through the thickness. The depth of each defect for this mesh size is approximately 1.79mm and the axial length is 10mm. The model has over 8 million elements and is approaching the maximum computational capabilities of the server used to run these models. A set of nodes were created at the receiver position to record the history output. The data collected at each node should be identical considering the loads and defects are axisymmetric. Figure 6.6 shows the model used in the FEA.

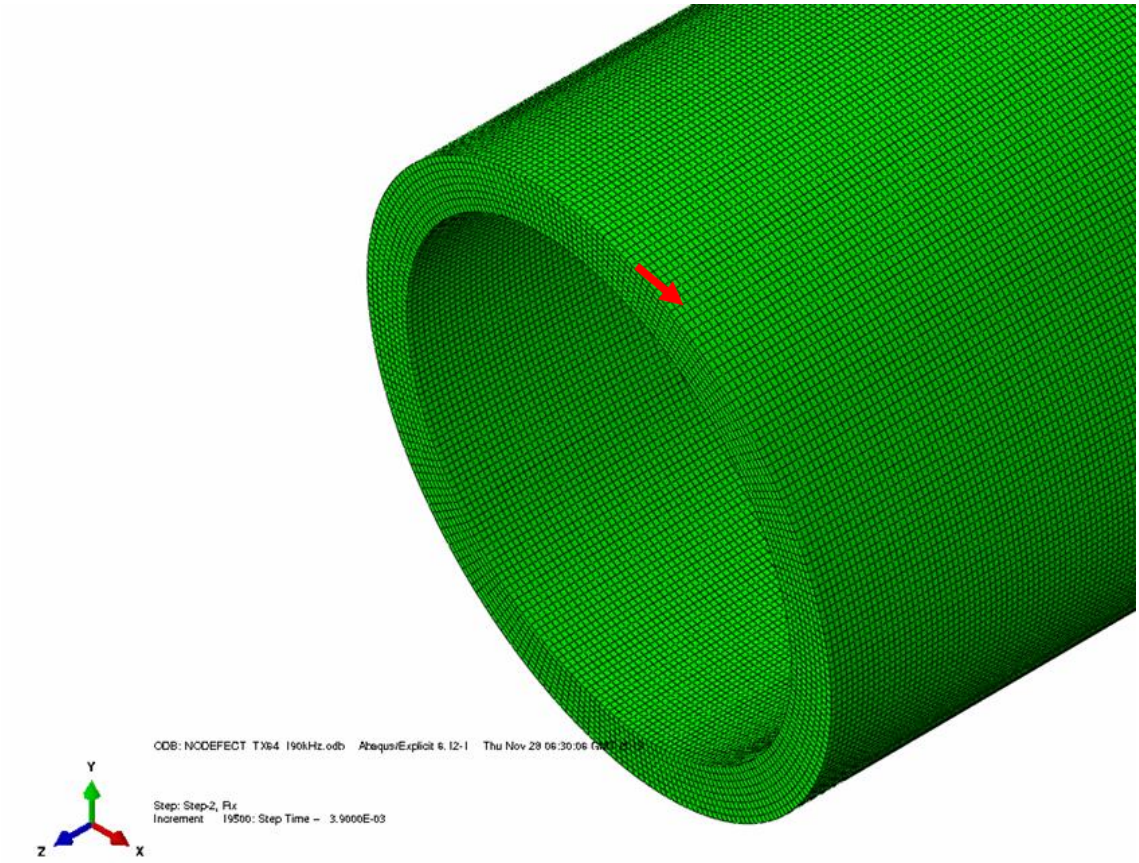

Figure 6.6. Full pipe FEA model. Element lengths approximately 1.79mm.

The data obtained for each defect size provide signal responses for T(0,1) and T(0,2). To investigate the signal responses each reflection coefficient was calculated for each defect size and the amplitude for each combination is shown in Figure 6.7. The results were obtained by measuring the peak amplitudes of the incident and reflected wave modes in order to calculate the reflection coefficients. This was calculated using the gated regions to measure each wave mode based on the velocity of T(0,1) and T(0,2) at 190kHz and the propagating path of each response. The results show that there is a non-linear relationship for all reflection coefficient calculations whereas there is a linear response for T(0,1) at low frequencies shown by Carandente *et al.* [2012]. A clear response is the reflection coefficient for the T(0,2) to T(0,2) response at a 37.5% wall loss. This peak in reflection coefficient is an indication of measureable characteristics that is dependent on flaw size and hence has potential for use in a practical flaw sizing technique. However, to investigate it further would require the modelling of finer

increments in defect size, which is not possible with the full pipe approach because the number of elements required exceeds available computational resources. To overcome this limit, a means of virtual three dimensional modelling was used where a pipe segment was modelled in such a way that it could represent a full pipe and therefore investigate wave behaviour in a full pipe with much fewer elements.

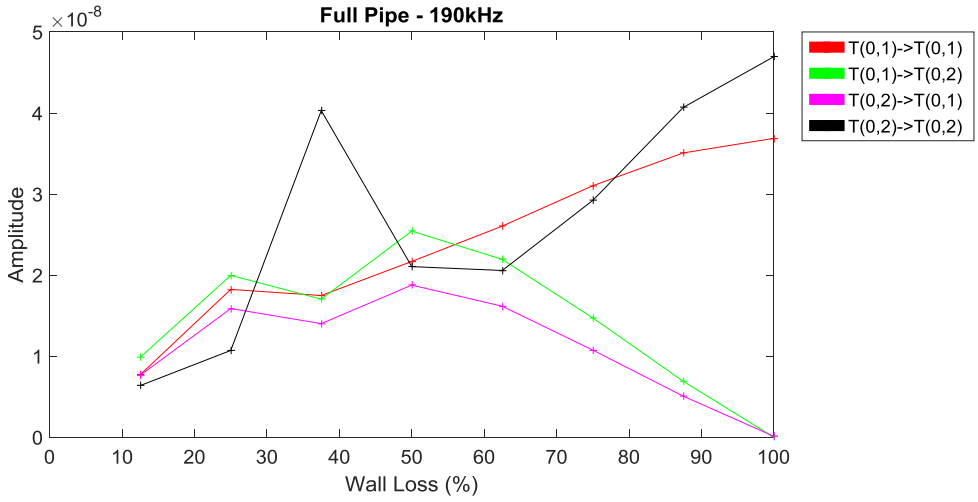

Figure 6.7. Full pipe FEA model showing amplitude against wall loss at 190kHz.

6.4 Defect Sizing Using Narrowband Signals - Modified Pipe Segment

The modified pipe segment created in this section can be used to represent the full pipe model (Section 6.3), but with far fewer elements thus making a finer mesh and the study of finer increments of defects possible. The advantage of using the pipe segment is that the model is 256 times smaller, which provides the ability to decrease the element sizes and investigate a greater number of defect sizes without reaching maximum computing capabilities. The computing time is considerably reduced to minutes instead of the hours needed to compute the full pipe model for a single frequency. The model exploits rotational symmetry considering that the excitation points are equally distributed and the defect is axisymmetric. Tie constraints are used on the sides of the pipe segment to virtually represent the full pipe model (details are described in chapter 4 section 3.4).

The pipe segment has a width equivalent to the distance between two loading points in the full pipe model. A single point load is applied and a single point is used as a receiver to collect the data. In order to portray a full pipe from the segment, tie constraints must be applied to the sides of the segment. This will translate the node displacements from one side to the other, which will simulate neighbouring point loads in a full pipe. Figure 6.8 shows the pipe segment.

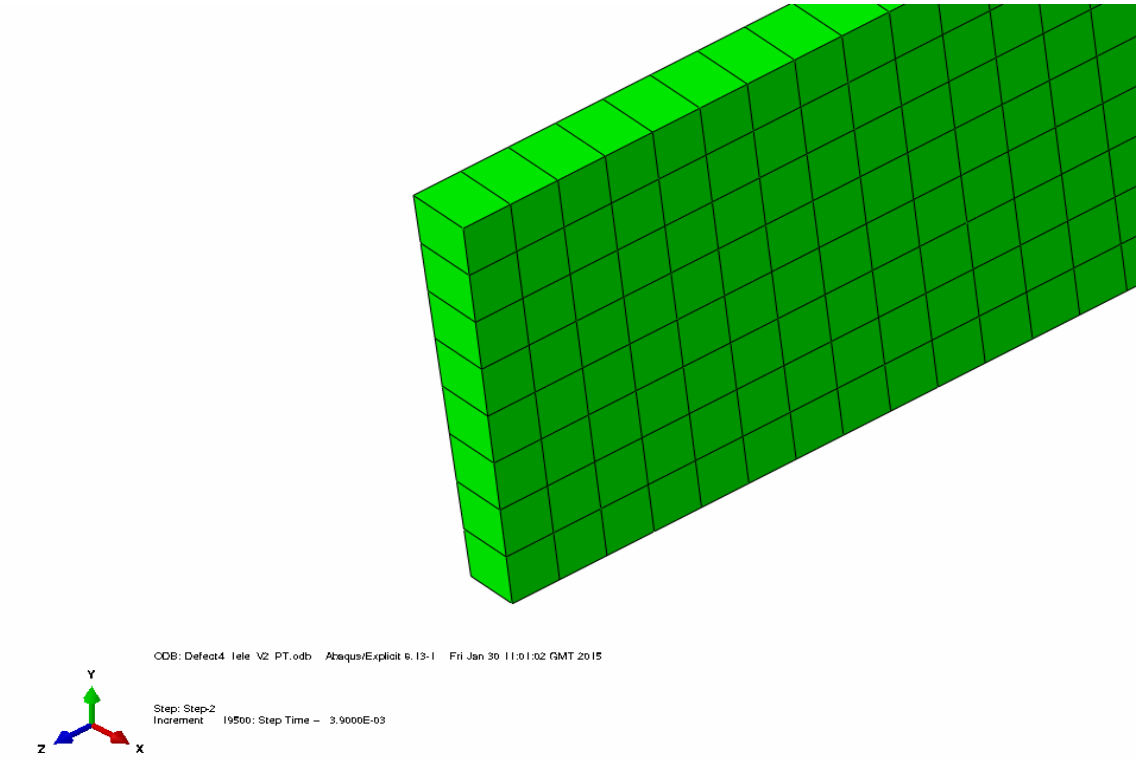

Figure 6.8 Modified pipe segment FEA model. Element lengths approximately 1.79mm.

In order to check that the pipe segment model has sufficiently similar wave propagation characteristics to the full pipe model a direct comparison was made of the reflection coefficients. The results for the full pipe are shown in Figure 6.7 and the results for the pipe segment are shown in Figure 6.9. The difference between the results is less than 2% for the T(0,2) to T(0,2) reflection coefficient**.** This is a relatively small difference and the model is acceptable to use for further simulations considering that the shape of the reflection coefficient curves are similar. To investigate a greater number of defects the number of elements was doubled through the thickness to provide the capability of

investigating 16 defects with equal incremental depth change shown in Figure 6.10. The next stage was to investigate the reflection coefficients with respect to frequency, therefore all 16 different defect sizes were simulated at 160, 170, 180, 190 and 200kHz. The results are shown in Figures 6.11, 6.12, 6.13, 6.14 and 6.15**.** To calculate the reflection coefficients for the range of frequencies the peak amplitudes of the incident and reflected waves were determined. This required obtaining the velocity for all measured wave modes using values from the dispersion curves and calculating the approximate arrival times. For example, the mode converted responses transmit at one wave mode's velocity and reflect at the other wave mode's velocity. The time arrival of a pulse determines the first gated region for measurement purposes and the second gate is determined by the number of cycles which captures the end of the pulse. Using these gated regions the algorithm can highlight the maximum amplitude of each response for each frequency and automatically generate the reflection coefficients for all combinations of incident and reflected wave modes.

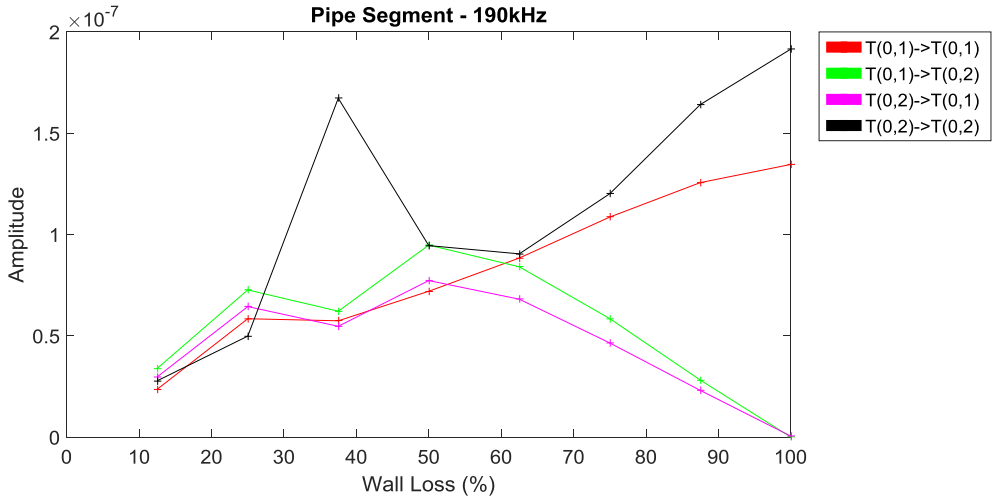

Figure 6.9. Modified pipe segment FEA model showing amplitude against wall loss at 190kHz. Element lengths approximately 1.79mm.

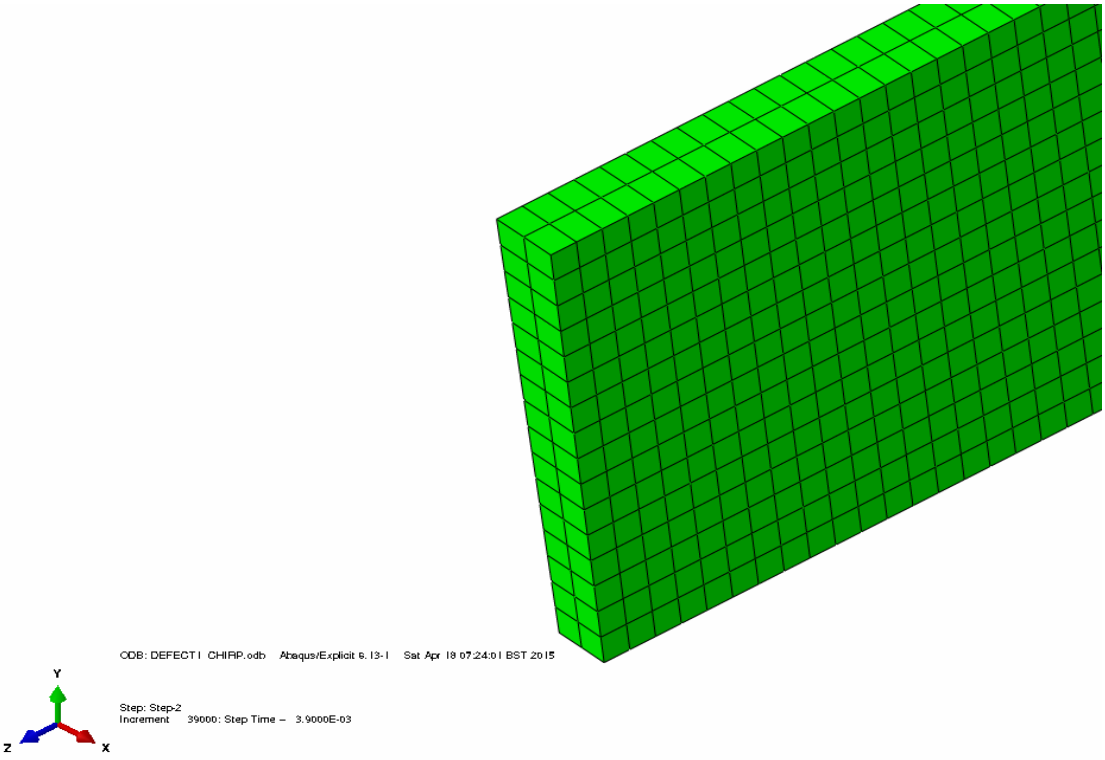

Figure 6.10. Modified pipe segment FEA model. Element lengths approximately 0.89mm.

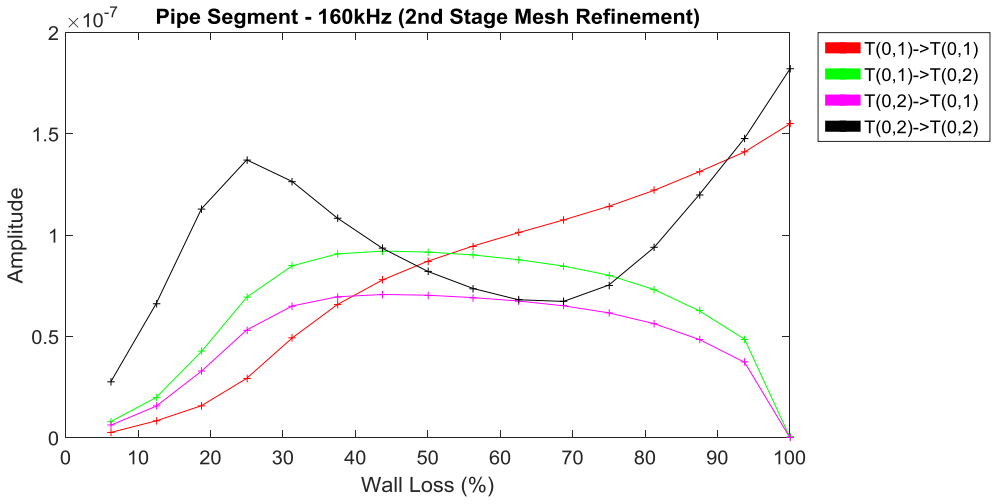

Figure 6.11. Modified pipe segment FEA model showing amplitude against wall loss at 160kHz. Element lengths approximately 0.89mm.

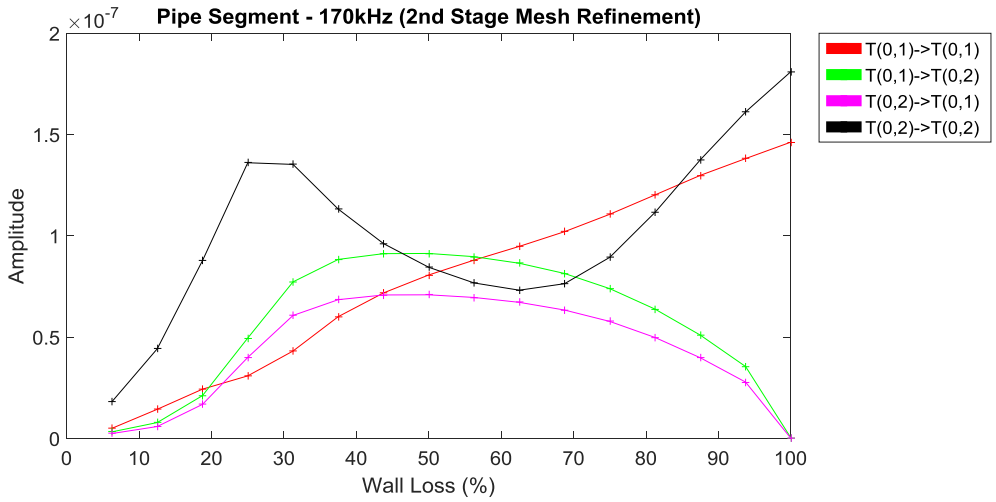

Figure 6.12. Modified pipe segment FEA model showing amplitude against wall loss at 170kHz. Element lengths approximately 0.89mm.

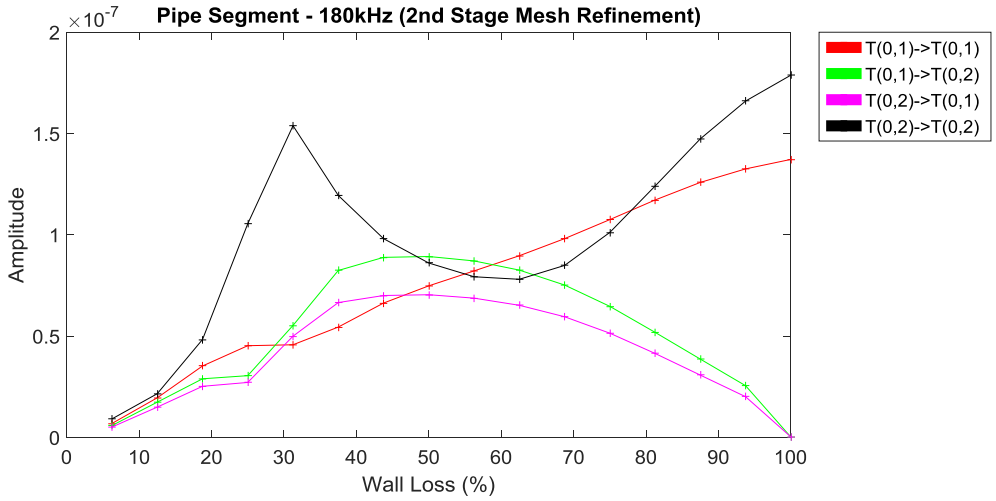

Figure 6.13. Modified pipe segment FEA model showing amplitude against wall loss at 180kHz. Element lengths approximately 0.89mm.

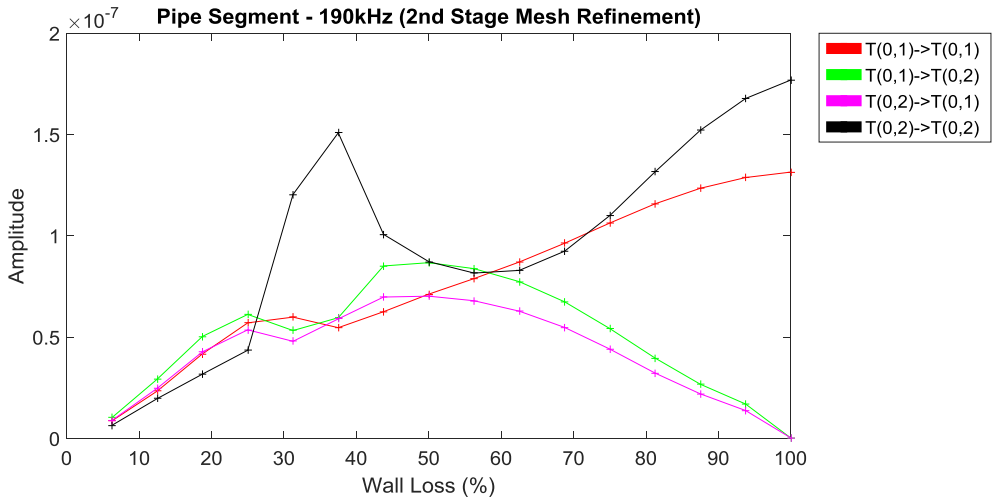

Figure 6.14. Modified pipe segment FEA model showing amplitude against wall loss at 190kHz. Element lengths approximately 0.89mm.

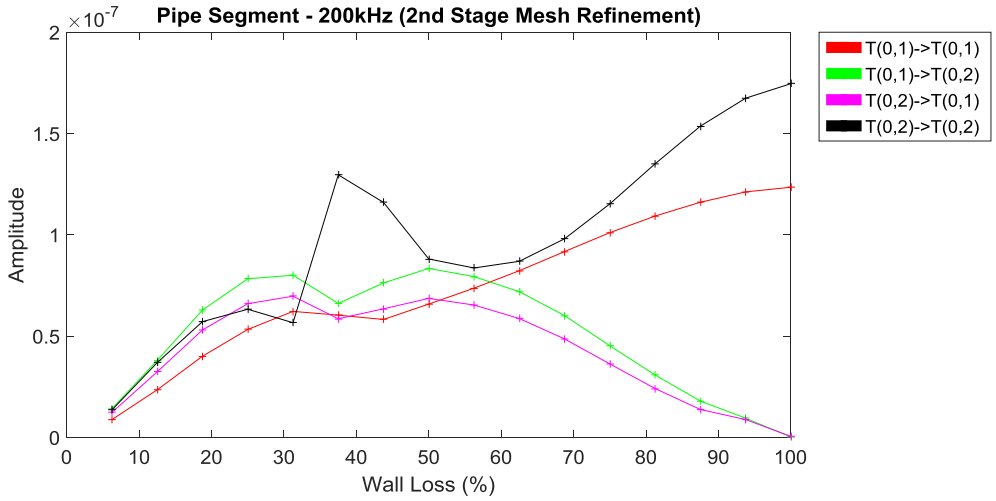

Figure 6.15. Modified pipe segment FEA model showing amplitude against wall loss at 200kHz. Element lengths approximately 0.89mm.

The results show that as the frequency increases the T(0,2) to T(0,2) reflection coefficient provides an amplitude peak at defects with a greater wall loss. This frequency dependent maximum could provide an indication to growth in defect sizes. The other responses provide no clear peak in reflection coefficients based on wall loss and frequency change.

In order to investigate the variation of reflection coefficient with frequency, a number of models are required for each defect size and frequency, which is time consuming. A frequency sweep would also need to be conducted in practical conditions, which could lead to vast amounts of stored data and could be time consuming depending on the frequency steps. These results are based around narrowband signals at particular centre frequencies. Modelling results for narrowband testing is used to compare to filtered broadband signals in the following and a technique based on broadband signals focusing on T(0,2) to T(0,2) responses for defect sizing is shown.

6.5 Defect Sizing Using Broadband Signals - Modified Pipe Segment

Broadband signals can be designed to improve the efficiency of guided wave testing. Currently, commercial systems tend to use narrowband input signals for pipe inspection although some recent research by Thornicroft [2015] has shown the potential of using broadband signals for guided wave inspection. This section shows the benefits of using broadband signals for improving FEA by reducing the number of models needed and the amount data needed for a particular inspection. To analyse a wide range of frequencies using narrowband signals would be time consuming using FEA, however using broadband signals would make FEA a feasible option when analysing a wide frequency range. Broadband signals can be designed to include a range of frequencies needed for an inspection and after reception the signals can be filtered into narrowband signals before they are interpreted. The broadband signal used in this section ranges from 145kHz to 215kHz with a duration of 300uS and is windowed using a Tukey window with a ratio of 0.2 shown in Figure 6.16**.**

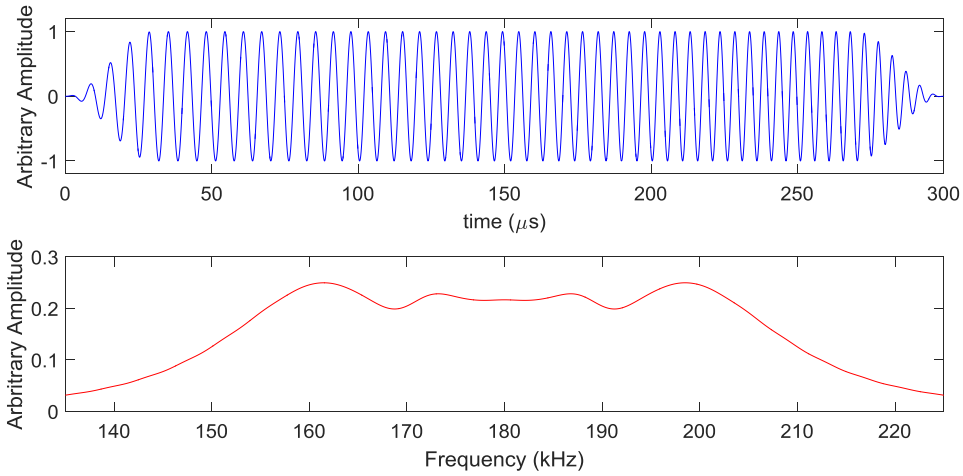

Figure 6.16. Tukey windowed chirp signal (top) and the amplitude against frequency spectrum (bottom) for 145-215kHz.

Figures 6.17, 6.18, 6.19, 6.20 and 6.21 show the normalised results for narrowband and broadband signals for the T(0,2) to T(0,2) reflection coefficient at 160, 170, 180, 190 and 200kHz respectively. The graphs were normalised by applying a scaling factor to the maximum reflection coefficient to provide a normalised amplitude value of 1. The scaling factor was then applied to the reflection coefficients for all defect sizes on both the narrowband and broadband signal responses. The results are almost identical from 160 to 190kHz with a maximum difference of 3%. The results for 200kHz have a greater difference potentially due to the bandwidth at this frequency reaching the upper limit of the broadband signal. Although there is a greater difference in amplitude at 200kHz the relative peaks in the graph occur in the same place, which is used for the analysis rather than the amplitude values.

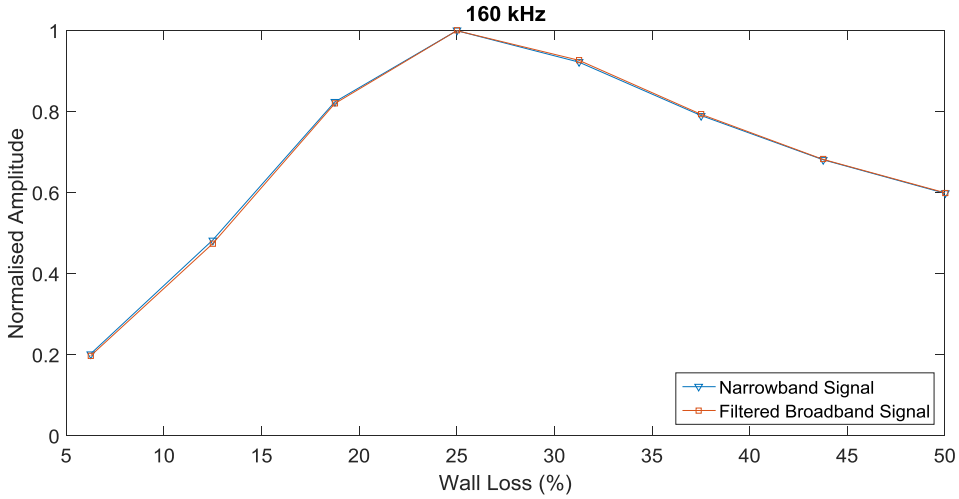

Figure 6.17. Normalised amplitude against wall loss for narrowband Hann windowed signal versus a Hann windowed signal filtered from a broadband chirp signal at 160kHz.

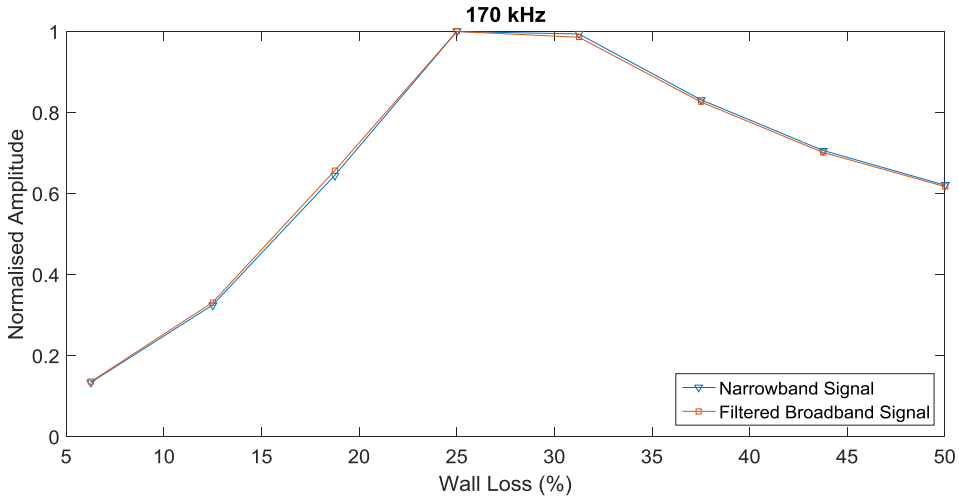

Figure 6.18. Normalised amplitude against wall loss for narrowband Hann windowed signal versus a Hann windowed signal filtered from a broadband chirp signal at 170kHz.

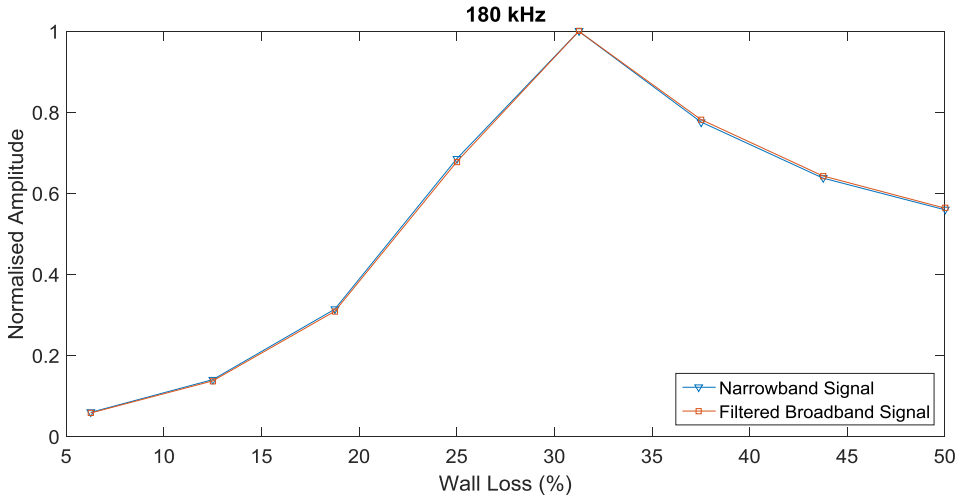

Figure 6.19. Normalised amplitude against wall loss for narrowband Hann windowed signal versus a Hann windowed signal filtered from a broadband chirp signal at 180kHz.

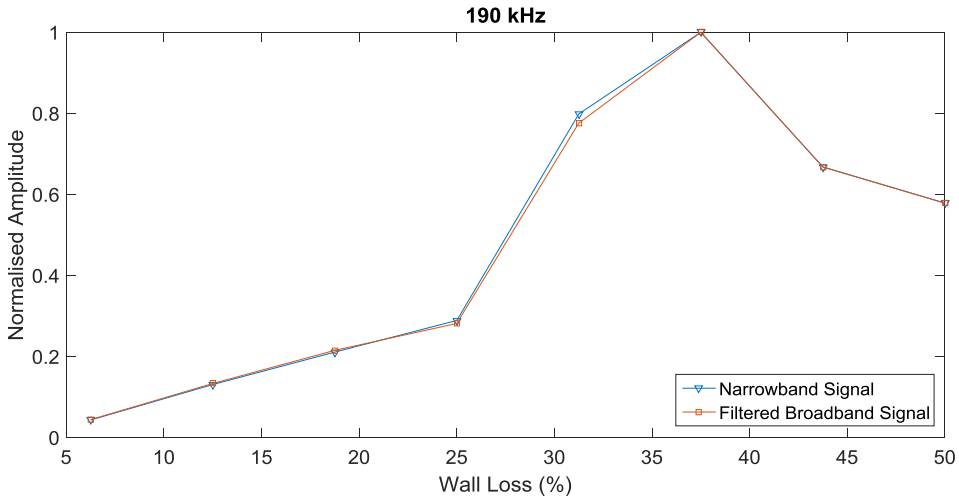

Figure 6.20. Normalised amplitude against wall loss for narrowband Hann windowed signal versus a Hann windowed signal filtered from a broadband chirp signal at 190kHz.

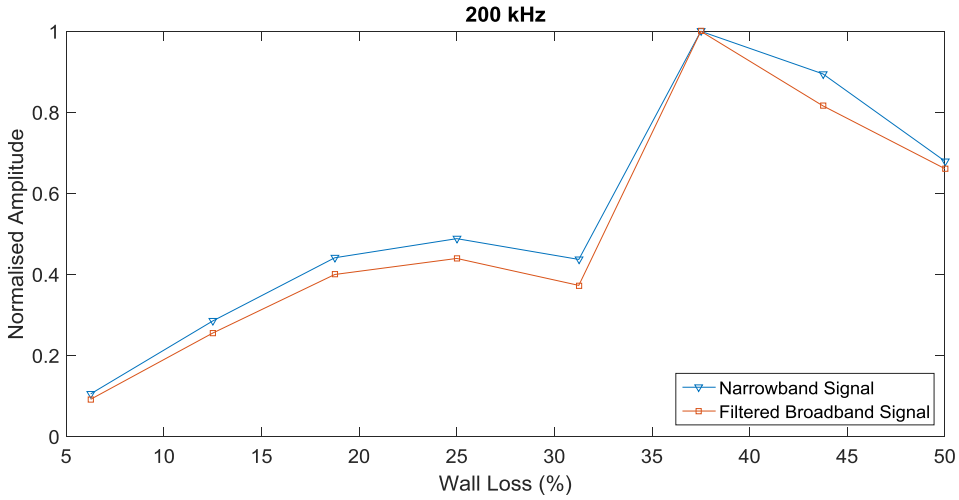

Figure 6.21. Normalised amplitude against wall loss for narrowband Hann windowed signal versus a Hann windowed signal filtered from a broadband chirp signal at 200kHz.

Considering that the filtered broadband signals match closely those of the narrowband signals, the next step is to analyse wall loss against reflection coefficient for a range of frequencies between 160 and 200kHz. A broadband signal for each defect size can be filtered into any number of frequency steps, but interpretation of the data is difficult to determine at a fine frequency step (such as 1kHz) due to the large number of reflection coefficient curves presented in one graph. In order to analyse the effects of defect size with respect to frequency, a 5kHz incremental step is used to determine the peak amplitude for the T(0,2) to T(0,2) reflection coefficient. Figure 6.22 shows the wall loss against reflection coefficient for 160 to 200kHz.

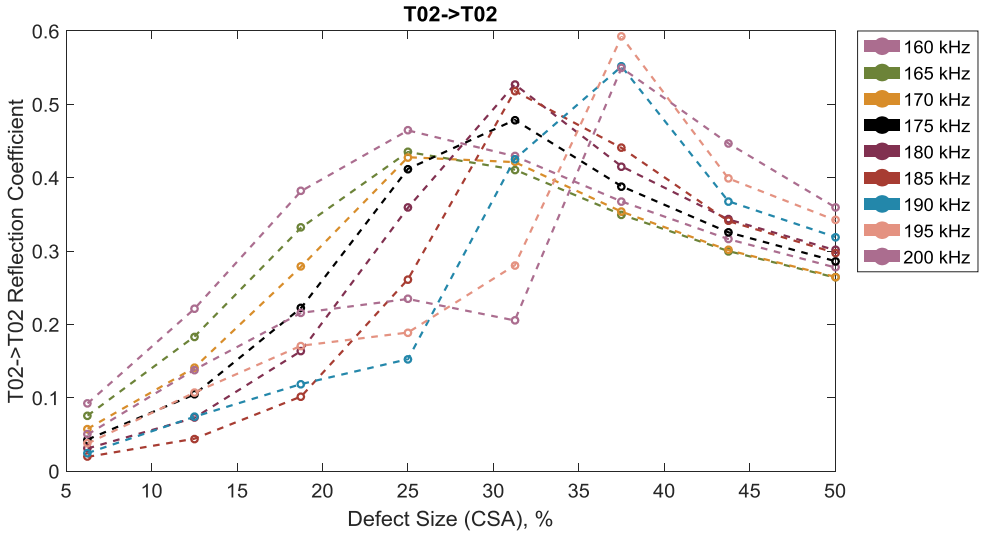

Figure 6.22. Reflection coefficient of T(0,2) against defect size (0-50% depth and axial length of 10mm) with a step change of 0.89mm for a frequency range 160-200kHz.

Each measured defect is highlighted with a marker and ranges from 0 to 50% wall loss with a 6.25% incremental change in defect size. The results show three main peak reflection coefficient amplitudes at 25, 31.25 and 37.5% wall losses. All frequencies within 160 and 200kHz provide a peak amplitude response at one of the three defect sizes. The results between 160 to 170kHz show a peak reflection coefficient amplitude at 25% wall loss. The results between 175 to 185kHz show a peak reflection coefficient response at 31.25% wall loss. Finally, the results between 190 to 200kHz show a peak reflection coefficient response at 37.5% wall loss. The trend from these results shows that as the frequency is increased a maximum reflection coefficient occurs at a greater wall loss. Once all frequencies reach their maximum reflection coefficient the amplitude in the reflected response begins to decrease, which can provide crucial information for defect sizing.

In a monitoring scenario signal characteristics can be tracked over time through repeat testing. Broadband signals could be captured repeatedly and used to monitor for developing flaws. The amplitude of signal features for a range of frequencies could be tracked and compared to FEA predictions (such as Figure 6.22). Trends could be identified and used to detect flaws and estimate their size. For a pipe of this geometry, a

defect that is between 0 to 25% wall loss would be indicated by a T(0,2) to T(0,2) reflection amplitude increase across all frequencies (and provides no indication of defect size). The first indication of defect size occurs when the reflection coefficient decreases for frequencies in the range of 160 to 170kHz (and continues to rise for the other given frequencies), which would correspond to approximately a 25% wall loss. Then, as the flaw size grows to around 31.25%, a reflection coefficient decrease would be observed between 175kHz and 185kHz. The final measurable defect size occurs at a 37.5% wall loss, when the reflection coefficient decreases for frequencies between 190 to 200kHz.

Currently, there are a range of frequencies that provide maximum reflection coefficient amplitudes at particular defect sizes. Considering that the maximum reflection coefficient is frequency dependent with defect size suggests that each frequency should represent a particular wall loss (rather than a group of frequencies representing a particular wall loss). In order to find a relationship between defect size and frequency with respect to maximum coefficient more defect sizes needed to be investigated within the defect size range shown in Figure 6.23. This approach can improve the accuracy in identifying a frequency response with a particular defect size rather than a group of frequencies relating to a defect size.

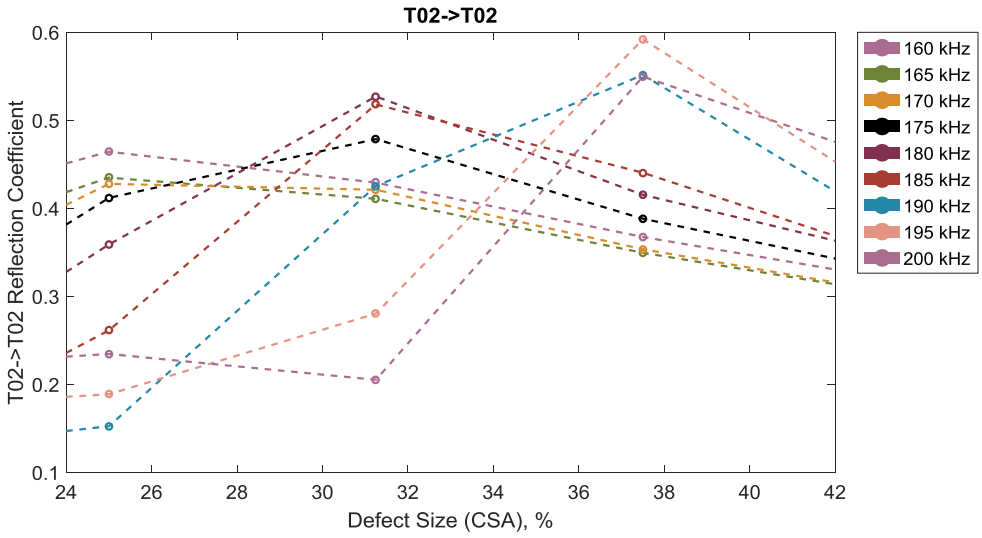

Figure 6.23. Reflection coefficient of T(0,2) against defect size (25-40.625% depth and axial length of 10mm) with a step change of 0.89mm for a frequency range 160-200kHz.

To investigate this frequency range further an FEA model with a finer mesh was created to increase the number of measurable defects, specifically in the range of 25 to 40.625% where the peak amplitudes occur. Currently the number of measurable defects from the FEA model is 16. To investigate a higher number of defects the number of elements through the thickness was increased to 32, which provides a wall loss increment of 3.125% and is shown in Figure 6.24.

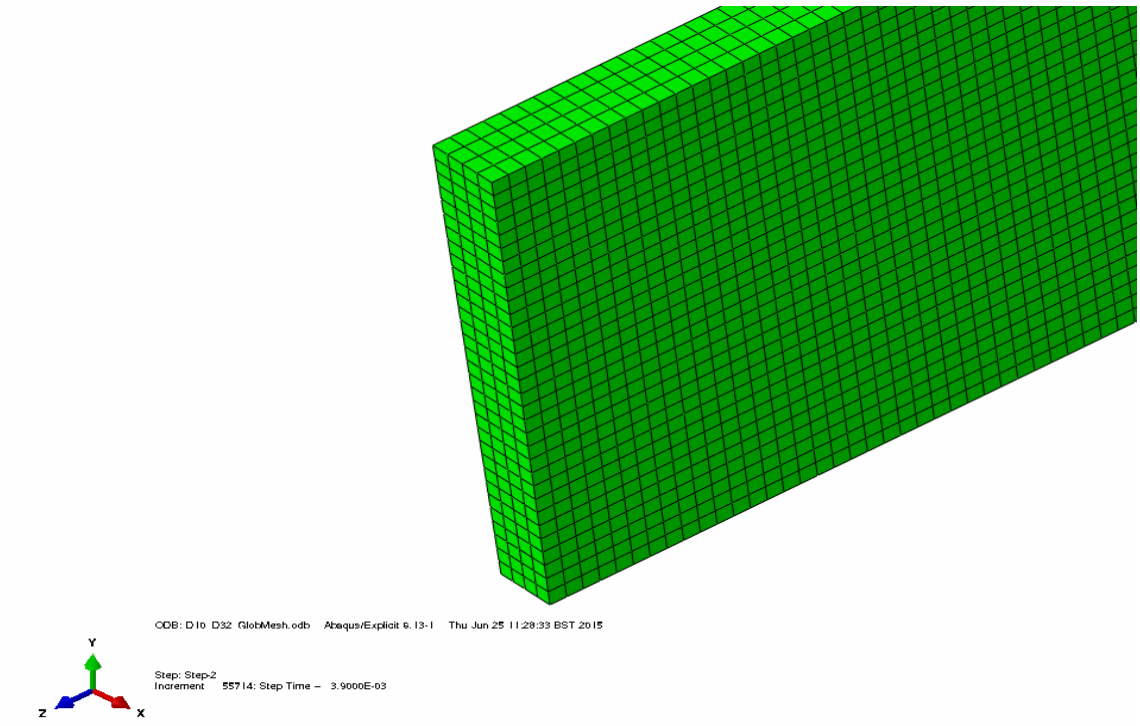

Figure 6.24. Modified pipe segment FEA model. Element lengths approximately 0.45mm.

To check that the results for the model with the finer mesh (Figure 6.25) are producing similar data a comparison is made to the previous results in Figure 6.23. The defects with a wall loss of 25%, 31.25% and 37.5% are directly comparable and are virtually identical for the range of frequencies.

The number of measurable defects has increased to 6 within the defect size range analysed (25 to 40.625% wall loss). The incremental step of the wall loss was too small in the previous model because peak amplitudes for particular defects occurred in a range of frequencies. This suggested peak amplitudes at particular frequencies overlapped as the defect size was not present for a particular frequency. The introduction of the new defect sizes show that peak amplitudes for particular frequencies occur at different defect sizes. In the previous model the results showed that the maximum reflection coefficient for a frequency range of 160 to 170kHz occurred at a 25% wall loss, 175 to 185kHz occurred at a 31.25% wall loss and 190 to 200kHz occurred at a 37.5% wall loss. This shows that an approximate range of 10kHz is associated with each defect size. The new model provides incremental defect steps of 3.125% so that the number of measurable defects is doubled.

The introduction of the new measurable defects has provided more insight into the relationship between maximum reflection coefficient and wall loss for specific frequencies. The results show that for a wall loss of 25% the maximum reflection coefficient occurs in a frequency range 160 to 165kHz. The introduction of the 28.125% wall loss shows that the maximum reflection coefficient occurs in a frequency range 170 to 175kHz. Comparing this to the previous results shows that maximum reflection coefficient has increased to a wall loss of 28.125% from 25% for 170kHz and has decreased from 31.25% to 28.125% for 175kHz. The results show that for a wall loss of 31.25% the maximum reflection coefficient occurs at frequency of 180kHz. For a 34.375% wall loss the maximum reflection coefficient occurs in the frequency range between 185 to 190kHz. The defect size with a wall loss of 37.5% has maximum reflection at a frequency of 195kHz. The final wall loss measurement is at 40.625%, which has a maximum reflection coefficient at a frequency of 200kHz. Overall, the results show that increasing the number of defects improves the accuracy of defect sizing with respect to frequency and maximum reflection coefficients. Although the comparison is between two FEA models, one with more incremental defect steps than the other, they both show that the maximum reflection coefficient is positioned on larger defect sizes when frequency is increased, which further highlights that responses to particular wall losses are frequency dependent.

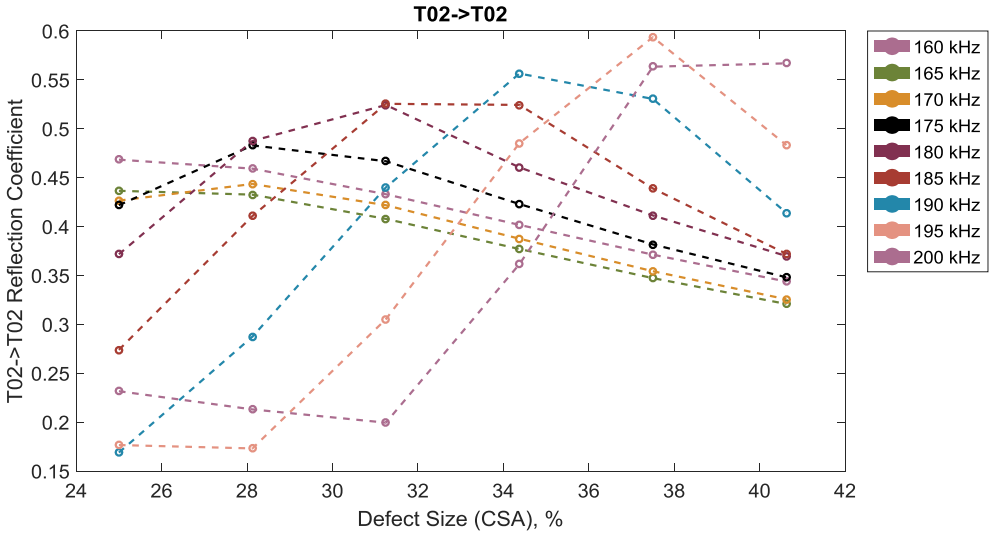

Figure 6.25. Reflection coefficient of T(0,2) against defect size (25-40.625% depth and axial length of 10mm) with a step change of 0.45mm for a frequency range 160-200kHz.

Looking at the results in Figure 6.25 some maximum reflection coefficient positions are possibly in between two measured defect sizes. For example, between the defect sizes of 31.25 and 34.375% wall loss the maximum reflection coefficient response for 185kHz has relatively negligible change and no clear peak. Whereas, the reflection coefficient for 195kHz is clearly shown at a defect size of 37.5% wall loss. This indicated that there is a possibility some defect sizes are not present for particular frequencies that have relatively small gradients towards the maximum reflection coefficient highlighted in the graph. On the other hand, frequencies that clearly show a peak for the maximum reflection coefficient at particular defect are either matched or close in frequency. Therefore, a spline function is a suitable plotting function to determine the positioning of the maximum reflection coefficient for a particular defect size. Thus, the next stage was to interpolate the results using a spline function to improve the accuracy for the maximum reflection coefficient, as shown in Figure 6.26.

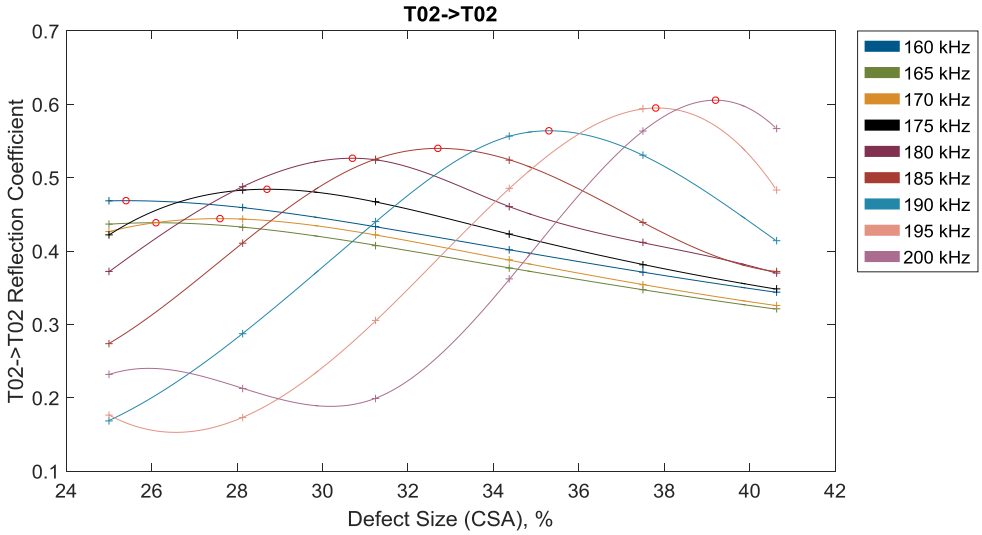

Figure 6.26. Reflection coefficient of T(0,2) against defect size (25-40.625% depth and axial length of 10mm) with a step change of 0.45mm for a frequency range 160-200kHz. Interpolated signals using a spline function. Markers indicate maximum reflection coefficients.

The results show that the maximum reflection coefficient shifts with an increase in wall loss for each frequency represented by the marker positioned on each curve. This is a considerable improvement as previous results showed overlapping frequencies for particular defect sizes. The new positioning of the maximum reflection coefficients with respect to defect size shows that interpolation is needed from FEA results, considering that the number of defects that can be simulated is limited by the computational resources. As predicted, the result for 195kHz in Figure 6.25 has a clear peak amplitude at a wall loss of 37.5%, which suggests a close match. The new results in Figure 6.26 show that there is a slight increase in defect size from the original prediction. Whereas the results for 185kHz now shows a peak amplitude between two measured defects, which could not be determined from the previous graph in Figure 6.24.

Considering that the only variable changing during the modelling is defect size an investigation was carried out regarding the remaining wall thickness of the defect. Effectively the remaining wall of the pipe with axisymmetric defects can be portrayed as a thinner pipe. The next step was to investigate the dispersion curves of these particular defects or thinner pipe segments shown in Figure 6.27 and investigate the

relationship of cut-off frequency and defect size. The maxima in the reflection of T(0,2) is likely to occur at a frequency where T(0,2) cannot propagate in the defect region reflecting most of the energy.

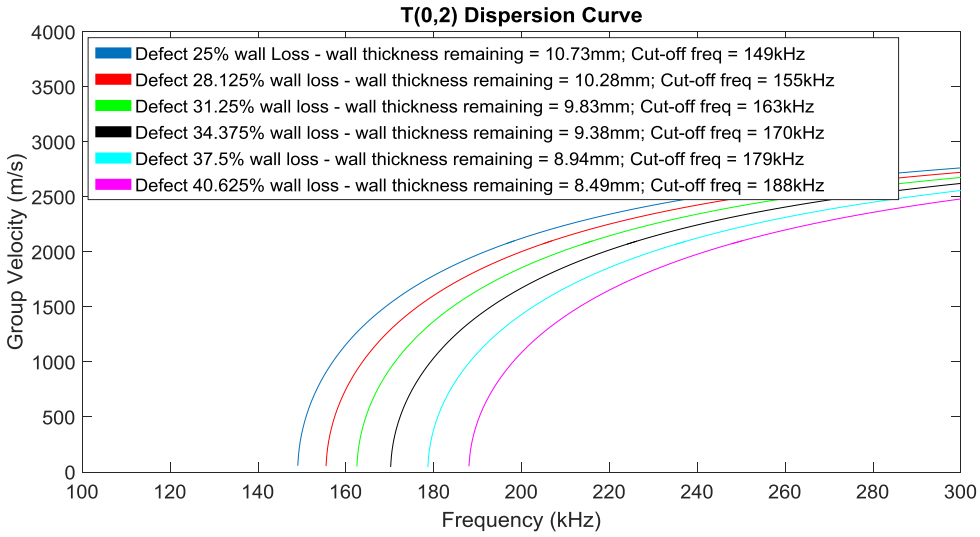

Figure 6.27. Dipsersion curve of group velocity against frequency of T(0,2) for a range of pipe thicknesses.

The next stage was to compare the cut-off frequency for a particular defect size against the defect size where the maximum reflection occurs at the same frequency, which is shown in Figure 6.28. The results show that there is a relatively linear relationship for the maximum reflection coefficient and the cut-off frequency when comparing defect size against frequency. Cut-off frequencies for different wall thicknesses are not used traditionally used to estimate defect size. However, the comparison is used in this analyse as a proposed technique for sizing defects.

Although there is a linear relationship between both results there is a difference in results for defect size and frequency. A defect size of 25% wall loss is detectable at 160kHz whereas the cut-off frequency estimates a defect size of approximately 30% wall loss, which is a difference of approximately 5%. The maximum difference occurs at the maximum measurable frequency of 180kHz, whereby the FEA results predicts the defect size has a wall loss of 31.25% and the related defect size for this particular cut-off frequency is approximately 38%, which a difference of approximately 7%. The

difference in defect size is relatively constant (on average 6%) when comparing maximum reflection coefficient and the cut-off frequency for a particular defect size.

To investigate this further there are factors to consider when comparing the reflection coefficient curves against frequency, such as the back wall reflection of the defect, the dispersive nature of T(0,2) at different frequencies, the velocity change within the defective region and the mode conversion that occurs within the defective region. The first factor that has an influence on the reflection coefficient is the back wall reflection from the 10mm length of the defect. It is currently known that the reflection coefficient for T(0,1) varies with the ratio of defect length to wavelength. The maximum reflection coefficient occurs approximately when the ratio of defect length to wavelength is 0.25, 0.75, 1.25, and so on, and the minimum reflection coefficient occurs at a ratio of defect length to wavelength occurs at 0, 0.5, 1, and so on (Demma *et al.* [2004]). This trend occurs for different defect depths whereby the reflection coefficient ratio increases linearly as depth increases. This cannot be applied directly to T(0,2) as there is a non-linear relationship between reflection coefficient and defect depth.

Another factor that complicates the reflection coefficient values against defect length is the dispersive nature of T(0,2). The velocity of T(0,2) changes with frequency and a decrease in frequency towards the cut-off increases dispersion, which has a noticeable impact when measuring peak to peak amplitudes. There is also the velocity change within the defect, which also varies depending on the remaining wall thickness and frequency. These factors that affect the reflection coefficient amplitudes must be isolated to investigate the method of determining the defect size. The next section investigates the T(0,2) to T(0,2) reflection coefficient for a step down defect (no back wall), which eliminates the response from the back wall reflection. This provides a reflection based solely on the change in wall loss and can be directly compared to the cut-off frequency for a particular defect size without any other influence affecting the T(0,2) to T(0,2) reflection coefficient.

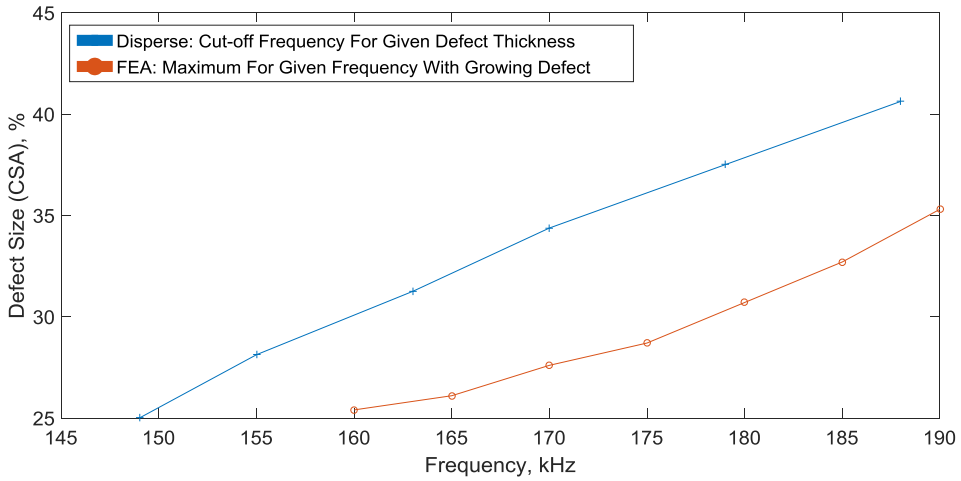

Figure 6.28. Maximum amplitude for a given frequency with a growing defect depth with an axial length of 10mm against the cut-off frequency for a given defect thickness.

Although there is a difference between maximum reflection coefficient and cut-off frequency when estimating defect size, the size can still be estimated by analysing the responses from different frequencies. An image showing maximum reflection coefficient for defect size against frequency with 1kHz intervals provides a linear trend, as shown in Figure 6.29.

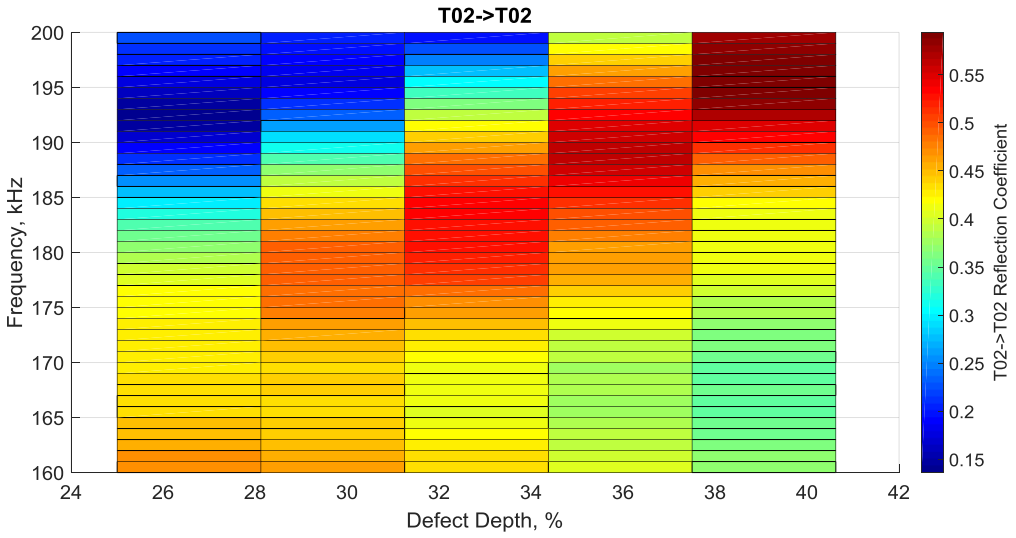

Figure 6.29. Reflection coefficient of T(0,2) for frequency against defect depth (1kHz intervals).

The results show that there is a relatively linear relationship for maximum reflection coefficient when analysing defect size against frequency. As the defect size increases the maximum coefficient occurs at a higher frequency and the amplitude also increases. The results also show the opposite effect for frequencies that have relatively low reflection coefficients particularly smaller defects at high frequencies. This effect is different to reflection coefficient imaging for T(0,1), whereby reflection coefficient is independent of frequency and only depends on size. The frequency dependency that occurs in T(0,2) provides clear intervals of defect size with respect to reflection coefficient and size can be determined without the need of a reference signal by using the relative amplitude differences for different frequencies. A curve showing reflection coefficient against frequency for the different defect sizes is shown in Figure 6.30.

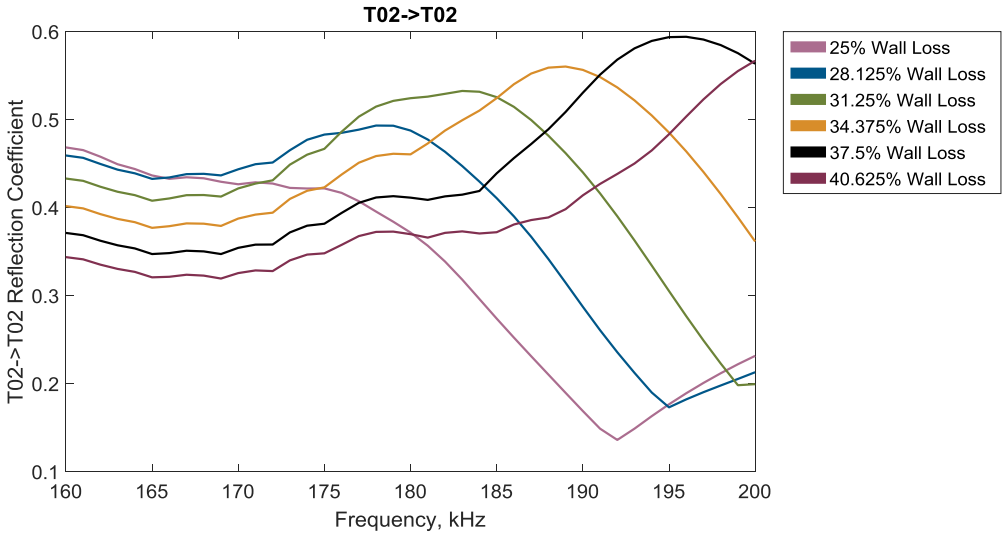

Figure 6.30. Reflection coefficient of T(0,2) against frequency for a range of defect depths (incremental change of approxiamtely 0.45mm).

The results show that defect sizes can be predicted by analysing the reflection coefficient responses obtained from different frequencies. A defect of 25% wall loss shows that an excitation frequency of approximately 160kHz provides the highest reflection coefficient amplitude. A defect of 28.125% wall loss shows that an excitation frequency of approximately 170kHz provides the highest reflection coefficient amplitude. A defect of 31.25% wall loss shows that an excitation frequency of approximately 182kHz provides the highest reflection coefficient amplitude. A defect

size of 34.375% wall loss shows that an excitation frequency of 188kHz provide the highest reflection coefficient amplitude. A defect size of 37.5% wall loss shows that an excitation frequency of 195kHz provides the highest reflection coefficient amplitude. The final defect size present is a 40.625% wall loss which shows that an excitation frequency of approximately 200kHz provides the highest reflection coefficient. For some defect sizes the difference between reflection coefficients for neighbouring frequencies is relatively small, but by analysing all frequencies as a collective group provides a range of reflection coefficient results that assist with identifying defect size.

6.6 Defect Sizing Using Broadband Signals - Modified Pipe Segment for Step Down

A step down defect is a step change in the pipe wall without a back wall or a step up and is investigated in this chapter to provide a relationship between defect depth and frequency without the influence of axial length. This section investigates the effects of defect depth with the cut-off frequency of the remaining wall thickness, which can be used to monitor a growing defect and potentially size it. Many industries use monitoring techniques to inspect particular components that have high risk to potential fatiguing. The purpose of this is not only to prevent a fatigue failure, but also to monitor areas when a fatigue crack occurs and potentially size it. This can allow companies to remain in operation if a condition monitoring system is capable of monitoring and sizing a flaw and the defect is below the maximum allowable size. A particular example of circumferential cracking is in boiler spines in the nuclear industry, which currently has no monitoring system for sizing fatigue cracking. These spines are exposed to axial stress and high temperatures up to 500^{o}C causing thermal fatigue cracking in external regions of the pipe exposed to heat. There can be a difference of 80^{o}C heat reduction on the inner wall of the pipe compared to external wall due to thick pipe walls. These types of cracks tend to propagate around the pipe before increasing in depth. Investigating a stepdown effect is a similar scenario to a fatigue crack because varying axial length of flaws is not a factor.

To investigate the effects of defect size against reflection coefficient a range of frequencies were modelled and measurements were made, which are shown in Figure 6.31. The graph shows defects ranging from 25 to 40.625% in depth and ranges from 160 to 200kHz in frequency with a 5kHz increments. The graph highlights this area rather than the entire signal as this area provides the information needed for monitoring and sizing. This is due to the reflection coefficient gradually increasing below 25% depth for all frequencies, which provides no vital information for monitoring as the reflection coefficients are similar giving no clear method of defect sizing. Consider a defect growth in a pipe which is detected by a signal response, there is no indication of the size of the defect from the isolated reflected signal alone. To investigate the characteristics of reflection coefficient with respect to defect size and frequency, a range of FEA models were created to explore the step down effect of increasing wall loss and the same analysis was conducted shown in section 6.5. The previous results showed that more than one frequency provided peak reflection coefficients for one particular defect, therefore more defect sizes were created to obtain more accurate measurements. To analyse the defect sizes in between the measured defect sizes a spline curve was fitted to the results to estimate the reflection coefficient for all defects sizes in the range, which is shown in Figure 6.32.

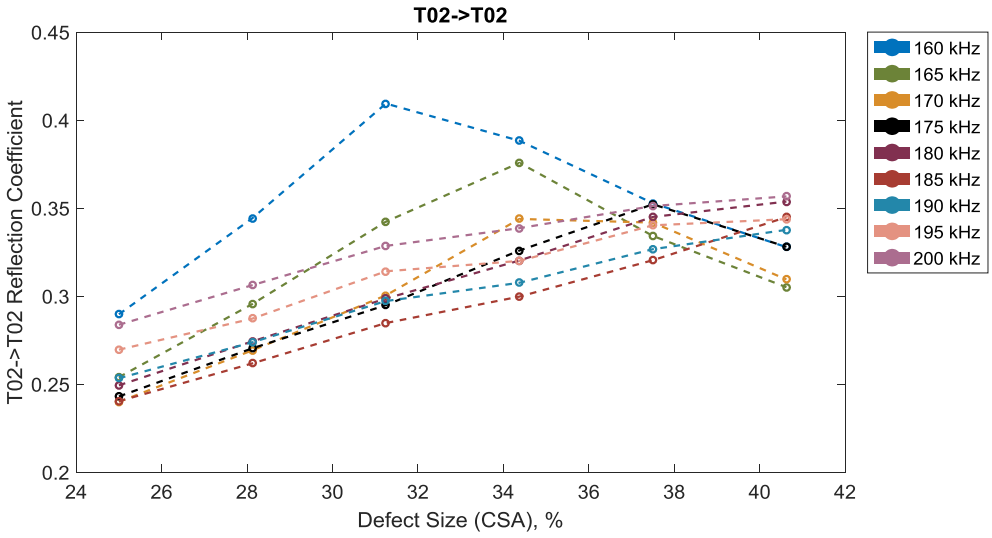

Figure 6.31. Reflection coefficient of T(0,2) against defect size (25-40.625% depth) with a step change of 0.45mm for a frequency range 160-200kHz.

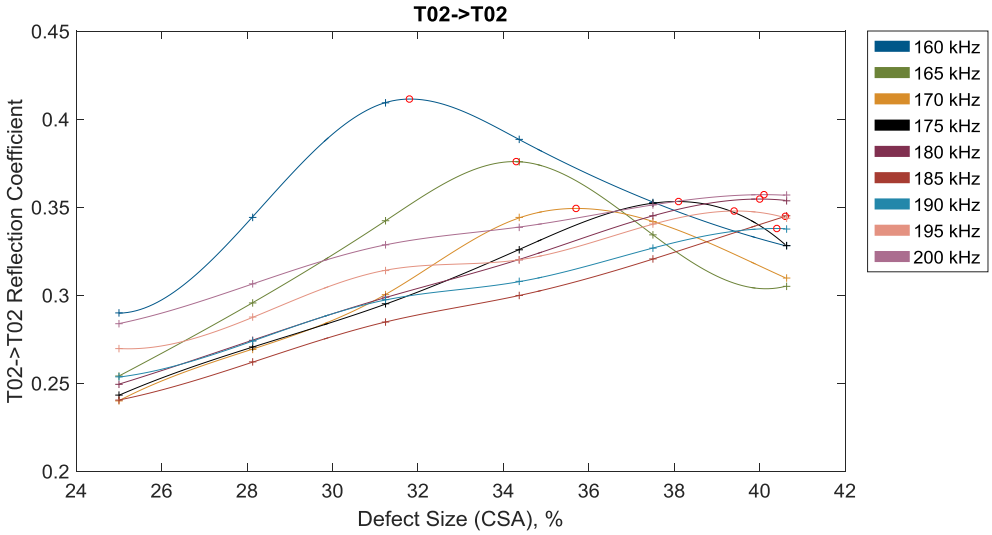

Figure 6.32. Reflection coefficient of T(0,2) against defect size (25-40.625% depth) with a step change of 0.45mm for a frequency range 160-200kHz. Interpolated signals using a spline function. Markers indicate maximum reflection coefficients.

Using the results from Figure 6.32 the maximum reflection coefficients for each defect size and frequency were plotted against the cut-off frequency for each defect size to show their relationship, which is shown in Figure 6.33. The graph shows a strong correlation between the two results indicating a defect size can be estimated using the cut-off frequency for a particular defect to an accuracy of approximately 2%. Consider monitoring a defect at 160kHz for which the reflection coefficient reaches the maximum amplitude. This would show that the wall loss had reached approximately 32%. The cut-off frequency suggests that the size of the defect at 160kHz would be approximately 30%. As the defect growth is continually monitored from the first defect size the next frequency step of 165kHz is monitored closely to identify a downturn in amplitude or peak amplitude. As the reflection coefficient starts to decrease at 165kHz this provides indication that the defect has increased to approximately 34% wall loss. Comparing this value to the cut-off frequency of different size defects again shows a prediction of approximately 32% wall loss. The under estimation of defect size that arises from the cut-off frequency is a relatively constant difference for all defect sizes measured. This could be due to a numerical discrepancy between the values obtained from FEA and Disperse, but considering the difference to be approximately 0.4mm wall loss this technique can be used to estimate the wall loss exhibited in a pipe.

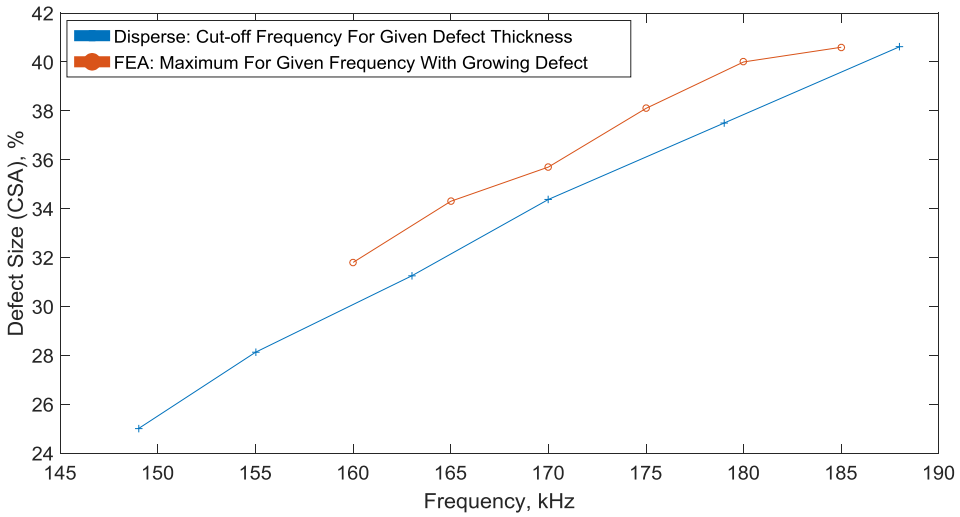

Figure 6.33. Maximum amplitude for a given frequency with a growing defect depth against the cut-off frequency for a given defect thickness.

6.7 Conclusions

This chapter shows that there is a strong correlation between maximum reflection coefficient for T(0,2) incident to T(0,2) reflected for a given frequency and the associated cut-off frequencies for a defect size of particular wall loss. This finding can be used for monitoring defect growth in a pipe, which can be used to analyse the residual life in service of the pipeline.

This chapter has shown the benefits of using T(0,2) in comparison to T(0,1) by combining a relationship between maximum reflection coefficient and frequency to defect size. The key difference is that T(0,2) has a response from defects that are frequency dependent, which has been quantified. Whereas, T(0,1) amplitude response from defects is independent of frequency and as the defect increases in size the reflection coefficient increases. This provides no peak amplitude responses and defect sizes cannot be determined from the reflected signals alone or without a reference signal. Therefore, a technique that monitors for frequency dependent characteristics

does not need a simple signal. Changes to the frequency spectrum can be detected in complex signals; therefore this could be a useful technique for monitoring complex structures where clear reflections are not apparent.

Many guided wave systems operate in pulse-echo mode, whereby the transducers transmit/receive from the same location and during transmission the systems are unable to measure any reflections. This transmission period is known as the 'dead zone' which can be significantly reduced by operating at medium frequencies, as the wavelength of a signal is significantly reduced. Operating at T(0,2) may therefore allow the operator to perform inspections at higher frequencies and inspect in the near fields that cannot be inspected at low frequency ranges. Another benefit of using medium frequencies can be used to increase the spatial resolution potentially increasing defect sensitivity and directionality, Teletest Focus+ currently uses a focusing technique to improve sensitivity and directionality, which can be enhanced by using higher order wave modes.

This chapter has also shown techniques for improving FEA models that maximise the number of defects that can be analysed, improve computational time and reduce the required number of models. The first step was to take the full pipe model and reduce this to a pipe segment that is capable of representing the full pipe. This increased the number of possible defects that can be analysed from 8 to 32 and improved computational performance significantly. The second improvement was to replace narrowband input signals with broadband signals and then filtering the broadband signals into relevant narrowband signals. This technique significantly improved the processing time as ranges of frequencies could be analysed from one particular model rather than running individual models for each frequency. Considering that individual frequencies were analysed in particular parts of the chapter from 160-200kHz this would result in 40 models from a narrowband frequency testing for one particular defect, whereas using a broadband input signal only one model is needed.

Overall, T(0,2) is capable of determining defect size for monitoring defect growth rapidly. The benefits of operating at a medium frequency are improving defect sensitivity through increased spatial resolution and reducing dead zones, which are all beneficial to the oil, gas and nuclear industries.

7 CONCLUSIONS AND FURTHER WORK

7.1 Conclusions

The purpose of this research was to develop a technique for inspecting pipes using medium range frequencies. A novel technique has been developed to size defects using the T(0,2) wave mode based on an amplitude and frequency relationship (chapter 6). The research has shown that for T(0,2) at a particular defect size and frequency a peak amplitude response occurs. For defects where axial length has no influence on the peak amplitude response, it was shown that the response is closely related to the cut-off frequency of T(0,2). Therefore, if a peak amplitude response occurs at a particular frequency, the defect depth can be estimated from T(0,2) dispersion curves consisting of a range of pipe thicknesses corresponding to the remaining wall of the defect.

An effective way of performing FEA using guided waves and processing the data has been developed (chapter 4). A modified pipe segment was created to replicate a full pipe model based on the pipe used in the experiments, which was used to analyse defects with smaller increments that could not be achieved using a full 3D model. This improvement also provided a method for analysing a larger number of defects in smaller increments (<0.5mm), which are extremely difficult to accurately machine into a pipe.

In the conventional full pipe model 8 defects could be measured through the thickness; however the pipe segment provided the capability of analysing 32 defects.

The next development was implementing medium range frequency broadband signals to the pipe segment (chapter 4). Thornicroft [2015] developed a technique and experimentally investigated low range frequencies for the fundamental wave modes by filtering narrowband signals from broadband signals. The method was adapted to medium frequencies to extract both T(0,1) and T(0,2) from the complex broadband signal response, which provided the full frequency range used to analyse each defect from one model. This is a significant advantage for FEA in comparison to the conventional method of using narrowband signals because it eliminates the need to run individual models for each frequency.

The development of the high density array (chapter 5) showed that by eliminating the transducer gap and increasing the number of transducer elements in the array provided a purer transmission of the T(0,1) wave mode at low range frequencies. The signal to noise ratio was improved and the results showed that the amplitude of the defects increase linearly with depth, which agreed to the research conducted by Carandente *et al.* [2012]. The results for the medium range frequency testing were complex and not directly comparable to some of the preliminary FE modelling. Investigating the features of the high density array and experimental setup showed that the length of the transducers have a significant effect on the transmitted wave modes. The amplitude of transmitted is wavelength dependant and is predicted to be at a minimum when the transducer length equals 1 wavelength. The recommended transducer length is up to ¼ wavelength of the transmitted wave mode because significantly sub-optimal interference can occur above this length.

Generally, operating at medium range frequencies reduces dead zones (transmission period) providing the capability of near field inspection and increasing spatial resolution potentially increasing defect detectability. Reducing the dead zone and increasing the spatial resolution can give a technique that can be used to inspect shorter sections of

pipe with higher resolution than current low range frequency cannot achieve. Using this knowledge and the developed defect sizing technique using T(0,2) could be the basis for improving the capabilities of guided wave inspection.

7.2 Further work

In order to advance on the defect sizing technique presented in this project alternative defects should be analysed using T(0,2). The first feature to analyse would be defects with varying axial lengths. The work presented in chapter 6 showed that axial length can have an impact on the amplitude of T(0,2), however the relationship between axial length and T(0,2) is yet to be fully characterised. Using the relationship between the axial length of the defect, peak amplitude and frequency could provide additional information to the defect sizing technique presented in this thesis. The combination of depth and axial length should be studied, which could potentially provide a three dimensional sizing technique for axisymmetric defects. The next stage would be to investigate the non-axisymmetric defects whereby the circumferential or angular extent of the defect varies. Varying axial and circumferential extent have been investigated using fundamental wave modes. Cawley *et al.* [2002] investigated the L(0,2) family of wave mode whereas Demma [2003] and Catton [2009] investigated the T(0,1) family. Both investigated defect depths showing a linear relationship for reflection coefficient against defect depth, however the results from this thesis show a non-linear relationship for T(0,2) with clear amplitude peaks at a particular defect frequency combination. Therefore, the circumferential and axial lengths should be investigated for defect, amplitude and frequency relationships that might be able to contribute to defect sizing.

Considering that T(0,2) is avoided in guided wave inspection and the research presented in this thesis has shown potential for defect sizing, the next stage would be to investigate T(0,3). This could potentially increase the frequency range used for guided wave inspection and increase the range presented in this thesis.

Alternatively, a two ring transmission array can be investigated to suppress T(0,3) to operate at higher frequencies using T(0,2) without the influence of T(0,3), which determined the upper frequency range when considering the technique developed in chapter 4. Inverting the excitation signal of the second ring of transmitters and time delaying the signal by the group velocity of T(0,3) would provide destructive interference hence suppressing the wave mode. Therefore, transmitting only T(0,1) and T(0,2).

The high density transducer array developed in this thesis showed improvements for low range frequency testing by improving the signal to noise ratio in comparison to existing transducer array used for guided wave inspection. This was achieved by increasing the number of transducers and equally spacing them. However, results showed that the length of the transducer had a significant influence on the transmitted signal. Therefore, the influence of transducer size and shape on transduction should be investigated in order to find the optimum transducer size for propagating guided waves at medium frequencies.

8 REFERENCES

ABAQUS. 2012. ABAQUS Version 6.12 User's Manual. Simulia.

Alleyne, D, & Cawley, P. 1992. Optimization of Lamb wave inspection techniques. NDT & E International, 25(1), 11-22.

Alleyne, D, & Cawley, P. 1994. The practical excitation and measurement of Lamb waves using piezoelectric transducers. Review of Progress in Quantitative Nondestructive Evaluation, 13, 181-188.

Alleyne, D, & Cawley, P. 1996. The excitation of Lamb waves in pipes using dry-coupled piezoelectric transducers. Journal of Nondestructive Evaluation, 15(1), 11-20.

ANSYS. 2013. ANSYS Version 15 User's Manual. Ansys Inc.

Bartoli, I, Scalea, F, Fateh, M, & Viola, E. 2005. Modeling guided wave propagation with application to the long-range defect detection in railroad tracks. NDT&E International, 38, 325-334.

Bartoli, I, Marzani, A, Scalea, F, & Viola, E. 2006. Modeling wave propagation in damped waveguides of arbitrary cross-section. Journal of Sound and Vibration, 295, 685–707.

Böttger, W, Schneider, H, & Weingarten, W. 1987. Prototype EMAT system for tube inspection with guided ultrasonic waves. Nuclear Engineering and Design, 102, 369-376.

Carandente, R, Ma, J, & Cawley, P. 2010. The scattering of the fundamental torsional mode from axi-symmetric defects with varying depth profile in pipes. Journal of the Acoustical Society of America, 127 (6), 3440-3448.

Carandente, R, & Cawley, P. 2012. The effect of complex defect profiles on the reflection of the fundamental torsional mode in pipes. NDT&E International, 46, 41-47.

Catton, P, Mudge, P, & Balachandran, W. 2008. Advances in defect characterisation using long-range ultrasonic testing of pipes. Insight, 50(9), 480-484.

Catton, P. 2009. Long Range Ultrasonic Guided Waves for the Quantitative Inspection of Pipelines. EngD. Thesis, Brunel University.

Cawley, P, Lowe, M, Simonetti, F, Chevalier, C, & Roosenbrand, A. 2002. The reflection coefficient of extensional guided waves in pipes as a function of defect depth, axial extent, circumferential extent and frequency. Journal of Mechanical Engineering Science, 216(11), 1131-1143.

Cho, S, Kim, H & Kim, Y. 2010. Megahertz-Range Guided Pure Torsional Wave Transduction and Experiments Using a Magnetostrictive Transducer. IEEE Transactions on Ultrasonics, Ferroelectrics, and Frequency Control, 57(5), 1225-1229.

Chree, C. 1886. Longitudinal waves of a solid bar. Quarterly Journal of Pure and Applied Mathematics, 21, 287-298.

COMSOL Multiphysics. [2012]. Version 4.3 User's Guide. COMSOL AB.

Demma, A, Cawley, P, Lowe, M, & Roosenbrand, A. 2003. The reflection of the fundamental torsional mode from cracks and notches in pipes. Journal of the Acoustical Society of America, 114(2), 611- 625.

Demma, A, Cawley, P, Lowe, M, Roosenbrand, A, & Pavlakovic, B. 2004. The reflection of guided waves from notches in pipes: a guide for interpreting corrosion measurements. NDT&E International, 37, 167-180.

Ditri, J, & Rose, J. 1992. Excitation of guided elastic wave modes in hollow cylinders by applied surface tractions. Journal of Applied Physics, 72(7), 2589-2597.

Drozdz, M. 2008. Efficient Finite Element Modelling of Ultrasound Waves in Elastic Media. Ph.D Thesis, Imperial College.

FEMLAB. 2004. Version 3.0 User's Guide and Introduction. COMSOL AB.

Graff, K. 1975. Wave motion in elastic solids. New York: Dover.

Ghosh, J. 1923. Longitudinal Vibrations of a Hollow Cylinder. Bulletin of the Calcutta Mathematical Society, 14(1), 31-40.

Herrmann, G, & Mirsky, I. 1956. Three-dimensional and shell theory analysis of axially symmetric motions of cylinders. Journal of Applied Mechanics, 78, 563-568.

Helmholtz, H. 1954. On the Sensations of Tone. New York: Dover Publications.

Hayashi, T, & Rose, J. 2003. Guided wave simulation and visualization by a semianalytical finite element method. Materials Evaluation, 75-79.

Hosten, B, & Castaings, M. [2005] Finite elements methods for modeling the guided waves propagation in structures with weak interfaces. Journal of the Acoustical Society of America, 117 (3), 1108-1113.

Lamb, H. 1910. The Dynamical Theory of Sound. New York: E. Arnold.

Lamb, H. 1917. On waves in an elastic plate. Proceedings of the Royal Society of London, 93 (648), 114-128.

Li, J, & Rose, J. 2001. Excitation and propagation of non-axisymmetric guided waves in a hollow cylinder. Journal of the Acoustical Society of America, 109(2), 457-464.

Li, J, & Rose, J L. 2002. Angular-Profile Tuning of Guided Waves in Hollow Cylinders Using a Circumferential Phased Array. IEEE Transactions on Ultrasonics, Ferroelectrics and Frequency Control, 49(12), 1720-1729.

Lowe, M. 1995 Matrix techniques for modeling ultrasonic waves in multilayered media, IEEE Transactions on Ultrasonics, Ferroelectrics, and Frequency Control, 42, 525–542.

Lowe, M, Alleyne, D, & Cawley, P. 1998. The Mode Conversion of a Guided Wave by a Part-Circumferential Notch in a pipe. Journal of Applied Mechanics, 65, 649-656.

Love, A. Some Problems of Geodynamics. Cambridge University Press, 1911.

Kannan, E, Maxfield, B, & Balasubramaniam, B. 2007. SHM of pipes using torsional waves generated by in situ magnetostrictive tapes. Smart Materials and Structures, 16, 2505–2515.

Kim, H, Cho, S, & Kim, Y. 2011. Analysis of internal wave reflection within a magnetostrictive patch transducer for high-frequency guided torsional waves. Ultrasonics. 51, 647–652.

Krautkrämer, J, & Krautkrämer, H. 2013. Ultrasonic testing of materials. Springer Science & Business Media, 5-14.

Kwon, Y, Kim, H & Kim, Y. 2010. Method to Suppress Higher Modes of the Guided Torsional Wave for Sending the Non-dispersive Mode through a Pipe. IEEE International Ultrasonics Symposium Proceedings, 1166-1168.

Kwon, Y, Kim, H, Kim, Y. 2015. High-frequency lowest torsional wave mode ultrasonic inspection using a necked pipe waveguide unit. Ultrasonics, 62, 237-243.

Kwun, H, & Bartels, A. 1998. Magnetostrictive sensor technology and its applications. Ultrasonics, 36, 171-178.

McFadden, J. 1954. Radial Vibrations of Thick-Walled Hollow Cylinders. Journal of the Acoustical Society of America, 26, 714-715.

Meitzler, A, H. 1961. Mode coupling occurring in the propagation of elastic pulses in wires. Journal of the Acoustical Society of America, 33(4), 435-445.

Mu, J, Zhang, L, & Rose, J. 2007. Defect circumferential sizing by using long range ultrasonic guided wave focusing techniques in pipe. Nondestructive Testing and Evaluation, 22(4), 239-253.

Mudge, P, Lank, A, & Alleyne, D. 1996. Long Range Method of Detection of Corrosion under Insulation in Process Pipework. 5th European Union Hydrocarbons Symposium, Edinburgh.

Mudge, P, & Lank, A. 1997. Detection of corrosion in pipes and pipelines. ASNT International Chemical and Petroleum Industry Inspection Technology Topical Conference V, Houston, Texas.

Mudge, P, & Catton, P. 2008. Quantification of Defect Size from Long Range Guided Wave Ultrasonic Tests on Pipes. Review of Quantitative Nondestructive Evaluation, 27, 147-154.

Pavlakovic, B, Lowe, M, Alleyne, D, & Cawley, P. 1997. Disperse: a general purpose program for creating dispersion curves. Review of Progress in Quantitative Non-destructive Evaluation, 16, 185-192,

Pochhammer, L. 1876. On the propagation velocities of small oscillations in an unlimited isotropic circular cylinder. Journal fur die Reine und Angewandte Mathematik, 81, 324-336.

Ratassepp, M, & Klauson, A. 2006. Curvature effects on wave propagation in an infinite pipe. ULTRAGARSAS, 2(59), 19-25.

Rayleigh, Lord. 1885. On waves propagated along the plane surface of an elastic solid. Proceedings of the London Mathematical Society, 17, 4-11.

Polytec. 2009. PSV-400-3D Scanning Vibrometer Data Sheet. Polyec. Available from: http://users.ox.ac.uk/~abrg/spider_site/pdfs/SpecsPSV-400-3D.pdf

Rokhlin, S. 1980a. Diffraction of Lamb waves by a finite crack in an elastic layer, Journal of the Acoustical Society of America, 67, 1157-1165.

Rokhlin, S. 1980b. Analysis of Lamb wave diffraction by a finite crack using the method of generalized scattering matrices. Ultrasonics Symposium Proceedings, 922-926.

Rose, J, Sun, Z, Mudge, P, & Avioli, M. 2003. Guided Wave Flexural Mode Tuning and Focusing for Pipe Testing. Materials Evaluation, 162-167.

Rudd, K, Leonard, K, Bingham, J, & Hinders, M. 2007. Simulation of guided waves in complex piping geometries using the elastodynamic finite integration technique. Journal of the Acoustical Society of America, 121(3), 1449-1458.

Sanderson, R, & Smith, S. 2002. The Application of Finite Element Modelling to Guided Ultrasonic Waves in Rails. Insight - Non-Destructive Testing and Condition Monitoring, 44(6), 359-362.

Sanderson, R, & Smith, S. 2003. The application of finite element modelling to guided wave testing systems. Review of Progress in Quantitative Nondestructive Evaluation. AIP Conference Proceedings, 22, 256-263.

Sanderson, R. 2012. Quantitative Studies in Guided Wave Inspection of Pipelines. Ph.D. Thesis, University of Warwick.

Schneider, H. 1984. The nondestructive testing of tubes and pipes for nuclear application. Nuclear Engineering and Design, 81, 69-76.

Silk, M, & Bainton, K. 1979. The propagation in metal tubing of ultrasonic wave modes equivalent to lamb waves. Ultrasonics, 17, 11-19.

Strutt, J. 1885. On waves propagated along the plane surface of an elastic solid. Proceedings of the London Mathematical Society, 17, 4-11.

Su, Z, Ye, L, & Lu, Y. 2006. Guided Lamb waves for identification of damage in composite structures: A review. Journal of Sound and Vibration, 265, 753-780.

Sun, Z, Rose, J, Song, W-J, & Hayashi, T. 2003. Non-Axisymmetric Wave Focusing In Pipe Inspection. Review of Quantitative Nondestructive Evaluation, 22, 244-249.

Thornicroft, K. 2015. Ultrasonic Guided Wave Testing of Pipelines using a Broadband Excitation. Ph.D. Thesis, Brunel University.

Velichko, A, & Wilcox, P. 2009. Excitation and scattering of guided waves: Relationships between solutions for plates and pipes. Journal of the Acoustical Society of America, 125(6), 3623-3631.

Viktorov, I. 1967. Rayleigh and Lamb Waves - Physical Theory and Applications. New York, NY: Plenum Press.

Viktorov, I. 1967. Rayleigh and lamb waves: physical theory and application. Moscow: Acoustics Institute, Academy of Science of the USSR, (translated from Russian by Warren P. Mason).

Worlton, D. 1951. Ultrasonic testing with Lamb waves. Nondestructive Testing, 15(14), 218-222.

Worlton, D. 1961. Experimental confirmation of Lamb waves at megacycle frequencies. Journal of Applied Physics, 32, 697-971.

Yoon, B, Yang, S, Lee, H, & Kim, Y. 2010. Detection and Mode Identification of Axial Cracks in the Steam Generator Tube of the Nuclear Power Plant Using Ultrasonic Guided Wave. Journal of Nuclear Science and Technology, 47(8), 754-759.

Zemanek, J. 1972. An experimental and theoretical investigation of elastic wave propagation in a cylinder. Journal of the Acoustical Society of America, 51, 265 283.

Zhang, L. 2005. Guided Wave Focusing Potential in Hollow Cylinders. Ph.D Thesis, The Pennsylvania State University.

Zhang, L, Gavigan, B, & Rose, J. 2006. High Frequency Guided Wave Natural Focusing Pipe Inspection with Frequency and Angle Tuning. Journal of Pressure Vessel Technology, 128, 433-438.

Zhou, W J, Ichchou, M N, & Mencik, J M. 2009. Analysis of wave propagation in cylindrical pipes with local inhomogeneities. Journal of Sound and Vibration, 319, 335-354.

Zhu, W. 2002. An FEM simulation for guided elastic wave generation and reflection in hollow cylinders with corrosion defects. Journal of Pressure Vessel Technology, 124, 108-117.

9 APPENDICES

9.1 Teletest Focus+ Technical Specification

Standard Output Voltage	300V Peak to peak
Number of Transducer Channels	24 independent
Maximum Number of Signal Averages	1,000,000
Maximum Sample Range (ms)	1000
Receiving Gain Range	20 -100dB in 1db steps
Teletest® Focus + Weight (Kg)	8
Teletest® Focus + Dimensions (cm)	33 x 33 x 14
Run Time on Battery (hours)	10 typical
Communication Protocol	Ethernet
Integrated Air Pump	Standard
Frequency Range (Pulser-receiver)	20-300kHz
Frequency Range (Normal operation)	20-100kHz